Development of a modelling strategy for simulation of coastal development due to tsunamis

Dissertation

in fulfilment of the requirements for the degree “Dr. rer. nat.”
of the Faculty of Mathematics and Natural Sciences
at Kiel University

Submitted by

Silvia Chacón-Barrantes

KIEL, GERMANY

2015

Development of a modelling strategy for simulation of coastal development due to tsunamis

Dissertation

in fulfilment of the requirements for the degree “Dr. rer. nat.”
of the Faculty of Mathematics and Natural Sciences
at Kiel University

Silvia Chacón-Barrantes

January 2015

Supervisor:
Prof. Dr. Roberto Mayerle

Coastal Research Laboratory
Research and Technology Centre
Christian Albrechts University
Kiel, Germany

First referee: Prof. Dr. Roberto Mayerle

Second referee: Prof. Dr. Athanasios Vafeidis

Date of oral examination: 09.06.2015

Approved for publication: 09.06.2015

Abstract

The world's coasts get more populated every year and most of them are under tsunami risk. Recently the 2004 Indonesia tsunami and the 2011 Japan tsunami have shown the destructive potential of tsunamis interacting with human settlements. Inundation of dry land is the most known tsunami damage but tsunamis also change the coastal morphology, at least temporally. In most of the cases, those changes disappear within several months or years. This work seeks to get a better understanding of the tsunami phenomenon and its consequences beyond wave height, by means of the modelling of tsunami morphodynamics. First, a modelling study was performed addressing the possible consequences of tsunamis at the North Sea and the German Bight, including a Storegga-like scenario. Tsunami current velocities were modelled and compared with those of storm surges at the North Sea and German Bight. Tsunami water levels were found to be smaller than those of storm surges, yet their flow velocities were comparable and tsunamis acted during a shorter period of time. Second, a parameterization of tsunamis was tried by means of N-waves. The morphological changes caused by the waves depended on their orientation. Tsunami flow velocities and morphological changes were more sensitive to the waveform than runup, making difficult to establish a generalization. And third, three-dimensional morphological changes were simulated in Tamil Nadu at the east coast of India by a tsunami similar to the 2004 Indian Ocean tsunami. The study region was an open coastline and the model results showed a flattening of the bed and a widening of the beach, both effects documented during the 2004 Indian Ocean tsunami. The results obtained in this thesis show that there is still much work to do on modelling tsunami morphodynamics. There are no specific equations for tsunami sediment transport and much more data is required for tsunami morphodynamics modelling than for hydrodynamics modelling. However, the results also show that modelling tsunami morphodynamics can be performed even with those limitations but with reduced certainty. Then, the modelling of tsunami morphodynamics becomes a useful tool to understand tsunami behaviour and forecast damages.

Keywords: *tsunami, morphological changes, tsunami deposits, N-waves, North Sea, 2004 Indian Ocean tsunami*

Zusammenfassung

Die Küsten der Welt werden von Jahr zu Jahr zunehmend stärker bevölkert und die meisten dieser Küsten sind dem Risiko von Tsunamis ausgesetzt. In der jüngeren Vergangenheit haben der indonesische Tsunami von 2004 und der japanische Tsunami von 2011 das destruktive Potential von Tsunamis, die auf menschliche Siedlungen treffen, gezeigt. Die Überflutung von trockenem Land ist der am besten bekannte Schaden, aber Tsunamis verändern auch die Küstenmorphology, zumindest zeitweise. In den meisten Fällen verschwinden solche Veränderungen innerhalb von einigen Monaten oder Jahren. Diese Arbeit versucht ein besseres Verständnis des Phänomens Tsunami und seiner Auswirkungen auch über die Wellenhöhen hinaus aufzuzeigen mit Hilfe der Modellierung der Morphodynamik von Tsunamis. Zuerst wurde eine Modellierungsstudie durchgeführt, die die möglichen Folgen von Tsunamis in der Nordsee und in der Deutschen Bucht betrachten, eingeschlossen ein Storegga-ähnliches Szenario. Es wurden durch Tsunamis bedingte Strömungen modelliert und mit denen von Sturmfluten in der Nordsee und der deutschen Bucht verglichen. Es zeigte sich, dass Tsunami-Wasserstände niedriger als diejenigen von Sturmfluten waren, allerdings waren die Strömungsgeschwindigkeiten vergleichbar und Tsunamis wirkten innerhalb kürzerer Zeitspannen. Zweitens wurde eine Parameterisierung von Tsunamis mit Hilfe von N-Wellen erprobt. Die morphologischen Änderungen, die von den Wellen verursacht wurden, hingen von deren Ausrichtung ab. Strömungsgeschwindigkeiten von Tsunamis und morphologische Änderungen reagierten empfindlicher gegenüber der Wellenform als der Wellenauflauf, was die Erstellung einer Verallgemeinerung erschwerte. Drittens schließlich wurden dreidimensionale morphologische Änderungen für Tamil Nadu an der Ostküste Indiens simuliert, die ein Tsunami vergleichbar mit dem Tsunami im Indischen Ozean von 2004 verursachen würde. Das Untersuchungsgebiet war eine offene Küstenlinie und die Modellierungsergebnisse zeigten eine Abflachung des Meeresbodens und eine Verbreiterung des Strandes, beides Effekte, die während des Tsunamis im Indischen Ozean von 2004 dokumentiert wurden. Die Ergebnisse, die in dieser Thesis gewonnen wurden, zeigen, dass weiterhin ein großer Forschungsbedarf in der Modellierung der Morphodynamik von Tsunamis besteht. Es gibt keine spezifischen Gleichungen für den Sedimenttransport durch Tsunamis und für die Modellierung der Morphodynamik von Tsunamis werden weit mehr Daten benötigt als für die Modellierung der Hydrodynamik. Trotzdem zeigen die Ergebnisse auch, dass die morphodynamische Modellierung von Tsunamis unter diesen Einschränkungen durchgeführt werden kann, allerdings mit eingeschränkter Zuverlässigkeit. Somit enwickelt sich die Modellierung der Morphodynamik von Tsunamis zu einem nützlichen Werkzeug, um das Verhalten von Tsunamis zu verstehen und um Schäden zu prognostizieren.

Keywords: *Tsunami, morphologische Veränderungen, Tsunami-Ablagerungen, N-Wellen, Nordsee, Tsunami von 2004 im Indischen Ozean*

Resumen

La población costera se incrementa constantemente y toda está expuesta a tsunamis. Recientemente los tsunamis del Océano Índico del 2004 y de Japón del 2011 han mostrado el potencial destructivo de los tsunamis al interactuar con los asentamientos humanos. El efecto más conocido de los tsunamis es la inundación, sin embargo los tsunamis también tienen la capacidad de cambiar la morfología costera, al menos temporalmente. En la mayoría de los casos dichos cambios desaparecen en pocos meses o años. Este trabajo busca lograr un mayor entendimiento de los tsunamis y sus consecuencias más allá de su altura, por medio del modelado de la hidrodinámica y morfodinámica asociadas. Primero se exploraron las posibles consecuencias de un tsunami en el Mar del Norte y la costa alemana incluyendo un escenario similar al del tsunami de Storegga. Se modelaron las velocidades de las corrientes causadas por tsunamis y se compararon con aquellas causadas por surgencias de tormentas en el Mar del Norte y la costa alemana. Se obtuvo que las alturas de inundación por tsunami fueron menores que por tormentas pero las velocidades de corriente fueron comparables y los tsunamis actuaron durante períodos más cortos de tiempo. En segundo lugar se intentó parametrizar los tsunamis usando ondas N. Se encontró que los cambios morfológicos causados por las ondas dependían de su orientación. Se encontró que las velocidades de corriente de los tsunamis y los cambios morfológicos que estos causan son más sensibles que la altura del tsunami a la forma de la onda, dificultando el realizar una generalización. En tercer lugar se simularon los cambios morfológicos causados en Tamil Nadu, en la costa oriental de India, por un tsunami similar al de Indonesia de 2004 por medio de un modelo numérico tridimensional. La región estudiada era una costa abierta y los resultados del modelo mostraron un aplanamiento del fondo marino y un ensanchamiento de la playa, ambos efectos fueron documentados durante el tsunami del 2004. Los resultados obtenidos en esta tesis mostraron que aún queda mucho trabajo que realizar en el modelado de la morfodinámica de tsunamis. No hay ecuaciones específicas para el transporte de sedimentos por parte de tsunamis y se requieren muchos más datos para modelar la morfodinámica de tsunamis que para modelar su hidrodinámica. Sin embargo, los resultados también mostraron que se puede realizar el modelado numérico de la morfodinámica de tsunamis con una certidumbre reducida aún con esas limitaciones. Entonces el modelado numérico de la morfodinámica de tsunamis se perfila como una herramienta útil para entender el comportamiento de los tsunamis y pronosticar sus consecuencias.

Keywords: *tsunami, cambios morfológicos, depósitos causados por tsunami, modelado de la morfodinámica de tsunamis, ondas N, Mar del Norte, tsunami del Océano Índico del 2004*

Table of Contents

Figures

Tables

Notation

a	Position of the reference level over the bed
$A^{(m,n)}$	Area of cell (m,n)
B_k	Buoyancy term of turbulent kinetic energy
B_ε	Buoyancy term of the dissipation rate of turbulent kinetic energy
Bsed	Total number of sediment fractions present on the modelling
$c = \sqrt{gH}$	Shallow Water Waves propagation speed
C	Chézy friction coefficient
c_D=0.1925	Constant
$c_{1\varepsilon}$=1.44	Constant
$c_{2\varepsilon}$=0.1.92	Constant
$c_{3\varepsilon} = \begin{cases}0\\1\end{cases}$	Constant for unstable stratified flows Constant for stable stratified flows
c_μ=0.11115	Constant
$c_a^{(b)}$	Reference concentration of sediment fraction (b)
$c_{kmx}^{(b)}$	Concentration at kmx layer of sediment fraction (b)
$c_{kmx,b}^{(b)}$	Concentration at the bottom of the kmx layer of sediment fraction (b)
$c_s^{(b)} or\ c^{(b)}$	Concentration of sediment fraction (b)
c_s^{total}	Total concentration of sediment
C_{soil}	Reference density
CFL	Courant-Friedrichs-Lewy condition
$D_{50}^{(b)}$	Medium sediment size for sediment fraction (b)
$D_*^{(b)}$	Non-dimensional particle diameter for sediment fraction (b)
D_k	Turbulent kinetic energy eddy diffusivity
D_ε	Dissipation rate of turbulent kinetic energy eddy diffusivity
$D^{(b)}$	Deposition rate for sediment fraction (b)
$D_s^{(b)}$	Medium sediment diameter of sediment fraction (b)
$E^{(b)}$	Erosion rate for sediment fraction (b)
f	Friction coefficient
f_R	Riemann invariant
f_c'	Gain related friction factor
f_c	Total current related friction factor

g	Gravity acceleration
H_0	Maximum height of the incoming wave
$h(x,y)$ or h	Still water depth
$H=h+\eta$	Total water depth
Im	Imamura number
k	Kinematic turbulent energy
k_s	Nikuradse equivalent sand roughness or surface roughness height
K_s	Equivalent sand diameter
L	Mixing length
$\vec{M} = M\hat{\boldsymbol{\imath}} + N\hat{\boldsymbol{\jmath}} = H\vec{u}$	Horizontal discharge flux
$M=uH$	x-direction discharge flux
$M^{(b)}$	Sediment mobility number
$M_e^{(b)}$	Excess sediment mobility number
n	Manning's coefficient
$N=vH$	y-direction discharge flux
p	Pressure
P_k	Productivity term of turbulent kinetic energy
P_ε	Productivity term of the dissipation rate of turbulent kinetic energy
$s^{(b)} = \dfrac{\rho_s^{(b)}}{\rho_w}$	Relative density of sediment fraction (b)
$S_{b,uu}^{(m,n)}$	Bed load transport on the grid cell (m,n) on the direction uu
t	Time
t_0	Constant determining middle point of the N-wave
T_a	Non-dimensional bed shear stress
$\vec{u} = u\hat{\boldsymbol{\imath}} + v\hat{\boldsymbol{\jmath}}$	Horizontal flow velocity vector
$\vec{U} = U\hat{\boldsymbol{\imath}} + V\hat{\boldsymbol{\jmath}}$	Horizontal depth-averaged flow velocity vector
$\overrightarrow{u_b} = u_b\hat{\boldsymbol{\imath}} + v_b\hat{\boldsymbol{\jmath}}$	Horizontal flow velocity vector at the first σ-layer above the bed
u	x-direction flow velocity
u_*	Friction velocity due to currents
$u_{*,c}$	Local bed shear stress
U	x-direction depth-averaged flow velocity
v	y-direction flow velocity
V	y-direction depth-averaged flow velocity
w	Vertical velocity defined at iso σ-surfaces
$w_{s,0}^{(b)}$	Free settling velocity of sediment fraction b

$w_s^{(b)}$	Hindered settling velocity of sediment fraction b
x, y	Horizontal axis
z	Vertical axis, referenced to the mean sea level, negative above and positive below
z_{kmx}	Position of the kmx layer over the bed
α_1	Correction factor
$\alpha_2^{(b)}$	Correction factor for sediment concentration of sediment fraction (b)
$\beta_{eff}^{(b)}$	Effective Van Rijn beta factor of sediment fraction (b)
γ	Constant determining the width of the N-wave
ε	Dissipation rate of turbulent kinetic energy
ε_f	Vertical fluid mixing coefficient
$\varepsilon_{s,x}^{(b)}, \varepsilon_{s,y}^{(b)}, \varepsilon_{s,z}^{(b)}$	Eddy diffusivities of sediment fraction m
$\eta(x,y,t)$ or η	Displacement of the free surface
$\mu_c = {f'_c}/{f_c}$	Efficiency factor
$\nu_{3D} = c_\mu \frac{k^2}{\varepsilon}$	Part of eddy viscosity from the turbulence closure model in the vertical direction
ν_{mol}	Kinematic (molecular) viscosity
ν_H	Horizontal eddy viscosity
ν_V	Vertical eddy viscosity
ρ	Fluid density
ρ_{mix}	Density of the water-sediment mix at a given salinity and temperature
$\rho_{sed}^{(b)}$	Density of the sediment fraction (m)
ρ_w	Water density
σ	Vertical coordinate on the σ-coordinate system, $\sigma=-1$ at the bottom and $\sigma=0$ at the free surface
σ_{mol}	Prandtl-Schmidt number for molecular mixing
ω	z-direction flow velocity
τ_{cr}	Critical bed shear stress
τ_{ii}	Component ii of the stress tensor, where i can be x, y or z
$\vec{\tau} = \tau_x \hat{\boldsymbol{\imath}} + \tau_y \hat{\boldsymbol{\jmath}}$	Bed shear stress
$\Delta_{SED}^{(m,n)}$	Change on the available sediment on the bottom of grid cell (m,n)
Δt	Time-step on the modelling

Δx, Δy	Size of the grid cell on (x,y) directions respectively
$\Delta z = z_{kmx} - a$	Difference between the position of the kmx layer over the bed and the reference height

Acknowledgments

- To the Survey of India and the National Institute of Oceanography of India for the tide-gauge data of the 2004 tsunami in the Indian subcontinent and the beach profiles at the East Coast of India.
- To the NOAA / PMEL / Center for Tsunami Research for the altimetry data and references of the 2004 tsunami in the Indian Ocean.
- To the National University of Costa Rica (UNA) and the Deutscher Akademischer Austausch Dienst (DAAD) for the scholarship that made this work possible.
- To all reviewers that contributed to improve this work.

1. Introduction

1.1. General problem definition

A deeper understanding of a natural phenomenon might help to save lives, even in such a low-frequency event as tsunamis. Traditionally tsunami research has been focused on tsunami generation, propagation and inundation. However, the erosion and deposition caused by tsunamis is also responsible of damages and has become an active study field in the last decades. The ability of forecast where a tsunami might cause erosion and/or deposition can become very useful on the design of near-shore infrastructure in the future.

When the XXI century began only some people living mostly in the Pacific basin knew about tsunamis. But two major events summing about 250,000 deaths (NGDC/WDC, 2011) in the middle of the technology and globalization era have made that nowadays people from all over the world are aware of this natural phenomenon. Both tsunamis, Indian Ocean 2004 and Japan 2011, have caused a major impression worldwide because of both the magnitude of the damage and the amount of graphical testimonies that have circulated in the internet and the news. Most of the videos and pictures taken in 2004 were made by tourists, so they were recorded from ground level and in some cases from balconies, and their quality is not the best. But the videos and pictures of the Japanese tsunami amazed the world because of their sharpness and because several of them were taken from the air or elevated places (Asian Tsunami Videos, 2011). In many videos from this recent tsunami is possible to see the debris wave advancing through the villages, becoming obvious that a tsunami does not mean only moving water, but all the things it drags within.

In some regions of the world several geomorphological records can be attributed to tsunamis arriving there prior population were established, for example Australia, New Zealand, Scotia, and these records are also tsunami data. One example is the North Sea, where sediment deposits attributed to tsunamis allowed the confirmation that a large tsunami affected that basin 8,000 years before present (DAWSON, 1999). The study of geomorphological records caused by recent tsunamis can be applied to records of paleotsunamis in order to obtain more information about the tsunamis that caused them. So far, these records only provide information on the tsunami occurrence and its minimum penetration. To be able to obtain quantitative information about tsunami geomorphological records it is necessary to gain more knowledge on tsunami morphodynamics.

1.2. Aims and objectives

This thesis seeks to improve the understanding of tsunami hydrodynamics and morphodynamics through numerical modelling, toward contribute to the development of a strategy to model coastal development due to tsunamis.

Several model configurations were employed including two- and three-dimensional modelling, different ways to impose the forcing, different types of forcing, etc.

Three main objectives of the thesis are:

1. To determine the tsunami risk for the German Bight.
2. To explore if tsunami morphodynamics may be modelled by N-waves.
3. To perform a three-dimensional modelling of tsunami morphodynamics in an open coastline and compare it with two-dimensional modelling.

1.3. Justification

In all the simulations performed here Delft3D model was chosen as the hydrodynamic and morphodynamic calculations are coupled in both directions, a condition not met by other models employed in tsunami morphodynamics so far.

1.3.1. Tsunami risk for the German Bight

Approximately 80% of tsunamis occur at the Pacific Ocean; however, after the 2004 Indonesia tsunami became clear that destructive basin-wide tsunamis do not happen only in that basin. Despite the tsunami antecedents on the Indian Ocean, there was no tsunami warning system by that time and neither tsunami educational and awareness programs. These circumstances, together with the tsunami size, were responsible for the highest death toll on recorded tsunami history (NGDC/WDC, 2011). After this, scientists all over the world started to consider tsunami risk on other basins, as tsunami antecedents were found on all the world’s oceans. For example the Caribbean Sea has important seismic and volcanic activity, and records of several tsunamis in the past. Also the North Sea has important tsunami records. In both seas meteorological phenomena such as storms and hurricanes are much more common and tangible. Countries along both seas have been traditionally well prepared for the effects of those phenomena but ten years ago there was absolutely no tsunami preparedness at any of them.

Since the 2004 tsunami, the tsunami risk was estimated to be high enough at the Caribbean Sea to justify the creation of a tsunami warning system (UNESCO/IOC, 2014a). The same happened at Europe, where a tsunami warning system was created for the Mediterranean Sea and the Northeast Atlantic (UNESCO/IOC, 2014b). The North Sea is included on the last one, yet the risk appears to be minor there, as it does not have subduction zones or active volcanoes within. Nevertheless, there is plenty of evidence of the impact of tsunamis originated both inside and outside the North Sea basin. The most renowned tsunami in the North Sea was generated by the second Storegga submarine slide about 8,000 years ago in the Norwegian Sea (HARBITZ, 1992). Besides this event, the NOAA Global Historical Tsunami Database (NGDC/WDC, 2011) includes other tsunami records for Germany, for example a tsunami in Germany and Denmark in 1760 which was attributed to a local earthquake. Also, there are reports in this database for tsunamis in the United Kingdom, France and the Netherlands in 1755 and 1761 caused by earthquakes from the offshore area of Portugal in the Atlantic (NGDC/WDC, 2011). There is still an open question about the tsunami risk for the German Bight and whether a tsunami affecting the German Bight, might have stronger or weaker effects than the storm surges so common in this region. The effects of these storm surges include inundation of dry land and damages and morphological changes due to strong currents.

As the information on tsunamis on the North Sea is scarce it was not possible to use real sources on most of the experiments performed there, and a parameterization of the leading wave of tsunamis was chosen instead. At the first set of experiments (Chapter 3) N-waves were used for the modelling of tsunami propagation through the North Sea and inundation of the German Bight to assess the tsunami risk for the German Bight.

1.3.2. N-waves as a parameterization of the leading wave of tsunamis

The Nicaragua and the Indonesia tsunamis of 1992 had a clear leading depression shape, questioning the representation of tsunamis as solitary waves employed until that date (TADEPALLI and SYNOLAKIS, 1994). Most tsunamis are caused by earthquakes, and coseismic deformations have two poles: elevation and subsidence, meaning that their cross-sections look like an N-wave. N-waves are bipolar non periodic waves: they have an elevation and a depression. Isosceles N-waves are a type of N-waves having elevation and depression of the same amplitude. There are several formulations of N-waves, all of them based on a combination of exponential functions.

The modelling of tsunami morphodynamics using N-waves could be sufficient to obtain general results, if the analogy with the modelling of tsunami propagation and inundation sustains. General results are important in the understanding of tsunami behaviour and can be applied on the design of coastal structures and zoning. The aim of the second set of experiments (Chapter 5) is to perform a first attempt on examining N-waves for their suitability to model the sediment transport and morphological changes caused by tsunamis.

N-waves were employed in this thesis to assess the tsunami risk on the German Bight by simulating tsunami heights and velocity flows on the first set of experiments described in Chapter 3. However, to the knowledge of the author, there are no substantial studies available on morphological changes caused by N-waves or on the suitability of N-waves for simulating morphological changes caused by tsunamis. So far, modelling of tsunami-caused morphological changes has been done with real tsunami shapes, which are specific for each tsunami at each location (APOTSOS et al., 2009), (APOTSOS et al., 2011b).

1.3.3. Tsunami morphodynamics on an open coastline, simulated by a three-dimensional model

Despite the limitations, the modelling of tsunami morphodynamics considering the vertical dimension has been somewhat successful, but it has been performed mostly along a channel (2DV) or on ports and harbours. There are no studies on three dimensional modelling of tsunami morphodynamics on open coastlines, neither on the assessment of performance of comparable three-dimensional and two-dimensional models. The aim of the third set of experiments (Chapter 6) is to approach those questions by one case-study.

1.4. Outline

This thesis is composed by seven chapters. In Chapter 1 the general problem is discussed, together with the aim and objectives of the research and their justification.

In Chapter 1 are defined the basic concepts of tsunamis, tsunami modelling and tsunami morphodynamics as well as the numerical model Delft3D.

In Chapter 2 there is review of the state of the art on the modelling of tsunami hydro- and morphodynamics.

Chapter 3 presents the numerical experiments performed at the North Sea and German Bight and their results. In Chapter 5 are described several numerical experiments performed to explore the suitability of N-waves on modelling tsunami morphodynamics. Chapter 6 presents the three-dimensional modelling on an open coastline due to a tsunami similar to 2004 Indian Ocean tsunami.

Chapter 7 gives general conclusions of the experiments and Chapter 8 lists the references employed in this thesis.

2. Theoretical background and the numerical model

2.1. Basic definitions

Tsunamis are surface gravity waves, meaning that they travel through the water surface and their restoring force is the gravity, as they are caused by a sudden perturbation of the water surface. The most common source of tsunamis are submarine earthquakes which deform the ocean bottom; this deformation is transmitted to the water surface provoking a tsunami. Other causes are aerial and submarine landslides, volcano eruptions, meteorites, and abrupt changes on the atmospheric pressure. Therefore, tsunamis can happen in any water body including lakes.

According with the Intergovernmental Oceanographic Commission of UNESCO (2013), tsunami inundation is defined as the horizontal distance from the original coastline to the point of maximum tsunami penetration. And tsunami runup is defined as the height of the inundation limit above the original sea level at the time of the tsunami (Figure 2-1). Both quantities are measured when there is a clear indication of the inundation limit and they vary for different locations. The runup is not necessarily the maximum tsunami height at a given place, as the latter is very difficult to measure: it can only be inferred if there are flow markers like buildings or trees with clear water marks still standing (IOC, 2013).

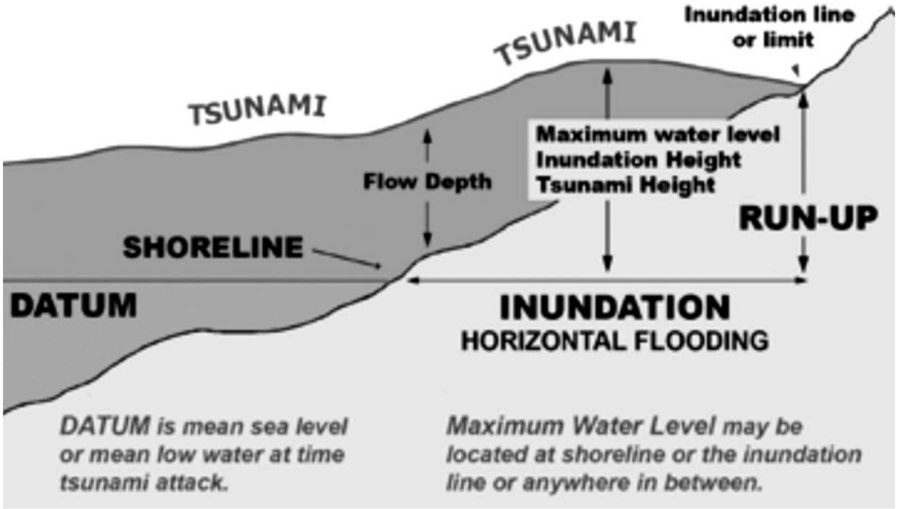

Figure 2-1. Tsunami terminology. Taken from Tsunami Glossary of the Intergovernmental Oceanographic Commission (2013)

2.2. The σ coordinate system

For three-dimensional modelling purposes, the vertical direction σ-coordinate system (PHILLIPS, 1957) was employed here, instead of the Cartesian coordinates system. In this system the horizontal coordinates are the same as in the Cartesian system, but the vertical direction is divided in σ-layers, which are considered to follow the bed level and the water surface. In this way, the bathymetry is represented smoothly and not step-wise as in the Cartesian system. Here, σ-layers were defined thinner close to the bottom to have more resolution on the processes near the bottom.

The coordinate σ is defined as:

$$\sigma = \frac{z-\eta}{h+\eta} = \frac{z-\eta}{H}. \qquad \textbf{2-1}$$

where z is the vertical Cartesian coordinate, η is the displacement of the water free surface, h is the still water depth and H=h+η is the total water depth. At the free surface $\sigma = 0$ and at the bottom $\sigma = -1$ (DELFT HYDRAULICS, 2010, p.195).

2.3. Equations of motion

To obtain the equations of motion for propagation and inundation of tsunamis it is possible to start with the Navier-Stokes equations, as Earth’s rotation can be neglected on tsunami propagation. When the Boussinesq approximation and scale simplifications are applied, the equations in Cartesian coordinates become:

$$\frac{\partial \mathrm{u}}{\partial x} + \frac{\partial \mathrm{v}}{\partial y} + \frac{\partial \mathrm{w}}{\partial z} = 0, \qquad \textbf{2-2}$$

$$\frac{\partial u}{\partial t} + u\frac{\partial u}{\partial x} + \mathrm{v}\frac{\partial u}{\partial y} + \mathrm{w}\frac{\partial u}{\partial z} = -\frac{1}{\rho}\frac{\partial p}{\partial x} + \frac{1}{\rho}\left(\frac{\partial \tau_{xx}}{\partial x} + \frac{\partial \tau_{xy}}{\partial y} + \frac{\partial \tau_{xz}}{\partial z}\right), \qquad \textbf{2-3}$$

$$\frac{\partial \mathrm{v}}{\partial t} + u\frac{\partial \mathrm{v}}{\partial x} + \mathrm{v}\frac{\partial \mathrm{v}}{\partial y} + \mathrm{w}\frac{\partial \mathrm{v}}{\partial z} = -\frac{1}{\rho}\frac{\partial p}{\partial y} + \frac{1}{\rho}\left(\frac{\partial \tau_{xy}}{\partial x} + \frac{\partial \tau_{yy}}{\partial y} + \frac{\partial \tau_{yz}}{\partial z}\right), \qquad \textbf{2-4}$$

$$0 = -\frac{\partial p}{\partial z} - \rho g, \qquad \textbf{2-5}$$

where (x,y,z) are the Cartesian coordinates, t is time, (u,v,w) are the components of the velocity vector, p is the pressure, ρ is the flow density, g is the gravity acceleration and τ_{xx}, τ_{xy}, τ_{yy}, τ_{xz}, and τ_{yz} are components of the stress tensor (DELFT HYDRAULICS, 2010, p.197). The equations are shown in Cartesian coordinates for simplicity, but spherical coordinates are employed when the propagation over long distances is simulated; and in those cases also the σ-coordinate system can be chosen to represent the vertical dimension.

The shallow water approximation implies that the horizontal scale of motion is much larger than the vertical scale. Tsunamis are widely modelled as long or shallow water waves, because their wave length is much longer than the depth in which they propagate (LEVIN and NOSOV, 2009, p.198). The Shallow Water Equations (SWE) reproduce well the propagation of tsunamis over small distances (MURTY and KOWALIK, 1993). SWE are widely used to simulate tsunami propagation over any distance, even when they cannot reproduce the dispersion experienced by tsunamis after travelling long distances (LEVIN and NOSOV, 2009, p.198-199). SWE are employed because they reproduce the tsunami propagation well enough (SYNOLAKIS et al., 2008) and their numerical solution is much simpler than Boussinesq equations, which would be more physically accurate. Most of the numerical models for tsunami propagation and inundation are based on the depth-averaged Shallow Water Equations (SWE), which consider no wave dispersion (Section 2.4). SWE are usually discretized to finite differences (GOTO et al., 1997), (PMEL, 2006).

Delft3D system of numerical models of WL|Delft Hydraulics (STELLING and DUINMEIJER, 2003) was used for all the hydrodynamic and morphodynamic simulations on this thesis. Delft3D-FLOW solves the Shallow Water equations both two-dimensionally and three-dimensionally using finite differences and an alternating directions implicit method (ADI) for the continuity and horizontal momentum equations (LEENDERTSE, 1987).

For the horizontal advections terms Delft3D offers several options. One of them is the named “Flood Scheme” which was developed for the inundation of dry land (DELFT HYDRAULICS, 2010, p.p. 94) and was employed on the experiments performed here. This scheme is based upon: “1. Mass conservation combined with no-negative water depths, 2. Momentum balance in flow expansion and 3. Energy head conservation in strong contractions” (STELLING and DUINMEIJER, 2003). In this scheme, the integration of the advection term is explicit and the time step is restricted by the Courant number to be less than one (DELFT HYDRAULICS, 2010, p.p. 94). Then the grid employed must fulfil the Courant-Friedrichs-Lewy stability condition of the time step being smaller than the time for the wave to cross one cell. In one dimension this is:

$$CFL = \frac{\Delta t}{\Delta x}\sqrt{gh} < 1, \tag{2-6}$$

where Δt is the model time step and Δx is the grid step. Delft3D has an algorithm incorporated to calculate CFL in each grid point of the horizontal grid.

2.4. Two-dimensional equations

The depth-averaged SWE are obtained integrating Eq. 2-2 to 2-4 over the vertical, from $z = -h$ to $z = \eta$. These equations in Cartesian coordinates are (IMAMURA et al., 2006):

$$\frac{\partial \eta}{\partial t} + \frac{\partial M}{\partial x} + \frac{\partial N}{\partial y} = 0, \tag{2-7}$$

$$\frac{\partial \mathrm{M}}{\partial t} + \frac{\partial}{\partial x}\left(\frac{M^2}{H}\right) + \frac{\partial}{\partial y}\left(\frac{MN}{H}\right) + gH\frac{\partial \eta}{\partial x} + \frac{\tau_x}{\rho} = \nu_H\left(\frac{\partial^2 M}{\partial x^2} + \frac{\partial^2 M}{\partial y^2}\right), \tag{2-8}$$

$$\frac{\partial N}{\partial t} + \frac{\partial}{\partial x}\left(\frac{MN}{H}\right) + \frac{\partial}{\partial y}\left(\frac{N^2}{H}\right) + gH\frac{\partial \eta}{\partial y} + \frac{\tau_y}{\rho} = \nu_H\left(\frac{\partial^2 N}{\partial x^2} + \frac{\partial^2 N}{\partial y^2}\right), \tag{2-9}$$

where (M,N) are the components of the discharge flux $\vec{M}$, (τ_x, τ_y) are the bed shear stresses, and ν_H is the horizontal eddy viscosity which is assumed to be constant in space. For the propagation of tsunamis only, the eddy turbulence is considered to be negligible compared to the bottom friction (IMAMURA et al., 2006). Then, the right term in Eq. 2-8 and 2-9 vanishes. The non-linear Shallow Water Equations are solved numerically by Delft3D when the two-dimensional mode is selected.

As mentioned before, tsunamis as Shallow Water Waves or Long Waves are not dispersive and their propagation speed, c, depends only on the water depth by:

$$c = \sqrt{g(h + \eta)}. \tag{2-10}$$

Consequently tsunamis experiment reflections and refractions due to bathymetric features. Some locations have proved to amplify tsunamis like Hilo Bay in Hawaii and Crescent City in California, due to their topographic and bathymetric characteristics.

Also, as Shallow Water Waves, their flow velocity remains uniform over the vertical, except near the bottom where decreases due to friction forming a thin boundary layer. Then, the flow velocity considered in the model is the depth-averaged flow velocity.

Because of the depth-averaged approach employed in the two-dimensional case, the shear stress applied by the bed over the flow is considered as an external force applied over the flow in the horizontal momentum equations (Eq. 2-8 and 2-9) and can be written as:

$$\frac{\vec{\tau}}{\rho} = \frac{g}{C^2}\left|\vec{U}\right|\vec{U}, \tag{2-11}$$

where $\vec{U}$ is the depth-averaged horizontal velocity and C is the Chézy friction coefficient, which can be computed by various bed roughness formulations (IMAMURA et al., 2006).

2.5. Three-dimensional equations of motion

When the shallow water approximation is applied and variations over the vertical direction are considered by means of the σ-coordinate system, the horizontal momentum (Eq. 2-3 and 2-4) and the continuity (Eq. 2-2) equations become:

$$\begin{aligned}\frac{\partial \mathrm{u}}{\partial t} + \mathrm{u}\frac{\partial \mathrm{u}}{\partial x} + \mathrm{v}\frac{\partial \mathrm{u}}{\partial y} + \frac{\omega}{h+\eta}\frac{\partial \mathrm{u}}{\partial \sigma} \\ = -g\frac{\partial \eta}{\partial x} + \nu_H\left(\frac{\partial^2 \mathrm{u}}{\partial x^2} + \frac{\partial^2 \mathrm{u}}{\partial y^2}\right) + \frac{1}{(h+\eta)^2}\frac{\partial}{\partial \sigma}\left(\nu_V\frac{\partial \mathrm{u}}{\partial \sigma}\right),\end{aligned} \tag{2-12}$$

$$\begin{aligned}\frac{\partial \mathrm{v}}{\partial t} + \mathrm{u}\frac{\partial \mathrm{v}}{\partial x} + \mathrm{v}\frac{\partial \mathrm{v}}{\partial y} + \frac{\omega}{h+\eta}\frac{\partial \mathrm{v}}{\partial \sigma} \\ = -g\frac{\partial \eta}{\partial y} + \nu_H\left(\frac{\partial^2 \mathrm{v}}{\partial x^2} + \frac{\partial^2 \mathrm{v}}{\partial y^2}\right) + \frac{1}{(h+\eta)^2}\frac{\partial}{\partial \sigma}\left(\nu_V\frac{\partial \mathrm{v}}{\partial \sigma}\right),\end{aligned} \tag{2-13}$$

$$\frac{\partial \eta}{\partial t} + \frac{\partial[(h+\eta)\mathrm{u}]}{\partial x} + \frac{\partial[(h+\eta)\mathrm{v}]}{\partial y} + \frac{\partial \omega}{\partial \sigma} = 0. \tag{2-14}$$

where ω is the vertical velocity in the σ-coordinates and ν_V is the vertical eddy viscosity (DELFT HYDRAULICS, 2010, p.197). In the three-dimensional modelling the turbulent motion cannot be neglected. The turbulent eddy viscosity coefficients include the effect of molecular viscosity, Reynolds stresses and unresolved motions, which are always present on numerical modelling due to discretization (CUSHMAN-ROISIN and BECKERS, 2011). The horizontal eddy viscosity is significantly larger than the vertical because horizontal scales are much larger than vertical scales. The eddy viscosities are not necessarily homogeneous and their calculation is done through turbulence closure models as will be explained in Section 2.7.

The vertical velocity ω is defined relative to the moving σ plane, associated with up- or downwelling motions. The vertical velocity in the z-coordinate (w), the physical velocity, is not employed on the three-dimensional formulation with σ-coordinates. However, both vertical velocities can be related through:

$$\mathrm{w} = \omega + u\left(\sigma\frac{\partial H}{\partial x} + \frac{\partial \eta}{\partial x}\right) + \mathrm{v}\left(\sigma\frac{\partial H}{\partial y} + \frac{\partial \eta}{\partial y}\right) + \left(\sigma\frac{\partial H}{\partial t} + \frac{\partial \eta}{\partial t}\right) \tag{2-15}$$

(DELFT HYDRAULICS, 2010, p.198). The hydrostatic pressure equation in the σ coordinates becomes (DELFT HYDRAULICS, 2010, p.198):

$$\frac{\partial p}{\partial \sigma} = -g\rho H = -g\rho(h+\eta). \tag{2-16}$$

In the three-dimensional formulation, the bottom friction is incorporated as a boundary condition at the ocean bottom (DELFT HYDRAULICS, 2010, p.209):

$$\frac{\nu_V}{H}\frac{\partial}{\partial \sigma}(\mathrm{u},\mathrm{v})\bigg|_{\sigma=-1} = \frac{1}{\rho}\left(\tau_x, \tau_y\right), \tag{2-17}$$

where (τ_x, τ_y) can be obtained from:

$$\vec{\tau} = \frac{\rho g |\overrightarrow{u_b}|}{C^2}\overrightarrow{u_b}, \tag{2-18}$$

and $\overrightarrow{u_b}$ is the velocity at the first σ-layer above the bed, which is considered to be horizontal (DELFT HYDRAULICS, 2010, p.211):

$$\overrightarrow{u_b} = \overrightarrow{u_*}\ln\left(1 + \frac{\Delta z_b}{2z_0}\right), \tag{2-19}$$

where Δz_b is the distance to the computational point closest to the bed and z_0 is user defined. And then for numerical calculations, the bottom stress is:

$$|\vec{\tau}| = \rho_0 |\overrightarrow{u_*}| \overrightarrow{u_*}, \tag{2-20}$$

where $\overrightarrow{u_*}$ is the friction velocity due to currents.

Even when Eq. 2-11 and 2-18 have the same structure, there is an important difference between them: the horizontal velocity employed to calculate the bed shear stress. For the two-dimensional case is used the depth-averaged velocity and for the three-dimensional case is used the bottom velocity.

For the three-dimensional case the Chézy friction coefficient C can be related with the roughness height; however, this relationship is not valid for unsteady flows as tsunamis (DELFT HYDRAULICS, 2010, p.212).

2.6. Manning formulation for bed roughness

The most widely used bed roughness formulation for tsunami modelling is Manning formulation, which has been verified for these purposes due to its adequate performance on many tsunami numerical modelling studies. Manning formulation is employed on tsunami-specific numerical models, being some of the most widely used TUNAMI (GOTO et al., 1997), MOST (PMEL, 2006) and NEOWAVE (YAMAZAKI et al., 2009).

On Manning formulation the Chézy friction coefficient is given by (DELFT HYDRAULICS, 2010, p.210):

$$C = \frac{(h+\eta)^{1/6}}{n}, \tag{2-21}$$

where n is the Manning’s coefficient. Then the terms on Eq. 2-8 and 2-9 for the two-dimensional case, become:

$$\frac{\tau_x}{\rho} = \frac{gn^2}{(h+\eta)^{7/3}} M\sqrt{\mathrm{M}^2+\mathrm{N}^2}, \tag{2-22}$$

$$\frac{\tau_y}{\rho} = \frac{gn^2}{(h+\eta)^{7/3}} N\sqrt{\mathrm{M}^2+N^2}. \tag{2-23}$$

And Eq. 2-18 for the three-dimensional case becomes

$$\vec{\tau} = \frac{\rho g n^2}{(h+\eta)^{1/3}} |\overrightarrow{u_b}|\overrightarrow{u_b}. \tag{2-24}$$

Manning formulation was obtained empirically for channels, and the values of Manning’s coefficient, n, were also obtained empirically by measurements on rivers and channels. Therefore the values of Manning's n on hydraulic textbooks are referred to them. Still, Manning formulation can be applied to tsunamis. Table 10.1 in Imamura (2009) gives n=0.025m$^{-1/3}$s for Natural Coast and Channels and Rivers, and the same value is given for a “coast free from dense vegetation” in Levin and Nosov (2009, p.214). The first reference found for this value of Manning coefficient on tsunami modelling was in Bretschneider and Wybro (1976), although it was not possible to find an explanation on how it was obtained. On Titov et al. (2003) they wrote “In the absence of proven scientific estimates, we have chosen to use a standard engineering value for the Manning parameter corresponding to mildly rough surfaces (n = 0.025 (sic)). That approach gives credible conservative estimates of the tsunami inundation". This value of n=0.025m$^{-1/3}$s has been widely validated through comparison of numerical model results with tsunami records and observations, for example Mercado and McCann (1998), Gusman et al. (2014), and with tsunami deposits as in Apotsos et al. (2011a). On some modelling studies, values between n=0.02m$^{-1/3}$s and n=0.03m$^{-1/3}$s are also used offshore, as in Lynett et al. (2012), Satake (1995), Dao and Tkalich (2007), Apotsos et al. (2009), Dengler and Uslu (2011), and PMEL (2006). In some cases values between n=0.032 m$^{-1/3}$s and n=0.04m$^{-1/3}$s are employed inland, as in Apotsos et al. (2011a), (2011c).

The bed friction coefficient includes the effect of skin friction, bedforms, and suspended sediments, among others. The author supposes that the value of Manning coefficient employed on tsunami modelling does not have the significance of the original theory of channels and rivers, but it is implicitly including other effects caused by the large velocities of tsunami flow. For example, the destructiveness which will reduce the resistance to the flow, or the high amount of suspended sediment or the small time-scale of the phenomena. It is very hard to quantify these effects, and it could be that this value of Manning's coefficient is doing it in a certain way. After all, the values of friction coefficients given on textbooks for channels and rivers were also obtained empirically.

2.7. Turbulence

In three-dimensional modelling, the eddy viscosity includes the effects of molecular viscosity, two-dimensional turbulence and three-dimensional turbulence (DELFT HYDRAULICS, 2010, p.223). The two-dimensional turbulence part is originated because the horizontal grid step and time step are always too large to solve all the turbulence processes present on the flow. The three-dimensional part is computed by the turbulence closure model. For all the simulations performed here the k-ε model was chosen. In this second-order turbulence closure model the mixing length L is calculated from the turbulent kinetic energy k and the dissipation rate of turbulent kinetic energy ε:

$$L = c_D \frac{k\sqrt{k}}{\varepsilon}, \tag{2-25}$$

where c_D=0.1925 is a constant. The values of k and ε are calculated from transport equations. This closure model does not require the use of a damping function "since the influence of stratification on the mixing length is taken into account by the buoyancy terms in the transport equations for k and ε" (DELFT HYDRAULICS, 2010, p.227).

In the transport equations is assumed that the production, buoyancy and dissipation of k and ε dominate the process and then the equations are implemented as non-conservative:

$$\frac{\partial k}{\partial t}+\mathrm{u}\frac{\partial k}{\partial x}+\mathrm{v}\frac{\partial k}{\partial y}+\frac{\mathrm{w}}{h+\eta}\frac{\partial k}{\partial \sigma}=\frac{1}{(h+\eta)^2}\frac{\partial}{\partial \sigma}\left(D_k\frac{\partial k}{\partial \sigma}\right)+P_k+B_k-\varepsilon, \qquad \textbf{2-26}$$

$$\frac{\partial \varepsilon}{\partial t}+\mathrm{u}\frac{\partial \varepsilon}{\partial x}+\mathrm{v}\frac{\partial \varepsilon}{\partial y}+\frac{\mathrm{w}}{h+\eta}\frac{\partial \varepsilon}{\partial \sigma}=\frac{1}{(h+\eta)^2}\frac{\partial}{\partial \sigma}\left(D_\varepsilon\frac{\partial \varepsilon}{\partial \sigma}\right)+P_\varepsilon+B_\varepsilon-c_{2\varepsilon}\frac{\varepsilon^2}{k}, \qquad \textbf{2-27}$$

where: D_k and D_ε are the k and ε eddy diffusivities, P_k and P_ε are the production terms, B_k and B_ε are the buoyancy terms and $c_{2\varepsilon}=1.92$ is a constant (DELFT HYDRAULICS, 2010, p.232). Those quantities are defined from:

$$D_k=\frac{\nu_{mol}}{\sigma_{mol}}+\frac{\nu_{3D}}{\sigma}, \qquad \textbf{2-28}$$

$$D_\varepsilon=\frac{\nu_{3D}}{\sigma}, \qquad \textbf{2-29}$$

$$P_k=\nu_{3D}\frac{1}{D^2}\left[\left(\frac{\partial \mathrm{u}}{\partial \sigma}\right)^2+\left(\frac{\partial \mathrm{v}}{\partial \sigma}\right)^2\right], \qquad \textbf{2-30}$$

$$P_\varepsilon=c_{1\varepsilon}\frac{\varepsilon}{k}P_k, \qquad \textbf{2-31}$$

$$B_k=\frac{\nu_{3D}}{\rho\sigma}\frac{g}{H}\frac{\partial \rho}{\partial \sigma}, \qquad \textbf{2-32}$$

$$B_\varepsilon=c_{1\varepsilon}\frac{\varepsilon}{k}(1-c_{3\varepsilon})B_k, \qquad \textbf{2-33}$$

where ν_{mol} is the kinematic (molecular) viscosity, σ_{mol} is the Prandtl-Schmidt number for molecular mixing, $\nu_{3D}=c_\mu {k^2}/{\varepsilon}$ is the part of the eddy viscosity obtained from the turbulence closure model in the vertical direction, and the constants are $c_{1\varepsilon}=1.44$ and $c_{3\varepsilon}=0$ for unstable stratification and $c_{3\varepsilon}=1$ for stable stratification.

The vertical eddy viscosity is calculated from:

$$\nu_\mathrm{v}=c_\mu\frac{k^2}{\varepsilon}, \qquad \textbf{2-34}$$

where $c_\mu=0.11115$ is a constant.

For the two-dimensional modelling, Delft3D has a sub-grid scale model to calculate the horizontal components of the sub-grid eddy viscosity and diffusivity. This turbulence sub-grid scale model will not be discussed in detail as the use of depth-averaged approach is not desirable when sediment transport is considered. When using a two-dimensional approach, important vertical effects like variations of the velocity over the water column, vertical mixing and stratification are neglected.

2.8. Sediment transport and morphological changes

Due to Newton’s third law, the flow boundary layer exerts a shear stress over the bed of the same magnitude and opposite direction as the bottom friction. If this shear stress exceeds the threshold of transport for the type of sediments that compose the bed, sediment movement begins. The threshold of transport depends on the sediment size and shape, yet those relationships are empirical. It has been observed that mud has larger resistance than sand to be put in motion by currents; additionally mud is mostly located in deep ocean while sand is mostly located on coastal regions. Then sand is more likely to be transported and deposited by tsunamis than mud (SUGAWARA et al., 2008).

Once the sediment has been set on motion it remains in constant contact with the bottom as bed load until the turbulence of the flow increases enough to incorporate it completely to the flow. Then, it is transported at the entire water column over longer distances as suspended load. Sugawara et al. (2008) wrote that for tsunamis in near-shore and onshore areas “suspended load may dominate the transport process”.

Sediment transport is the carriage of sediment particles by a flow. Sugawara et al. (2008) also wrote “The quantitative evaluation of the distribution and concentration of the sedimentary particles in a tsunami is certainly a complicated problem, since tsunami run-ups are highly developed turbulent flows, and the physical properties of the sediment carried by them vary from particle to particle”.

Two properties are important in the process: the sediment concentration and its rate of travel (ALLEN, 1992). Both quantities are considered on the three-dimensional mass-balance equation for each suspended sediment fractions:

$$\frac{\partial c^{(b)}}{\partial t} + \frac{\partial\left(\mathrm{u}c^{(b)}\right)}{\partial x} + \frac{\partial\left(\mathrm{v}c^{(b)}\right)}{\partial y} + \frac{\partial\left[\left(\mathrm{w} - \mathrm{w}_s^{(b)}\right)c^{(b)}\right]}{\partial z} - \frac{\partial}{\partial x}\left(\varepsilon_{s,x}^{(b)}\frac{\partial c^{(b)}}{\partial x}\right) - \frac{\partial}{\partial y}\left(\varepsilon_{s,y}^{(b)}\frac{\partial c^{(b)}}{\partial y}\right) - \frac{\partial}{\partial z}\left(\varepsilon_{s,z}^{(b)}\frac{\partial c^{(b)}}{\partial z}\right) = 0 \qquad \textbf{2-35}$$

where $c^{(b)}$ is the mass concentration of sediment fraction (*b*), $\mathrm{w}_s^{(b)}$ is the settling velocity of sediment fraction (*b*) and $\left(\varepsilon_{s,x}^{(b)}, \varepsilon_{s,y}^{(b)}, \varepsilon_{s,z}^{(b)}\right)$ are the eddy diffusivities of sediment fraction (*b)* on the respective direction *x*, *y* and *z* (DELFT HYDRAULICS, 2010). Eq. 2-35 is given in Cartesian coordinates but can be easily converted to σ-coordinates by the chain rule. Several fractions of sediments might be suspended at the same time; if so, each of them should have its own Eq. 2-35.

The eddy diffusivities or vertical sediment mixing coefficients are calculated by the model employing:

$$\varepsilon_s^{(b)} = \beta_{eff}^{(b)} \varepsilon_f \qquad \textbf{2-36}$$

where ε_f is the vertical fluid mixing coefficient and $\beta_{eff}^{(b)}$ is the effective Van Rijn's beta factor of sediment fraction (b). As wind waves are not considered in the modelling

$$\beta_{eff}^{(b)} = 1 + 2\left({\mathrm{w}_s^{(b)}} \big/ {\mathrm{u}_{*,c}} \right) \qquad \textbf{2-37}$$

where $\mathrm{u}_{*,c}$ is the local bed shear stress due to currents and $\mathrm{w}_s^{(b)}$ is the settling velocity of the sediment fraction (b). The vertical fluid mixing coefficient defines the sediment dispersion and is calculated from the eddy viscosity obtained by the turbulence closure model. The value of $\beta_{eff}^{(b)}$ varies in space and time, but it is limited by the model to be between 1 and 1.5 due to the uncertainties remaining in the physical processes involved.

When the flow velocity decreases under a threshold named settling velocity, the sediment settles on the bottom again due to gravity. The free settling velocity is the terminal velocity of a particle when the drag force has the same magnitude of its weight; at that moment the net force is zero and therefore there is no acceleration and the velocity remains constant. As the drag force depends on the size of the sediment particle, so does the free settling velocity:

$$\mathrm{w}_{\mathrm{s},0}^{(\mathrm{b})} = \frac{10\nu_{mol}}{D_S^{(b)}}\left[\sqrt{1 + \frac{0.01[s^{(b)}+1]gD_S^{(b)^3}}{\nu^2}} - 1\right] \qquad \textbf{2-38}$$

for $100\mu m < D_S^{(b)} \leq 1000\mu m$, where $D_S^{(b)}$ is the representative sediment diameter of fraction (b) and $s^{(b)} = {\rho_s^{(b)}} \big/ {\rho_{\mathrm{w}}}$ is the relative density of sediment fraction (b). This derivation of the settling velocity was done for free settling: a single particle on an infinite fluid. In the reality the presence of many sediment particles affect the settling velocity, because there are interactions between them. This effect is called hindered settling. In the formulation employed here, the settling velocity is computed following van Rijn (1993) accounting for the sediment concentration, and then becomes a function of time and position additionally to the physical characteristics that define the free settling velocity:

$$\mathrm{w_s^{(b)}} = \left(1 - \frac{c_s^{total}}{C_{soil}}\right)^5 \mathrm{w}_{s,0}^{(b)} \qquad \textbf{2-39}$$

where c_s^{total} is the sum of the mass concentrations of all the sediment fractions present in the fluid, C_{soil} is the reference density and $\mathrm{w}_{s,0}^{(b)}$ is the free settling velocity for the sediment fraction (b).

Suspended sediments modifies the fluid density. On the modelling this effect “is achieved by adding (per unit volume) the mass of all sediment fractions, and subtracting the mass of the displaced water” (DELFT HYDRAULICS, 2010) in each time step:

$$\rho_{mix} = \rho_{\mathrm{w}} + \sum_{b=1}^{Bsed} c^b \left(1 - \frac{\rho_{\mathrm{w}}}{\rho_{sed}^{(b)}}\right) \qquad \textbf{2-40}$$

where ρ_{mix} is the density of the water-sediment mix at a given salinity and temperature, ρ_{w} is the water density at the same salinity and temperature, Bsed is the total number of sediment fractions present on the modelling and $\rho_{sed}^{(b)}$ is the density of the sediment fraction (b). The change on the fluid density might be important on the calculation as it might lead to stratification which in turn can have an effect on the vertical turbulent mixing.

To solve Eq. 2-35 it is necessary to establish initial and boundary conditions for sediment transport. In the case of tsunami modelling it is assumed that there was no sediment suspended before the tsunami arrived and then an initial condition of zero mass concentration is prescribed. It is also considered that there is no tsunami erosion far from the coast and then the open boundaries are chosen to be far enough from the interest region so no sediment transport is expect through them. However, Delft3D has the option of a Neumann equilibrium boundary condition, applied on the experiments performed here, which imposes a zero concentration gradient through the open boundaries to avoid erosion and deposition along them.

In Delft3D the transport equation (Eq. 2-35) is formulated using a finite-volume approximation and solved using the Cyclic Scheme (STELLING and LEENDERTSE, 1991). The sediment transport formulation employed was from Van Rijn (1993) which differentiates between bed load and suspended load, and the separation between them is located at a height over the bed named reference height. The reference concentration is defined as the sediment concentration at the reference height, and is calculated directly from the sediment transport formula and adjusted to the availability of sediment on the upper layer of the bed (VAN RIJN, 2007):

$$c_a^{(b)} = 0.015\rho_s^{(b)} \frac{D_{50}^{(b)} {T_a^{(b)}}^{1.5}}{a {D_*^{(b)}}^{0.3}}, \qquad \textbf{2-41}$$

where $D_{50}^{(b)}$ is the median sediment diameter for fraction (b), $D_*^{(b)}$ is the non-dimensional particle diameter for fraction (b):

$$D_*^{(b)} = D_{50}^{(b)} \left[\frac{\left(s^{(b)} - 1\right)g}{\nu^2}\right], \qquad \textbf{2-42}$$

and T_a is the non-dimensional bed shear stress:

$$T_a^{(b)} = \frac{\mu_c \tau - \tau_{cr}^{(b)}}{\tau_{cr}^{(b)}}, \qquad \textbf{2-43}$$

where the bed shear stress is calculated using Eq. 2-20, $\tau_{cr}^{(b)}$ is the critical bed shear stress for sediment fraction (b), and the efficiency factor is $\mu_c = {f_c'}\big/{f_c}$ obtained from the gain related and total current related friction factor. The latter is $f_c = C^{-2}$ and the former is related to the sediment passing size. The critical bed shear stress is:

$$\tau_{cr}^{(b)} = \left(\rho_s^{(b)} - \rho_w\right) g D_{50}^{(b)} \theta_{cr}^{(b)}, \qquad \textbf{2-44}$$

where the Critical Shields parameter $\theta_{cr}^{(b)}$ is given by:

$$\theta_{cr}^{(b)} = \begin{cases} 0.24{D_*^{(b)}}^{-1}, & 1 < D_*^{(b)} \leq 4 \\ 0.14{D_*^{(b)}}^{-0.64}, & 4 < D_*^{(b)} \leq 10 \\ 0.04{D_*^{(b)}}^{-0.1}, & 10 < D_*^{(b)} \leq 20 \\ 0.013{D_*^{(b)}}^{0.29}, & 20 < D_*^{(b)} \leq 150 \\ 0.055, & 150 < D_*^{(b)} \end{cases} . \qquad \textbf{2-45}$$

Bed load "is computed separately as it responds almost immediately to changing flow conditions and feels the effects of bed slope" (DELFT HYDRAULICS, 2010, p.346). In Delft3D the bed load transport is calculated at the cell centres using:

$$\left|\mathrm{S}_{\mathrm{b}}^{(\mathrm{b})}\right| = 0.006\rho_s^{(b)}\mathrm{w}_{\mathrm{s}}^{(\mathrm{b})}\mathrm{D}_{50}^{(\mathrm{b})}{M^{(b)}}^{0.5}{M_e^{(b)}}^{0.7} \qquad \textbf{2-46}$$

(VAN RIJN et al., 2004), where $\mathrm{M}^{(\mathrm{b})}$ and $M_e^{(b)}$ are the sediment mobility number and excess sediment mobility number, respectively:

$$M^{(b)} = \frac{\mathrm{v}_r^2}{(s^{(b)}-1)gD_{50}^{(b)}} \qquad \textbf{2-47}$$

$$M_e^{(b)} = \frac{(\mathrm{v}_r - \mathrm{v}_{cr})^2}{(s^{(b)}-1)gD_{50}^{(b)}} \qquad \textbf{2-48}$$

where v_r is the magnitude of an equivalent depth-averaged velocity computed from the velocity in the bottom computational layer assuming a logarithmic velocity profile and v_cr is the critical depth-averaged velocity for the initiation of motion based on the Shields curve. This bed load transport is then converted to the cell faces by an upwind scheme and corrected for bed slope, bed composition and sediment availability (DELFT HYDRAULICS, 2010, p.345). As wind waves were not considered in this work, the bed load transport was calculated only based in currents.

The change in the mass of the bed is calculated on every time step, as result of sediment sink and source terms and transport gradient (DELFT HYDRAULICS, 2010), and then converted to change on bed level. In this way, the coupling between hydrodynamics and morphodynamics is performed in both directions. The following equation calculates the exchange of material between the bed and the flux by means of the bottom boundary condition:

$$-\mathrm{w}_{\mathrm{s}}^{(\mathrm{b})}c_s^{(b)} - \varepsilon_{s,z}^{(b)}\frac{\partial c^{(b)}}{\partial z} = D^{(b)} - E^{(b)}, \qquad at\ z = -h \qquad \textbf{2-49}$$

where $\mathrm{D}^{(\mathrm{b})}$ and $\mathrm{E}^{(\mathrm{b})}$ are the sediment deposition and erosion rates for sediment fraction (b). These rates are calculated on the first layer completely above the reference height, which is known as the reference layer or kmx-layer.

The erosion rate is

$$E^{(b)} = \varepsilon_s^{(b)} \frac{\partial c^{(b)}}{\partial z} \approx \alpha_2^{(b)} \varepsilon_s^{(b)} \left(\frac{c_a^{(b)} - c_{kmx}^{(b)}}{\Delta z} \right) = \frac{\alpha_2^{(b)} \varepsilon_s^{(b)} c_a^{(b)}}{\Delta z} - \frac{\alpha_2^{(b)} \varepsilon_s^{(b)} c_{kmx}^{(b)}}{\Delta z}, \qquad \textbf{2-50}$$

where $c_a^{(b)}$ is the reference concentration of sediment fraction (b), $c_{kmx}^{(b)}$ is the average concentration at the kmx layer, α_2 is a correction factor for sediment concentration differences between the centre and the bottom of the kmx layer, and $\Delta z = z_{kmx} - a$ is the difference in elevation between the kmx layer and the reference level. Then, when the approximation is applied, the erosion rate can be divided in a source term (first term on the right side) and a sink term (second term on the right side) (DELFT HYDRAULICS, 2010, p.343). Delft3D requires establishing the depth of the layer of available sediment on the bed and a threshold value for which the erosion will be corrected in case the sediment layer is thinner than the threshold, to simulate the decrease on the transport capacity.

The deposition rate is

$$D^{(b)} = \mathrm{w}_s^{(b)} c_{kmx,b}^{(b)} \approx \alpha_1^{(b)} c_{kmx}^{(b)} \mathrm{w}_s^{(b)} \qquad \textbf{2-51}$$

where α_1 is a correction factor and $c_{kmx,b}^{(b)}$ is the sediment concentration at the bottom of the kmx layer.

The change on the sediment on the bed caused by the bed load transport is:

$$\Delta_{SED}^{(m,n)} = \frac{\Delta t}{A^{(m,n)}} \left[S_{b,uu}^{(m-1,n)} \Delta y^{(m-1,n)} - S_{b,uu}^{(m,n)} \Delta y^{(m,n)} + S_{b,\mathrm{vv}}^{(m,n-1)} \Delta x^{(m,n-1)} - S_{b,\mathrm{vv}}^{(m,n)} \Delta x^{(m,n)} \right], \qquad \textbf{2-52}$$

where $\Delta_{SED}^{(m,n)}$ is the change on the bottom sediment at location (m,n), Δt is the computational time step, $A^{(m,n)}$ is the area of cell (m,n), $S_{b,uu}^{(m,n)}$ is the computed bed load transport vector in u direction at the u point of the cell (m,n), $\Delta x^{(m,n)}$ is the cell size on the x-direction at point V of the cell, and $\Delta y^{(m,n)}$ is the cell size on the y-direction at point U of the cell. The calculation is repeated for each sediment fraction (DELFT HYDRAULICS, 2010, p.371).

The equations employed on sediment transport are empirical and have been formulated based on measurements of flow velocities, bed shear stresses and sediment concentrations obtained in rivers and in coastal waters caused by wind waves. The values measured in such environments and for the mentioned phenomenon are much smaller than those related to tsunamis. Although their adequacy is still on discussion (APOTSOS et al., 2011b), these are the only equations available so far: it is impossible to measure the sediment transport during tsunami runup (SUGAWARA et al., 2008). Even when sediment transport during a tsunami has been measured offshore, it was impossible to separate the sediment transport due to the tsunami from that caused by wind waves (LACY et al., 2012). The development of tsunami specific sediment transport equations might be possible by means of numerical modelling; but this research field is still adjusting. Nevertheless, the results achieved so far (APOTSOS et al., 2009), (APOTSOS et al., 2011a), (APOTSOS et al., 2011b), (TAKAHASHI et al., 2000) have encouraged the use of the currently available sediment transport equations for the computation of morphological changes due to tsunamis.

2.9. Open boundary conditions for the flow

Delft3D allows the use of the Riemann-invariant boundary condition to minimize false reflections in the open boundary (VERBOOM and SLOB, 1984). The Riemann invariant is calculated from the water level and the flow velocity at the boundary:

$$f_R = u \pm \eta\sqrt{\frac{g}{h}}. \tag{2-53}$$

The sign on Eq. 2-53 depends on the direction of incidence of the wave.

Riemann-invariant boundary condition was employed on all the experiments performed here. If an open boundary had no incoming wave then a zero Riemann invariant was prescribed to allow the wave leaving the domain.

To impose the N-waves of the first and second set of experiments (Chapter 3 and 5) it was employed the flow velocity of linear shallow water waves: $\mathrm{u} = \eta\sqrt{{}^{g}/_{h}}$. Apotsos et al. (2011d) tested this flow velocity against the flow velocity of simple waves $\left(\mathrm{u} = 2\sqrt{g|h+\eta|} - 2\sqrt{gh}\right)$ as input for Riemann invariant, and found that both performed almost identically. In the third set of experiments (Chapter 6) the flow velocity for the Riemann invariant boundary condition of the smallest grid was obtained from the modelling results of the larger grid.

2.10. Initial conditions for the flow

The flow initial conditions are the water surface perturbation (η) and the flow velocity at the initial time of the simulations. As tsunamis are the only phenomena considered in the modelling, a zero flow velocity was prescribed at the beginning of the simulations in all cases.

For the experiment of tsunamis or waves originated outside the domain the initial water surface perturbation is zero over the whole domain, as in the first and second set of experiments (Chapter 4 and 5).

In the third set of experiments (Chapter 6) the co-seismic deformation caused by the earthquake was employed as initial water surface perturbation for the tsunami, assuming that it happened fast enough so the deformation of the sea surface was the same as the deformation of the seabed.

2.11. Grid nesting

The simulation of the tsunami propagation from its source region to distant coastal areas, like the one performed in Chapter 6 requires the nesting of several grids. Delft3D system allows the use of nested grids or domains in two ways: online (or parallel) and offline. Both require that the grids involved have the same type of coordinates, Spherical or Cartesians.

The online nesting is named Domain Decomposition of the Delft3D-FLOW, and requires that all the domains involved have identical setup (DELFT HYDRAULICS, 2010, p.p. 606), the only differences would be the grid, enclosure and depth files, and the number of σ-layers (if needed). Additionally there should be no grid overlap, and the refinement between grids must be done in a 1-to-N ratio, being N an integer number and equidistant refinement is recommended in horizontal directions (DELFT HYDRAULICS, 2010, p.p. 607-608).

The offline nesting is named Delft-NESTHD, and requires the hydrodynamic boundary conditions of the smaller grid to be water level or normal velocity type (DELFT HYDRAULICS, 2010, p.p. 641). In this type of nesting the bigger domain is simulated first and its results are used as boundary condition for the smaller domain.

The online or parallel nesting has more physical meaning because what happens in the small domain also affects what happens in the big one, and in this nesting the simulations in both domains are performed simultaneously. Nevertheless it requires having identical setup in all the domains, then if morphodynamics is simulated in the small domain this type of nesting will require to do it in all the domains. The simulation of morphodynamics in all the nested domains would increment the simulation time unnecessarily and without physical meaning, because the interaction of the tsunami with the bottom in deep water is negligible.

Therefore, in the experiment described in Chapter 6 online nesting was employed for all the grids where only hydrodynamic was calculated. And finally offline nesting was used for the last grid where morphodynamics was also calculated. In the experiment described in Chapter 3 offline nesting was employed as the model system was already defined in this way and the grids did not fulfil the online nesting requirements.

2.12. Model validation

As said on Section 1.3, after the 2004 Indian Ocean tsunami there was an increasing interest on tsunami preparedness all over the world. This in turn led to the elaboration of tsunami mitigation plans, in many cases based on results from tsunami numerical simulations. The need for standards on tsunami numerical models raised to avoid those mitigation plans to be based on erroneous information. Those standards were put together on the official guide for validation and verification of tsunami numerical models of the National Oceanographic and Atmospheric Agency of the United States of America (NOAA) (SYNOLAKIS et al., 2007). These analytical, laboratory, and field benchmarks were later extended for other countries through the Intergovernmental Oceanographic Commission of UNESCO (SYNOLAKIS et al., 2008). Delft3D model was validated for tsunami modelling through seven of the analytical and laboratory benchmarks proposed on Synolakis et al. (2007) and (2008), and through field observations of the 2004 Indian Ocean tsunami, all by Apotsos et al. (2011a).

The mentioned criteria and benchmark solutions refer only to the modelling of tsunami water levels and there are no benchmarks on tsunami flow velocity and neither on tsunami sediment transport and morphological changes. This is mainly because many research and measurements have been done on tsunami water levels but very few on tsunami current velocities and sediment transport. Also, there are only few records of tsunami flow velocities like Bricker et al. (2007), Lynett et al. (2012), Lacy et al. (2012), and Fritz et al. (2006), (2012). To the author’s knowledge there is only one set of direct measurements of sediment transport during a tsunami, and correspond to a distant tsunami (LACY et al., 2012).

Nonetheless, the lack of criteria and benchmark on the modelling of tsunami currents and sediment transport might change in the near future. A workshop on the modelling of tsunami currents was held on February 2015 at the United States of America, for which five different benchmarking datasets were presented. To the date of this dissertation was finished, there was still not a document available resulting from the workshop. However, it was “anticipated that modelers will have a better awareness of their ability to accurately capture the physics of tsunami currents, and therefore a better understanding of how to use these simulation tools for hazard assessment and mitigation efforts” (USC, 2015).

3. State of the art

3.1. Tsunamis at the North Sea

To the authors' knowledge, two modelling studies on tsunamis in the North Sea have been performed to date: one by Borck et al. (2007) and the other one by Lehfeldt et al. (2007). Both studies obtained modelled tsunami heights of less than 2m and therefore concluded that the tsunami risk is not high for the German Bight because of the shallow depths of the North Sea and because of the protection provided by Norway and the British Islands. Nevertheless, Newig and Kelletat (2011) put together several reports along the North Sea basin to demonstrate that there was a tsunami on 5 June 1858, which caused run-ups of up to 4m in Germany, specifically in Sylt, Helgoland and Wangerooge. Tsunami heights between 1.2 and 6m were reported also in the United Kingdom, France, the Netherlands and Denmark. There were no casualties reported because the summer season had not yet started and tourism was scarce at that time. Still, several people, mostly in fishing communities, were reported to have barely escaped the onslaught of the tsunami (NEWIG and KELLETAT, 2011).

The biggest weakness of both studies lay on the tsunami source. Borck et al. (2007) used as input for their tsunami model "three successive positive single waves" generated by a sine-square function. The use of three positive solitary waves together has no physical meaning, as they are not a good representation of the leading wave of tsunamis. Lehfeldt et al. (2007) used a square hyperbolic secant solitary wave as input and imposed it perpendicularly at the open boundaries. Even when solitary waves are accepted as a representation of the leading tsunami wave, better results are obtained using N-waves to represent tsunami hydrodynamics because of their bipolarity (TADEPALLI and SYNOLAKIS, 1996). Particularly, the reports of the 1858 tsunami in the English Channel draw attention to a withdrawal of the sea followed by an inundation (NEWIG and KELLETAT, 2011), following leading depression N-waves.

3.2. N-waves

Tadepalli and Synolakis (1996) were the first employing N-waves as a parameterization of the leading wave of tsunamis. The waves they proposed and other types of N-waves were utilized on analytic and numerical solutions of tsunami problems, such as Carrier et al. (2003), Pritchard and Dickinson (2008), and Madsen and Schäffer (2010). N-waves proved to be a good approximation for calculating tsunami runup and inundation. They are usually used on numerical or physical experiments on a channel or a rectangular basin. They are employed also on analytical benchmarks for the validation and verification of tsunami numerical models (SYNOLAKIS et al., 2007), (SYNOLAKIS et al., 2008).

3.3. Tsunami morphodynamics

Tsunami sediment deposits have proved the occurrence of historical tsunamis (DAWSON and STEWART, 2007) and have assisted in the determination of some tsunami characteristics both on historical and recent tsunamis (DAWSON, 1999), (BOURGEOIS, 2009). However, most of the existing literature related with tsunami sediment transport and morphological changes is descriptive: very little modelling has been done in this field. For example, many researchers surveyed old sediment deposits to confirm the occurrence of tsunamis (DAWSON et al., 1988), (CLAGUE et al., 2000), (GOFF et al., 2000), (JAFFE and GELFENBAUM, 2007). In these cases tsunami heights were estimated based on the extent of tsunami deposits, as their location is considered an indicator of the minimum possible tsunami inundation limit (DAWSON, 1996). However, the extension of inland sediment deposits in proportion to the inundation distance, varies for every tsunami at every location (MARTIN et al., 2008), being in some cases only half of it (GOTO et al., 2011).

In the decade of 1990’s there were several publications in Japanese on numerical modelling of tsunami morphodynamics. The first traceable publication in English was from Takahashi et al. (2000) in which the authors proposed a two-dimensional model assuming there was no equilibrium on the sediment concentration profile. Many models based on river flows assumed an equilibrium profile of the sediment concentration, which is obviously not the case of tsunami flows. Takahashi et al. (2000) proposed an exchange rate between the suspended and the bed load layers, neglecting the critical Shields parameter in this exchange rate as long as in the bed load transport rate. The authors simulated the erosion and deposition caused by the 1960 Chile tsunami in Kese-numa port in Japan. They analysed the performance of the model in terms of the ratio of deposition volume to erosion volume which the model overestimated. In contrast, the model underestimated the maximum erosion and deposition, and the total volume of sand eroded and deposited.

Since then, modelling has been performed mostly with two-dimensional models. In some cases the model was two-dimensional-horizontal or depth-averaged (NISHIHATA et al., 2006), (HUNTINGTON et al., 2007), (GELFENBAUM et al., 2007), (APOTSOS et al., 2011c), (LI et al., 2012), (ONTOWIRJO et al., 2013). And in some cases the model was two-dimensional-vertical, 2DV, considering only one horizontal dimension and variations over the water column (APOTSOS et al., 2009), (APOTSOS et al., 2011a), (APOTSOS et al., 2011b). Some three-dimensional modelling has been performed as well (NAKAMURA et al., 2009), (KIHARA and MATSUYAMA, 2010), (KIHARA et al., 2012).

As sediment transport is a problem involving three dimensions, the employment of only two of them implies simplifying assumptions that have an impact on the results. Two-dimensional horizontal models use a depth-averaged approach which implies poor resolution of the near-bed processes and secondary flows when present (KIHARA et al., 2012). On the other hand, two-dimensional vertical models assume normal incidence of the tsunami and consider only cross-shore flow velocity and transport, ignoring any possible influence of the alongshore components.

Three-dimensional modelling, considering alongshore and vertical variations, requires larger computational effort and it has only become more common in the past few years. Nakamura et al. (2009) modelled three-dimensionally the scour caused by a solitary wave around a fixed structure in laboratory scale. They employed three different sediment transport formulations departing from Takahashi et al. (2000). In the first one they modified the original formulation by incorporating the critical Shields parameter on the exchange rate and the bed load transport rate. In the second one they used the modified Shields parameter to consider “infiltration/exfiltration flow velocity” on the bed. In the third one they included also the effective stress on the surface layer of the bed. In the last two formulations they employed some calibration parameters which according to them should be further studied. The last formulation gave the best results, although overestimated the scour depth around the structure, and underestimated the erosion depth behind the seawall. The coupling between the hydrodynamics and the morphodynamics on their model was done only in one direction: there was no update of the bathymetry during the simulation.

Kihara and Matsuyama (2010) performed three-dimensional modelling of the morphological changes caused by the 2004 Indian Ocean tsunami in Kirinda port, Sri Lanka on the only three-dimensional modelling study in real scale done so far. Their model predicted well the erosion between the main breakwater and the old secondary breakwater. Nevertheless, a scour up to 6m at the head of the main breakwater and the sand control wall was predicted when the tsunami actually created deposits of up to 6m there. In another research, Kihara et al. (2012)

did three-dimensional modelling of the morphological changes caused by a solitary wave in a laboratory-scale harbour. Their model reproduced well the pattern of those changes although underestimated the scour depth at the head of the breakwaters and the deposition height at the centre of the harbour. The model on the last two papers employed the sediment transport formulation of Van Rijn (1984a), (1984b) with the Mellor-Yamada closure turbulence model, which damping function has shown to produce stepwise profiles of eddy viscosity (DELEERSNIJDER and LUYTEN, 1994).

Apotsos et al. (2009), (2011b) established the importance of several factors such as sediment size, composition, and distribution, and bed roughness, on the location and magnitude of the final tsunami driven morphological changes, employing Delft3D model. According to their results, the modelling of tsunami morphodynamics requires a larger amount of data than the modelling of only the tsunami propagation and inundation. Some of these data required are not easy to obtain, for example the bed roughness coefficient. As the value of the Manning's coefficient determines the amount of energy dissipated by friction, it influences the calculated values of flow velocity (GAYER et al., 2010) and consequently the erosion and deposition as well. Nevertheless, typically a uniform value is used in tsunami simulations, as in most cases there is very little information available to do it any other way.

Also, the difficulties getting morphological data right before and right after a tsunami contribute to the reduced number of studies modelling tsunami morphodynamics. Tides, storms and other regular phenomena are constantly modifying the coasts and can modify the morphological changes caused by a tsunami. Therefore, it would be necessary to be taking coastal morphology data continuously in order to have accurate pre-tsunami and post-tsunami data. Usually it is almost impossible to travel to places affected by a tsunami right after it happened, not to mention that the continuous coastal monitoring is expensive and then performed only under certain circumstances.

4. Several tsunami scenarios at the North Sea and their consequences at the German Bight

The results of this experiment were published with the same title at Science of Tsunami Hazards, V. 32, N. 1, 2013.

The work described in this Chapter involved ten experiments in order to explore the tsunami risk in terms of run-up for the German Bight under a wider and more realistic approach. As it is well known, earthquakes are the most common source of tsunamis in the world and earthquake-generated tsunamis differ from those generated by landslides, both in amplitude and frequency. Consequently, it was considered one case of a landslide-generated tsunami with normal incidence and seven cases of earthquake-generated tsunamis with various directions of incidence. In all these cases, tides were not considered in the modelling. To explore the role of tides on tsunami heights, were performed two more experiments which included tides in the calculations.

4.1. Model domain and setup

Specifically for this study, it was modified an existing model system on Delft3D which covers the entire North Sea. The model system consists of four, two-dimensional, nested models: a) the Continental Shelf Model (CSM) from Verboom et al. (1992), b) the North Sea Model (NSM) from Bruss et al. (2010), c) the German Bight (GBM), and d) the Dirthmarschen Bight (DBM) models from Hartsuiker (1997). For the present study, only two models of the system were employed: the NSM and the GBM. The first model covers only the North Sea and it is not capable of computing inundation on dry land. In this model the input waves can be imposed in both the western and the northern open boundaries. The second model, the GBM, covers the German coasts and it is capable of simulating inundation on dry land. The nesting boundaries between the NSM and the GBM are drawn with thick black lines in Figure 4-1. The resolution of the original NSM varies between 7079.62m and 9349.68m, and it was refined to minimize numerical dispersion on tsunami propagation. The refined NSM (refNSM) has a resolution between 2359.87m and 3116.58m.

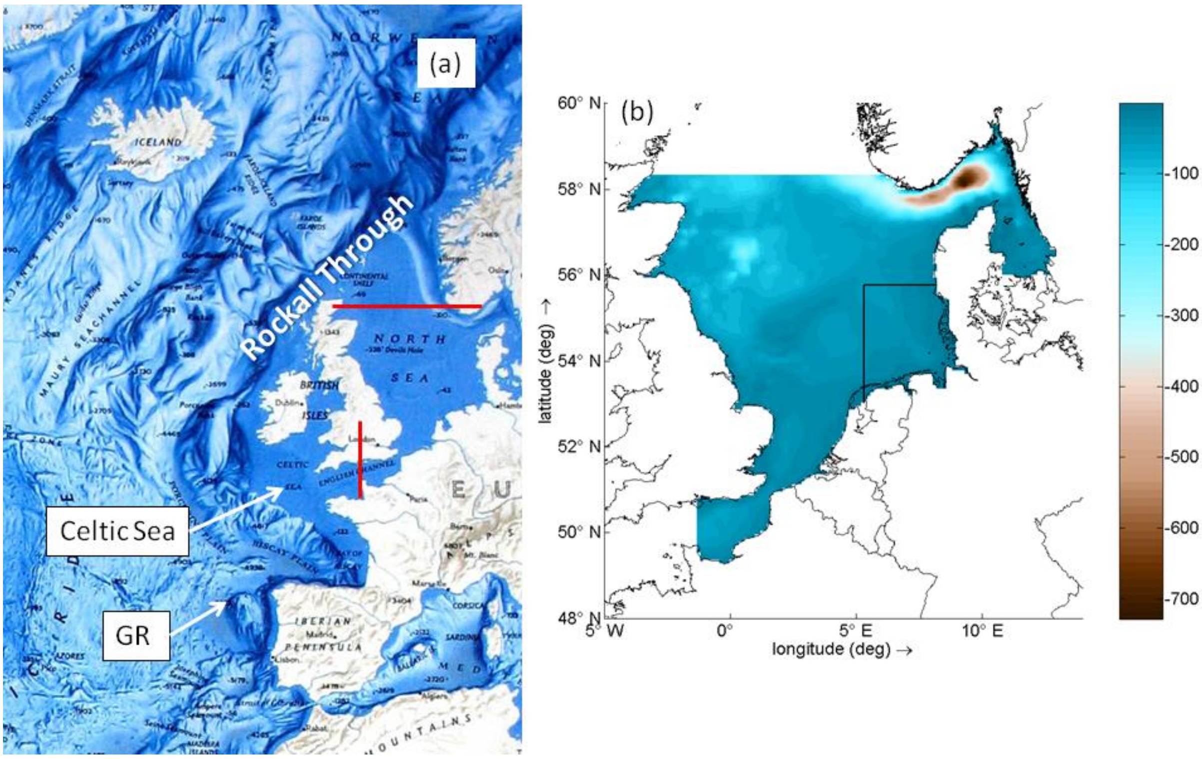

Figure 4-1. (a) Bathymetry of the North Atlantic Ocean. The Galician Rise (GR), the Celtic Sea and the Rockall Through are pointed. Also the open boundaries of the North Sea model are plotted. (b) Extent and bathymetry of the model system. The thick black lines show the boundaries between the German Bight Model (GBM) and the North Sea Model (NSM). The colour scale is in meters of depth.

The nesting between CSM and GBM was validated by Mayerle et al. (2005). Later Bruss et al. (2010) split the CSM and defined the NSM. As the NSM consists on a section of the CSM and has the same resolution, the nesting between the NSM and the GBM is the same as between the CSM and the GBM. Nevertheless, as the North Sea grid was refined for tsunami propagation purposes, it became necessary to validate the nesting between the refNSM and the GBM. For this purpose, were performed simulations of three large storms at the North Sea, which occurred in 1967, 1976 and 1999 with both the original and refined North Sea models. Additionally, the mild weather conditions from April 2008 were simulated to include more general scenarios. To test the nesting of the refNSM with the GBM were compared its results with results from the NSM nested to the GBM, as this original nesting has been extensively validated with field data (MAYERLE et al., 2005), (BRUSS et al., 2010).

For all validation cases, air pressure and wind fields were imposed in both North Sea models and the results were used as input, together with air pressure and wind fields, for the GBM. The percentage difference between the maximum water heights calculated by both models at the German Bight was smaller than 3% for the whole domain in all cases, indicating that the differences between results from both model systems are negligible, and that the refNSM can be nested to the GBM using the same procedure as for the original model system.

4.2. Storegga-like tsunami

Harbitz (1992) modelled the tsunamis caused by the first and second Storegga slides in the Norwegian Sea 8000 years ago. His resultant time series of water level for the second slide shows a leading depression N-wave with maximum amplitudes of about 2.5m offshore Aberdeen, Scotland (his station 8). The time between the maximum depression and maximum elevation is about 96min. To reproduce such a wave was used the landslide N-wave by Carrier et al. (2003):

$$\eta(t) = a_1 e^{-k1\cdot(t-t1)^2} - a_2 e^{-k2\cdot(t-t2)^2}, \qquad \textbf{4-1}$$

where the following values were assigned: a_1=2.35m, a_2=2.61m, k1=0.00125min^{-2}, k2=0.001min^{-2}, t1=471min and t2=381min. The resulting wave is plotted with a solid line in Figure 4-2. This wave matches Harbitz (1992) modelling, drawn as a dashed line in the same figure. This N-wave defined the boundary condition for a tsunami generated by a landslide, imposed normal to the northern boundary of the refNSM. No wave was imposed at the western boundary.

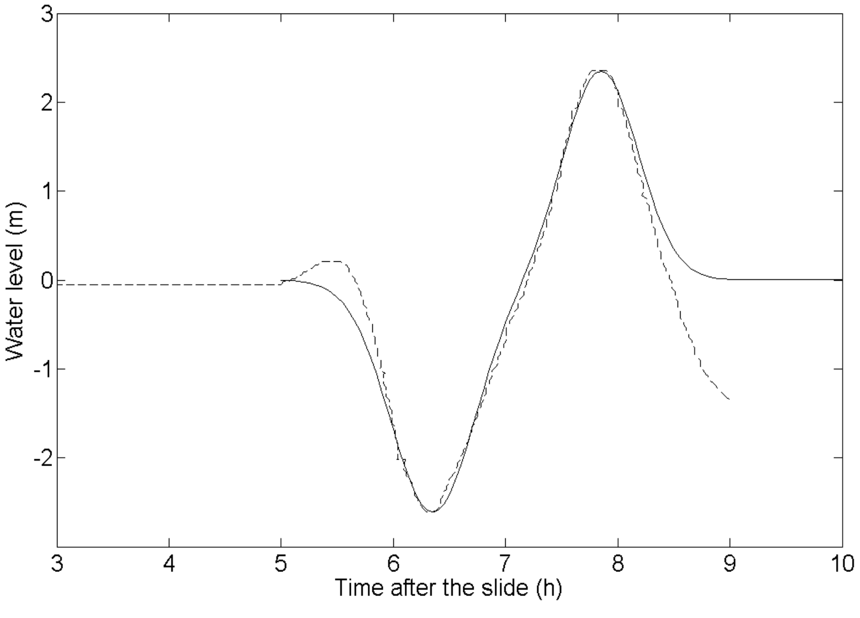

Figure 4-2. Water level of the N-wave imposed as boundary condition (solid line) for the Storegga-like experiment. The results from Harbitz (1992) for the second Storegga slide are shown with a dashed line.

The bathymetry used in the model during the simulations was the present bathymetry. The mean sea level nowadays is not the same as 8000 years ago, and neither is the bathymetry.

Therefore, the goal of this experiment was not to obtain accurate calculations of the historical tsunami run-up but only the consequences for the German Bight if the same tsunami would happen today. As the North Sea Model is not capable to calculate the inundation of dry land, the maximum tsunami heights were computed for the offshore area. However, because of the shoaling effect, the corresponding run-ups should be expected to be larger.

Maximum water levels of more than 5m over the mean sea level were obtained at Inverness and Edinburgh (Firth of Forth), Scotland. These results match those of Smith et al. (2004) who concluded that the run-up of the second Storegga tsunami in inlets at Scotland mainland, probably exceeded 5m over the local mean high water mark of spring tides at that time, while it was probably less along the open coast. Figure 4-3, left side, illustrates the computed maximum tsunami heights along the entire North Sea basin, roughly confirming these estimates.

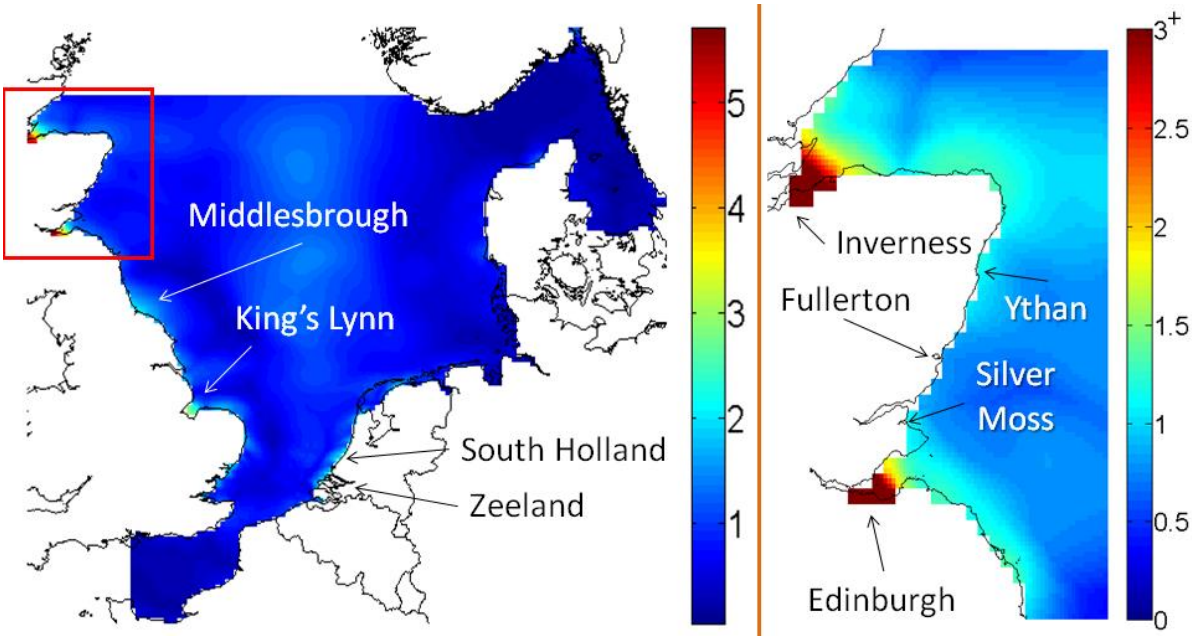

Figure 4-3. Left side: Maximum tsunami heights in meters at the whole North Sea basin for the Storegga-like tsunami, the red rectangle shows the detailed area at the right side where deposits from Storegga tsunami have been identified. At the right side the colour scale is saturated to depict more details.

At the right hand side of Figure 4-3 the maximum tsunami heights are shown along the British coasts where tsunami deposits from Storegga event have been identified. At the open coast site of Waterside (mouth of the river Ythan), maximum offshore heights of 1-1.5m were obtained. Here the maximum height of the sediment deposits is also about 1-1.5m (SMITH et al., 2004). According to Dawson (1999), the height of sediment deposits is lower than the maximum tsunami run-up and considering that run-up should be larger than offshore tsunami heights, the results obtained here were satisfactory in this point. In small inlets the model results seemed to underestimate the tsunami heights. The tsunami deposits suggest a minimum run-up of about 4m in Fullerton (SMITH et al., 2004) and the model reproduces about 1m of maximum offshore tsunami height. At Silver Moss, the tsunami deposits point to a minimum tsunami run-up of about 2m (SMITH et al., 2004) and the model calculated about 1.3m of maximum offshore tsunami height. Together with the lack of correct bathymetry, there is another reason for these differences. Specifically, the refNSM did not include these inlets completely because of its resolution. Also, the refNSM did not consider inundation of dry land; therefore the interaction of the tsunami with the coast is not well solved. At small inlets this interaction determines greatly the tsunami heights. Smith et al. (2004) postulated that the Storegga tsunami also impacted the U.K. shorelines south of where the tsunami deposits were found. The model system predicted offshore tsunami heights above 2m in places like Middlesbrough and King’s Lynn (Figure 4-3 left side). Maximum offshore tsunami heights of over 2m were also obtained in the south coast of the Netherlands, offshore South Holland and Zeeland, although no sediment deposits have been found in these places.

Figure 4-4 illustrates the simulated maximum tsunami heights in the whole German Bight domain for a Storegga-like tsunami. The highest values of almost 2m were obtained for the Western Frisian Islands, specifically at Schiermonnikoog and Ameland, and smaller values of about 1m were obtained for the Northern Frisian Islands, particularly for Sylt.

Figure 4-5 shows water level time series for the six German stations in the regions of higher tsunami heights. Among these stations, the highest water level of almost 1.0m was computed in Westerland, Sylt Island. However, all the time series depicted in Figure 4-5 have a leading depression shape, which usually implies larger onshore velocities (PRITCHARD and DICKINSON, 2008), that can cause greater damage.

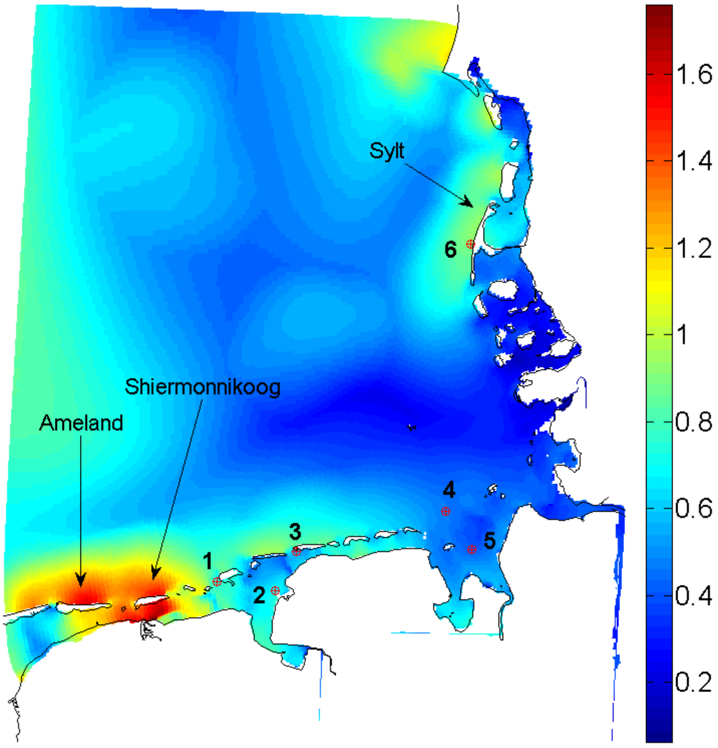

Figure 4-4. Simulated maximum tsunami heights in meters in the German Bight Model for the Storegga-like tsunami. The red crossed circles show the localization of the German stations where the highest tsunami heights were obtained: 1. Borkum, 2. Leybuch, 3. Norderney, 4. Alte Weser, 5. Dwarsgat and 6. Westerland.

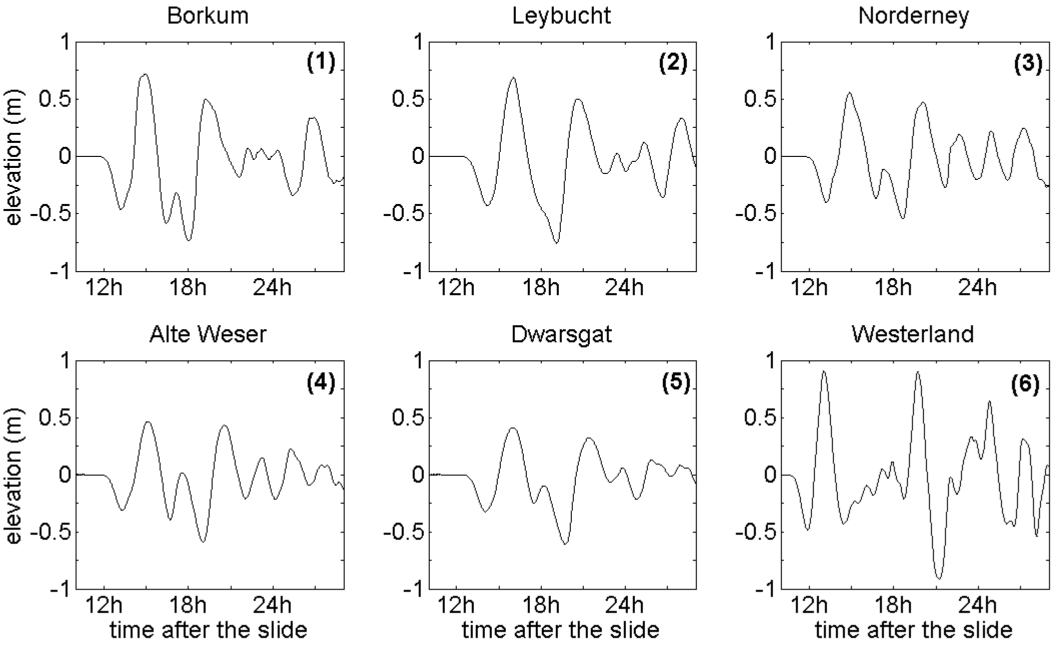

Figure 4-5. Simulated time series of tsunami heights at six stations on the German coast for the Storegga-like tsunami. The localization of the stations is shown in Figure 4-4. The time is given in hours after the event and in all plots water elevation is given in meters over the mean sea level.

4.3. Earthquake-generated tsunamis

The hazard for earthquake-generated tsunamis was evaluated in separate experiments, using forcing functions different than the employed for a landslide-generated tsunami. First, was considered the case of the wave entering only from the western boundary. Additionally, were considered six different directions of incidence for the wave at the northern boundary, to explore the effect of the incidence direction on the focusing of the tsunami energy and the many possible sources for earthquake-generated tsunamis. Two of the incidence directions that were used corresponded to the historical 1755 Lisbon and the 1929 Grand Banks tsunamis. Both tsunamis were generated by earthquakes, however in the case of Grand Banks the earthquake was followed by a submarine landslide.

For all the cases considered in this section, were used symmetric leading depression N-waves as input, similar to the Tadepalli and Synolakis (1996) formulation:

$$\eta(t) = \frac{3\sqrt{3}}{2} H \cdot \operatorname{sech}^2[\gamma(t - t_0)] \cdot \tanh[\gamma(t - t_0)] \qquad \textbf{4-2}$$

where γ and t_0 are constants and H is the maximum wave height. For the tsunamis referred above, no data is available on the height or the width of the incoming waves. Nevertheless, for the 1858 event, the water was reported to recede and then come back in 5-7min, in Bolognesur-Mer and in Le Havre, at the English Channel. Consequently, were chosen t_0=20min and γ=0.2087min^{-1} to have 6min between the depression and the peak of the N-wave. Although N-waves are non-periodic waves, Synolakis et al. (2008) define an equivalent wavelength as the distance between the points where the wave height is 1% of its maximum value at the beginning and at the end of the N-wave. Using this definition, the equivalent period of the wave was 33.2min, typical of earthquake-generated tsunamis. A unitary height (H=1m) was used for the incoming waves because the goal of this section was to identify the vulnerable regions through wave height amplification.

To evaluate the impact of the western wave, the N-wave was imposed only at the western boundary of the refNSM (Figure 4-1b). By comparing wave heights before and after crossing the Dover Strait, the western wave was highly attenuated afterwards. The wave just before and just after crossing the strait are shown in Figure 4-6, at points with similar depths of about 36m. The maximum heights after crossing the strait were strongly reduced. With an incoming wave of unitary height at the mouth of the English Channel, the maximum wave height after the Dover strait was about 10cm. This strong damping implies that there should be almost no interference between a wave entering the North Sea through the west and a wave entering the North Sea through the north.

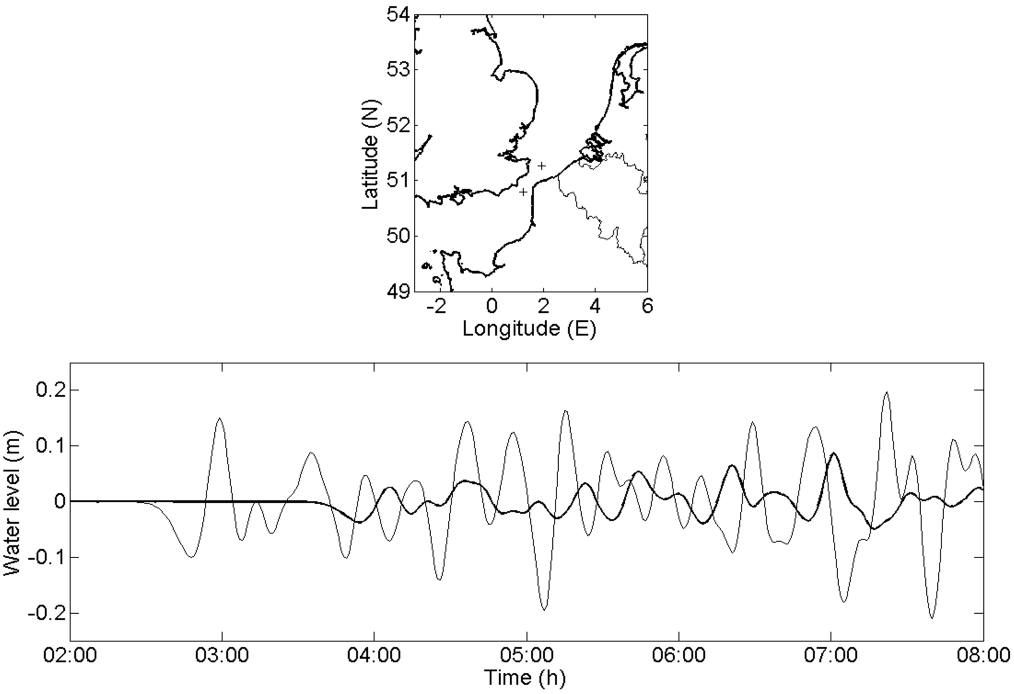

Figure 4-6. Bottom: Comparison of the western wave just before (thin line) and just after (bold line) crossing the Dover strait. Top: Location of the points where the wave was calculated. Both points have depths of around 36m.

To assess the influence of the direction of incidence of the northern wave, were considered two scenarios of earthquake-generated tsunamis based on the NOAA travel time maps of the 1755 Lisbon and 1929 Grand Banks events plotted in Figure 4-7 (NGDC/WDC, 2011). Other authors propose different locations for the 1755 Lisbon earthquake, as usually happens for large earthquakes. In this case in particular, there were no seismograms recorded that contributed to locate the event. As unitary heights were employed, these two historical tsunami scenarios differed only in the incidence direction of the wave through the northern boundary. This difference can be seen in Figure 4-7; the Lisbon tsunami originally came from the south and travelled around Ireland before entering the northern North Sea. The Grand Banks tsunami, on the other hand, came straight from the west, crossing the North Atlantic Ocean before entering the North Sea.

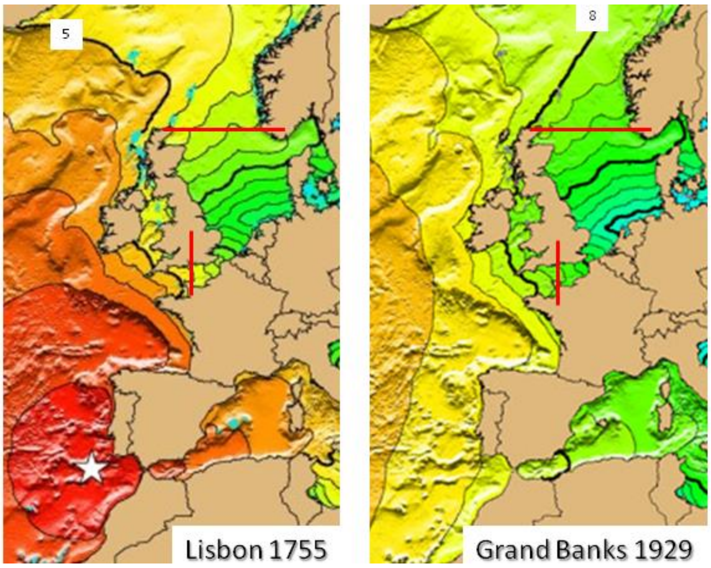

Figure 4-7. Travel time maps for two historical events arriving to the North Sea taken from the National Geophysical Data Center Tsunami Travel Time Maps website (NGDC, 2012). Time contours are plotted every hour and thick black lines are plotted every five hours (left) and every four hours (right). The numbers represent hours after each earthquake. The red thick lines show the approximate boundaries of the refNSM. The plots contain no information on the tsunami heights, only on its travel times.

As the depth of water along the north open boundary of the refNSM is not uniform, the incidence angle is not the same along this boundary (see time contours at Figure 4-7) and it is not possible to refer to a wave incidence angle for the various cases. Instead, the direction of incidence of the tsunami was given by means of the difference of arrival times between Wick in Scotland and Rekefjord in Norwegian shores, hereafter referred to as the time of entrance (Te). If a wave enters normally to the open boundary then the elapsed time Te is zero because it reaches Scotland and Norwegian shores at the same time. Following Figure 4-7, the time of entrance was Te=183min (=3h3min) for the Lisbon-like scenario (case d), and Te=122min (=2h2min) for the Grand Banks-like scenario (case c). Additionally to these two historical tsunamis, four complementary incidence directions were considered: normal incidence (case a), and entrance times of 61, 244 and 305min, cases (b), (e) and (f) respectively. The height of the incoming wave was set to one, in order to present the results in terms of wave amplification rather than in terms of absolute wave height. For simplicity reasons no waves were imposed at the English Channel on these cases.

It was found that the incidence direction determined the places where the energy was concentrated. At the North Sea, the higher the time of entrance, the further east the focusing of the wave energy (Figure 4-8). For all the cases, a certain amount of energy was focused always on the Frisian Islands and North Sunderland in England, although the proportion depended highly on the incidence direction. Also, for all the cases studied in this section, the tsunami heights west of the Dover Straits were negligible.

For the Grand Banks-like tsunami (case c), most of the energy was focused on the East and West Frisian Islands and less on the Durham shores, in England (Figure 4-8c). For this tsunami, there were no reports of arrival at the North Sea at all. It is quite possible that the tsunami was significantly damped after crossing the Atlantic Ocean. For the Lisbon-like tsunami (case d), most of the energy was focused on the East Frisian Islands in Germany (Figure 4-8d). Little energy was focused to the West and North Frisian Islands in the Netherlands, Germany and Denmark and even less to the Durham shores in England. The Global Historical Tsunami Database (NGDC/WDC, 2011) reported the arrival of the Lisbon tsunami at several locations along the east coast of Great Britain, including Firth of Forth in Scotland, Durham and Kingston upon Hull in England. Damaged boats and broken moorings were reported in Friesland, the Netherlands. There are no reports of the tsunami arrival to Germany. Considering the date, the lack of reports might be also due to scarce coastal population or poor record preservation.

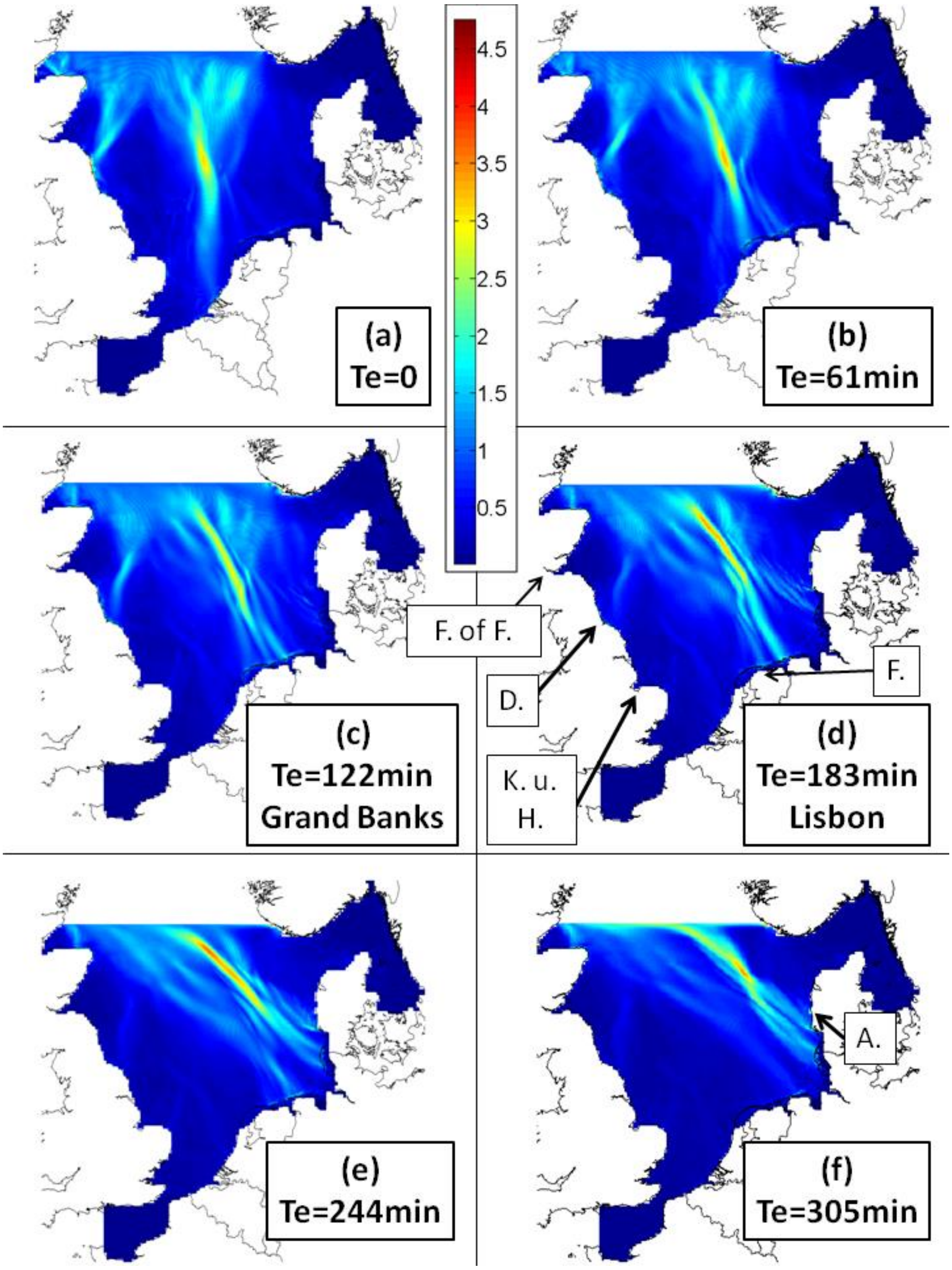

Figure 4-8. Maximum tsunami amplification factor for different directions of incidence of a unitary N-wave following Tadepalli and Synolakis (1996). Case (a) corresponds to perpendicular incidence. The others have oblique incidence with (b) 61min, (c) 122min (Grand Banks like), (d) 183min (Lisbon like), (e) 244min and (f) 305min time to complete the entrance through the northern boundary. Some geographical places are shown in subfigure (d): Firth of Forth (F. of F.) in Scotland, Durham (D.) and Kingston upon Hull (K. u. H.) in England, and Friesland (F.) in The Netherlands. In subfigure (f) Årgab in Denmark is pointed out.

At the GBM, the case of completely normal incidence, case (a), presented wave heights of less than one meter, meaning no amplification of the original wave that entered at the North Sea. Case (b) with almost normal incidence, presented the lowest amplification of wave height for the GBM, of less than two. The Lisbon-like scenario (case d) presented the highest amplification among all cases, of more than three times at the north shores of Borkum and Juist Islands. The Borkum station is facing the mud flat behind the island and the water heights computed there were of less than 2m (Figure 4-10), corresponding to less than twofold amplification. The Westerland station, at the western shore of Sylt Island, registered the highest heights for case (e), which had more tangential incidence than the Lisbon-like case, of almost 2m as shown in Figure 4-10e.

The seaside of the Frisian Islands presented the highest water levels in all cases (Figure 4-9), yet the mudflats between the Frisian Islands and the mainland mitigated the impact of the tsunami at continental shores. This mitigation did not happen for the Storegga-like tsunami of Section 4.2 (Figure 4-4), due to the waveform. The four cases of more normal incidence (cases a, b, c, and d) presented pronounced focusing of energy to the East Frisian Islands, and the two cases of more tangential incidence (cases e and f) presented more focusing of energy to the North Frisian Islands. The arrival time at each station increased with the incidence direction (Figure 4-10), the arrival time for the most tangential case (case f) was between 3 and 4 hours higher than for the normal incidence case (case f).

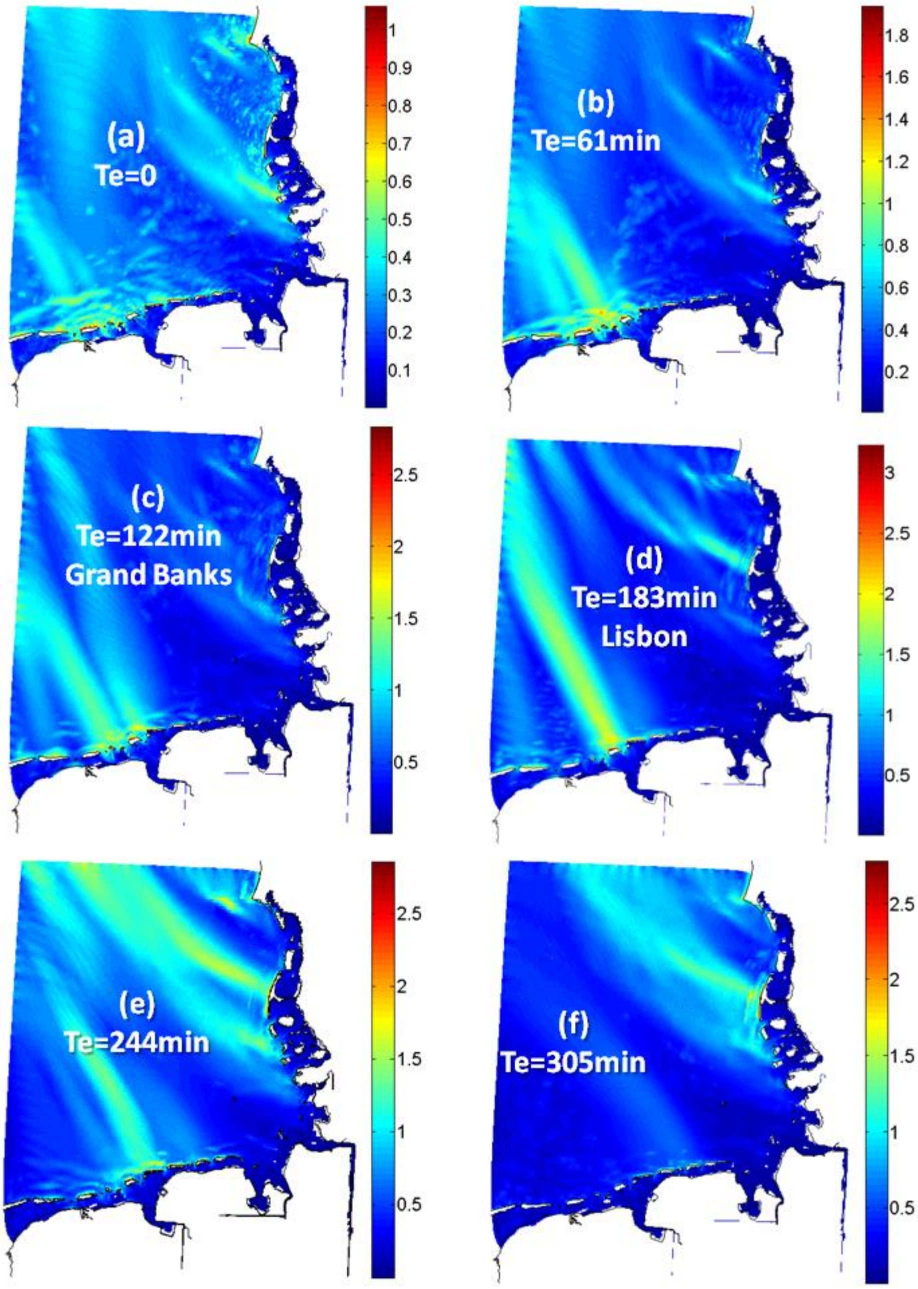

Figure 4-9. Maximum tsunami heights at the German Bight domain in meters for the various directions of incidence at the refined North Sea Model plotted in Figure 4-8. Case (a) corresponds to normal incidence. The others have oblique incidence with (b) 61min, (c) 122min (Grand Banks like), (d) 183min (Lisbon like), (e) 244min and (f) 305min time to complete the entrance through the northern boundary of the refined North Sea Model.

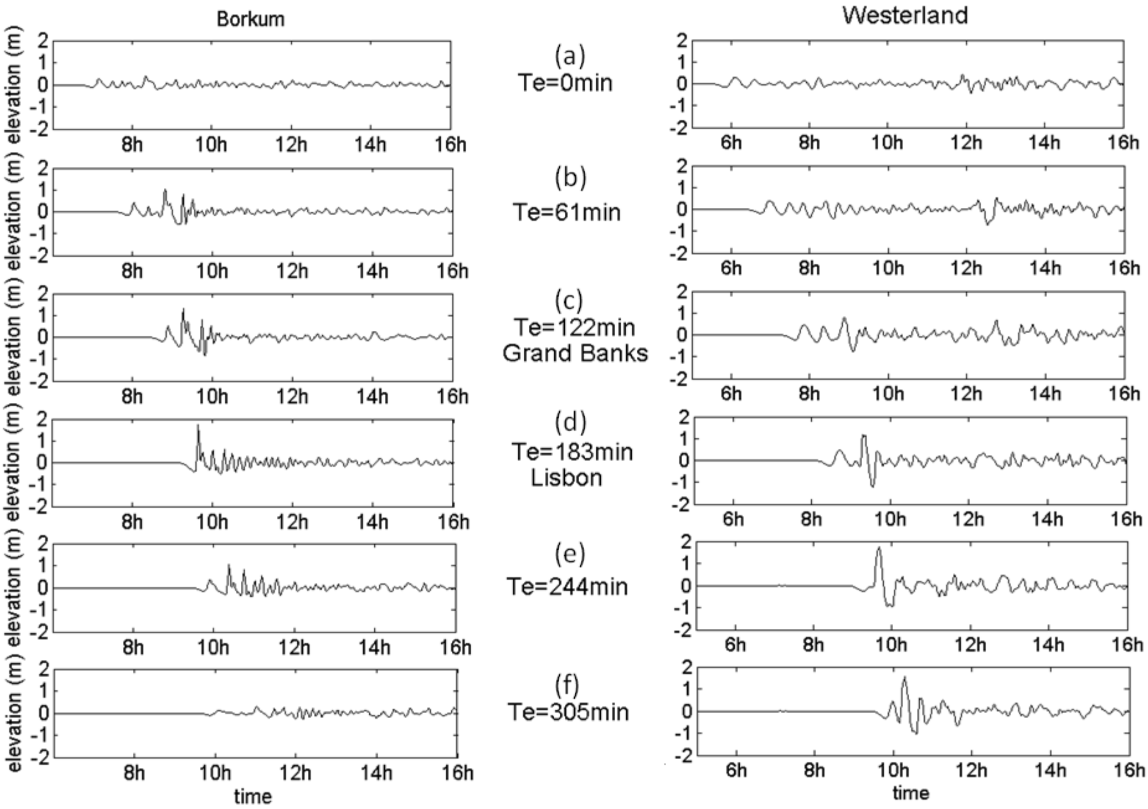

Figure 4-10. Time series of water height in meters for two stations at the Eastern (left) and Northern (right) Frisian Islands for the six incidence directions through the northern boundary of the refNSM.

4.4. The 1858 North Sea tsunami

In 1858 a tsunami arrived to the North Sea from an unknown source. The highest water heights were reported at Wangerooge, East Frisian Islands (between 3.3 to 4m) and Westerland, Sylt Island (3.5 to 4m) in Germany, and at Blåvandshuk (4.5 to 5m) and Årgab (about 6m) in Denmark (NEWIG and KELLETAT, 2011). There were a large number of reports of this tsunami along the English Channel, some of them of about 2.5m height. Yet the tsunami reports in Belgium and in the south of the Netherlands mention only about 1.25m height (NEWIG, 2012).

Newig and Kelletat (2011) conclude that the source of this tsunami was not in the English Channel itself but south of its entrance. They infer that the large tsunami run-ups in Germany and Denmark for the 1858 tsunami were due to the interference between the western wave (coming from the English Channel) and the northern wave (coming from Scotland). Still, they recognize that the reports of tsunami heights were larger for the North Sea than for the English Channel. The results obtained in Section 4.3 agreed with these reports showing high damping of the Channel wave, suggesting that the interference was not likely the cause of larger run-up in Denmark and Germany. Additionally, the tsunami was reported to arrive in Germany about one hour later than in Denmark; therefore the higher run-ups in these countries were due to a wave coming from the north.

Among the results of Section 4.3 in the GBM, the maximum tsunami heights for the (e) and (f) cases were located at the north coast of East Frisian Islands, at the west coast of Sylt Island, both in Germany and at Blåvandshuk in Denmark (Figure 4-9e and Figure 4-9f). Årgab lies outside of the GBM so it was not possible to produce a good estimation of the maximum tsunami height there. Nevertheless, the refNSM results showed high tsunami heights offshore Årgab for cases (e) and (f), higher for the later than for the former (compare Figure 4-8e and Figure 4-8f). The differences in arrival times at those three locations for case (f) also matched better the 1858 reports than for case (e), Figure 4-11.

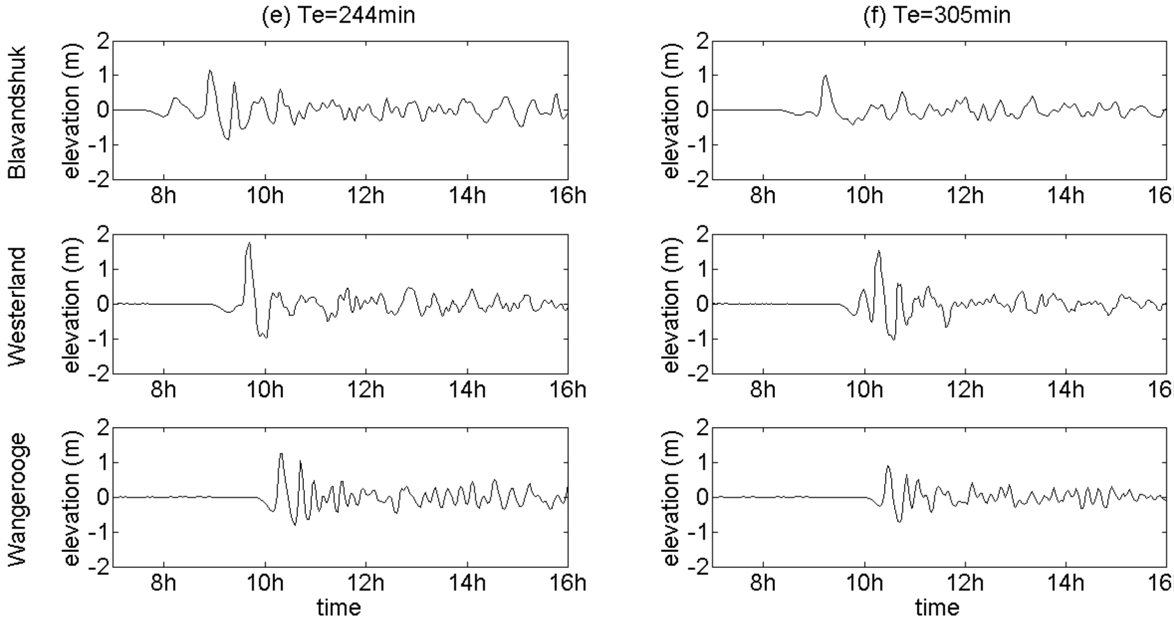

Figure 4-11. Time series of water height, in meters, on Blåvandshuk (Denmark), Westerland and Wangerooge (German Frisian Islands) for cases (e) and (f) of Section 4.3.

The leading depression of the tsunami wave at Blåvandshuk, Westerland and Wangerooge stations (Figure 4-11) was much smaller than the subsequent elevation; this could be the reason for no leading depression reported by eyewitnesses in those places (NEWIG and KELLETAT, 2011). The reports of the 1858 tsunami run-up are higher for Blåvandshuk than for Westerland and Wangerooge, and the model results showed higher runups for Westerland than for the other two places. The difference may be due to inaccuracies in the witnesses' reports, or the tide at the moment the tsunami arrived. It was performed a simple analysis of the influence of tides on tsunami heights in Section 4.6 and it was found that the latter were affected by the tidal phase.

The timeline and wave height of the tsunami observations and the model results point that the wave that arrived in the south of the Netherlands was probably the damped western wave and it was too small to be noticed at German shores. Few hours later, the northern wave arrived to Denmark and then to Germany, with a direction of incidence similar to case (f), corresponding to an origin further east of the 1755 tsunami source given by NOAA (NGDC, 2012): 36°N and 11°W. Other authors propose epicentres further east for the 1755 earthquake, for example Moreira (1989), Reid (1914) and Zitellini (1999), all at 10°W. Also, the tsunami source could have been at Biscay Bay or offshore from Morocco.

4.5. Comparison of storm surges and tsunamis

Storms are common phenomena in the North Sea. The surges they provoke have caused inundations and damages at the German coast, thus dikes have been built along the entire coastline to protect the coastal population. Tsunamis, on the other hand are much less frequent, and are not present in people’s memory, therefore are not taken into account in preventive measures either.

In Figure 4-12 are compared the water levels and depth-averaged flow velocities caused by storm surges and tsunamis at Westerland station, on Sylt Island, because this station presented the highest heights on all the tsunami simulations performed in previous sections. The storm surges of February 1967, January 1976 and December 1999 were plotted; they were simulated as part of the validation mentioned in Section 4.1. For tsunamis, it was plotted the Storegga like tsunami modelled in Section 4.2, and the case (f) of Section 4.3 with the unitary height forcing. Storm surges have much larger durations than the two tsunamis shown. Although landslide-generated tsunami had larger duration and period than earthquake-generated tsunami, its duration is still much shorter than that of storm surges. The maximum magnitude of depth-averaged flow velocity for case (f) of Section 4.3 was of 1.6m/s, for the Storegga tsunami was of 0.48m/s and for the 1967, 1976 and 1999 storm surges was of 0.74, 0.68 and 0.61m/s respectively

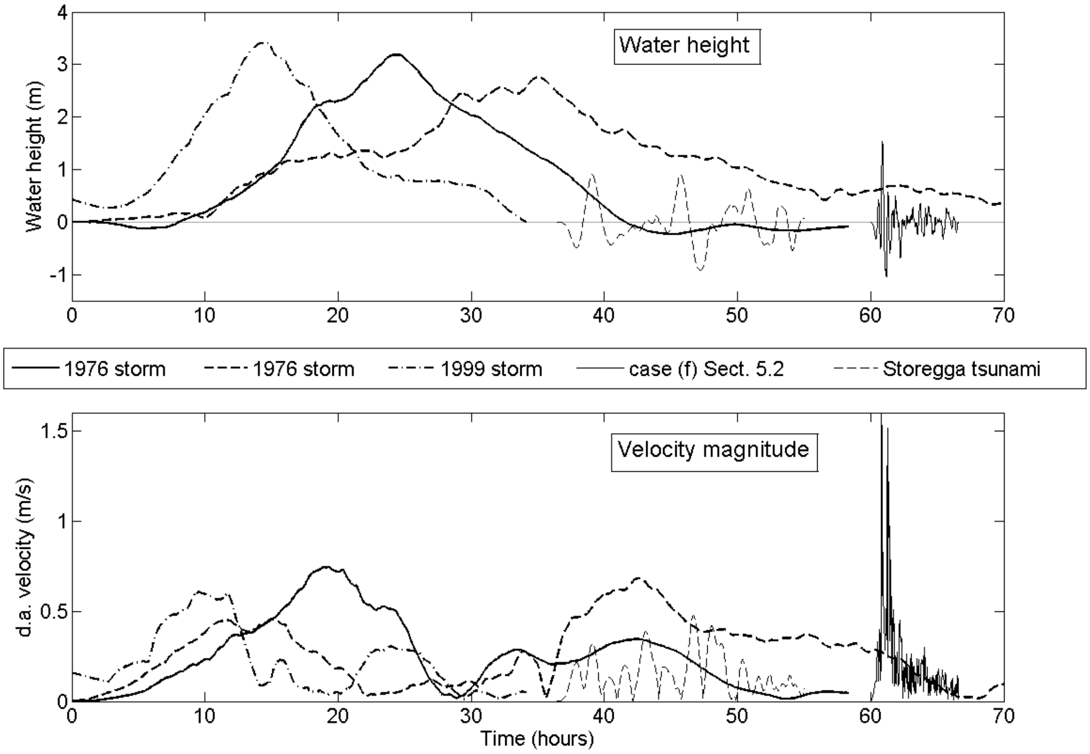

Figure 4-12. Comparison of storm surges and tsunamis on Westerland station, Sylt Island. The upper panel plots water levels and the bottom panel plots depth-averaged flow velocity magnitude. The times were shifted to show the differences more clearly.

4.6. Tsunamis and tides

Tides have been proven to have an impact on storm surges in the North Sea (BRUSS et al., 2010). Tsunamis are usually modelled without considering tidal influence; however, tides have been also proven to impact on tsunami heights (KOWALIK et al., 2006) (KOWALIK and PROSHUTINSKY, 2010). Kowalik and Proshutinsky (2010) superimposed tsunami signals on different stages of the tide on a simple slope channel to explore the influence of tides on tsunamis. The largest tsunami heights resulted during ebbing and low tide, because the change in bottom friction due to the interaction of tsunami and tides was larger at those stages. They conclude that under real conditions, the interaction of tsunami and tides is non-linear and it is given in terms of bottom friction, advection and momentum flux along with changing depths and velocities. Finally, they recommend tides to be simulated together with tsunamis in places where the former are comparable to prevailing depths, as it is the case for the North Sea.

Therefore an N-wave was superimposed to the spring tide of August 14th 1999 to explore the influence of tides on tsunamis heights. To obtain the tidal forcing for the refNSM, an astronomical forcing was imposed at the open boundaries of a larger model: the Continental

Shelf Model (CSM) of Verboom et al. (1992). The resulting water levels and current velocities at the refNSM boundaries were used to obtain the Riemann-invariant boundary condition for 9 days of simulation. The N-wave of Section 4.3, case (a) of unitary height and normal incidence was superimposed to the tides on two different moments, such that the tsunami arrived at Cuxhaven station during high tide and low tide. This procedure was only performed for the north open boundary, on the west open boundary only the tide was prescribed. Then, the tide was subtracted from the model results of the sum of tides and tsunami, and this residual was compared with the tsunami results of Section 4.3 case (a) at Cuxhaven station. If the interaction between tsunamis and tides were linear, the residual should be equal to the tsunami modelled alone.

The results for the two cases, high tide and low tide, are compared in Figure 4-13: pure tsunami with thin lines and tsunami under the influence of tides with thick lines. The influence of tides and its phase on tsunami heights was remarkable. The differences between the pure tsunami and the tide-influenced tsunami were higher if the tsunami arrived during low tide than if it arrived during high tide, agreeing with the results from Kowalik and Proshutinsky (2010) for tsunamis at Cook Inlet and Bruss et al. (2010) for storm surges at the German Bight. However, despite the tidal phase, the pure tsunami signal presented higher heights than the tide-influenced tsunami.

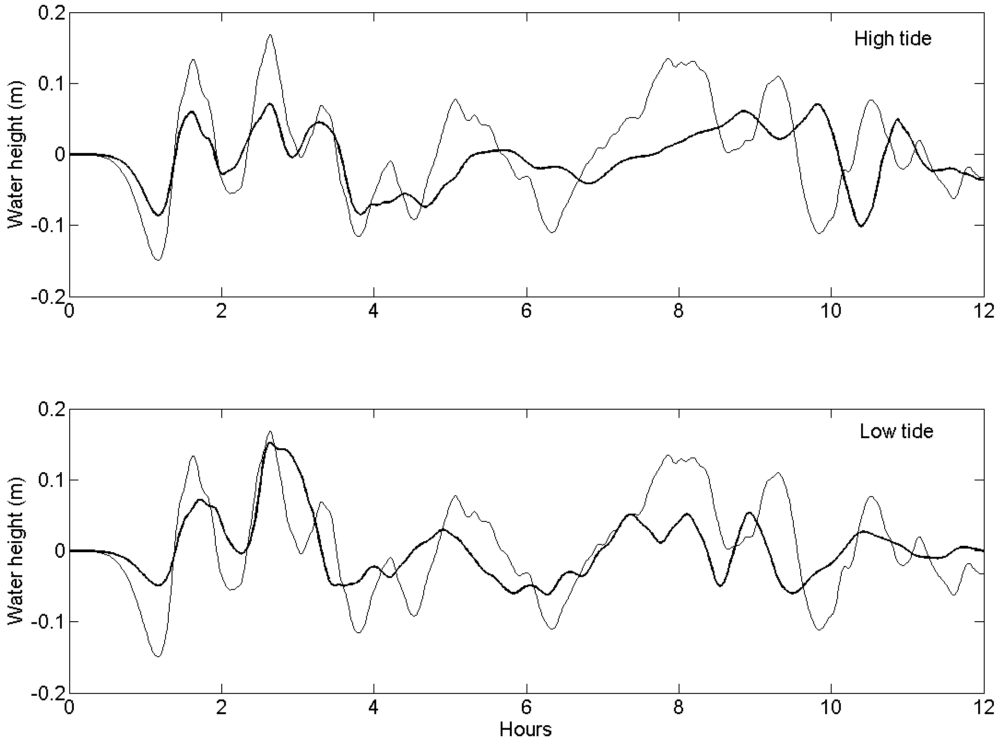

Figure 4-13. Influence of tides and tidal phase on tsunamis. Comparison of tsunami heights obtained without considering tides (thin line) and tsunami heights obtained taking tides into account (thick line).

4.7. Discussion

Tsunami risk in the North Sea was explored in this Chapter by means of N-waves imposed at the open boundaries of the refined North Sea model. Each tsunami affected different regions on the North Sea basin and the German Bight. The results obtained suggest that tsunami risk at the North Sea is not as low as other studies had implied. For example, Horsburgh et al. (2008) simulated several scenarios of tsunamis arriving at the United Kingdom shores from the offshore region of the Iberia Peninsula. They concluded that the Galician Rise (Figure 4-1) somehow shields Ireland and the west coast of Great Britain and also that the extent of the continental shelf of the Celtic Sea dissipates energy of tsunamis coming from the south before they reach these coasts. However, they did not model what could happen at Scotland or inside the North Sea. From the travel time plot of the 1755 Lisbon tsunami (Figure 4-7), tsunamis coming from the south propagate north along the continental slope and through the Rockall Trough at high velocities, and then get refracted around Scotland and enter the North Sea. As the propagation along the continental slope and the Rockall Trough occur at large depths, a tsunami wave traveling through this path probably experiences very little energy loss.

This energy focusing mentioned above is related with the incidence angle. Comparing the results from the two historical tsunamis, the Grand Banks-like tsunami (case c) presented water height amplification bellow those for the Lisbon-like tsunami (case d). The larger distance travelled by the Grand Banks-like tsunami cannot be blamed on this difference because incident waves of unitary height were employed in all the cases. A Lisbon-like tsunami would be more dangerous because the orientation of its arrival at the North Sea: its directionality, and not only because of its closeness. For the 1858 tsunami, the location of the most affected regions was well reproduced along with the tsunami arrival times along the German Bight and Denmark. The results obtained here indicate that the reason for the highest heights reported for this tsunami in this region was directionality rather than wave interference. This directionality points to a source for this tsunami further east from the Gorringer Banks.

Important differences were found also due to the forcing type employed. Normal incidence earthquake-type N-wave (case a) affected mostly the southern coast of the Netherlands and North Sunderland in England. The Storegga-like tsunami simulated in Section 4.2, also with normal incidence, affected mostly inlets along Scotland and England. Landslide-generated tsunamis have wavelength ranges different than earthquake-generated tsunamis.

Among all cases analysed for the German Bight, the most dangerous tsunamis were those generated by earthquakes south of the North Sea, because of their incidence direction. Storegga-like tsunami seems not to be dangerous, as its simulated heights were about half than those provoked by the storm surges. The tsunami wave of Section 4.3 was also smaller than the storm surges, yet it was generated employing a wave of unitary height as input; therefore if the incoming wave is higher, this tsunami wave could be also higher. Indeed, the highest tsunami heights reported historically at the German Bight are about 4m, comparable to the height of the maximum storm surge recorded at this region. But, the magnitude of the depth-averaged flow velocity generated by tsunamis was comparable or larger than that generated by storm surges, suggesting that a large tsunami may cause more damage than a storm surge. Then, even when the tsunamis last much less and their water levels can be smaller, their flow velocities can be larger than the storm surges causing more damage. Therefore, tsunamis should not be dismissed as a threat for the German Bight.

The interaction of tsunamis and tides was tested using one tsunami case in two tidal phases. The results showed that for the North Sea this interaction is clearly non-linear. The tsunami heights were higher for the tsunami arriving during low tide; however the tsunami heights without considering tides were the highest ones. As it is not possible to predict a tsunami event it is not possible to superimpose the right tide forcing when tsunami forecast is performed. In the case studied here, the modelling of the tsunami alone could be considered as a reasonable approximation to the maximum possible tsunami height at Cuxhaven. Still, to generalize this result more research would be desirable considering other tidal phases, tsunami frequencies and heights, and other locations along the German Bight.

N-waves were chosen as input for the modelling in the North Sea due to the lack of tsunami records in this region. Tsunami morphodynamics was not simulated on the North Sea because there were no data to compare the tsunami caused morphological changes, and because the results of Chapter 5 showed that N-waves might not be appropriate to simulate tsunami morphodynamics.

5. Effectiveness of N-waves for predicting morphological changes due to tsunamis

In this experiments were compared the morphological changes caused by leading elevation (LE) and leading depression (LD) N-waves and tsunami waves. The waves were considered to propagate along a channel with a long constant slope, and of which bed was composed of sediments of uniform size. The morphological changes they caused were analysed, focusing on the uprush and backwash of waves with different orientation (leading elevation versus leading depression). The study considered three different values of bed slope and two values of wave height. Four different N-waves were considered: three LEN and one LDN, as well as four real tsunami shapes.

5.1. Model setup

The numerical experiments were performed on a long rectangular channel. The grid consisted on nx cells of 12m length in the x-direction (cross-shore), one cell of 100m in the y-direction (alongshore) and 10 σ-layers over the vertical. The thickness of σ-layers decreased from the surface to the bottom in order to achieve better resolution near the bed. Each σ-layer did not have the same width or depth over the whole domain, as the number of σ-layers remained constant even though the water depth is not uniform. The results of the numerical model did not vary when the cross-shore grid size was changed to 6m, hence the x-wise cell length was kept at 12m. The channel bed had a single slope s and was composed by one class of equally distributed non-cohesive sediments of medium size 500μm. The main conclusions of this work did not change when sediments of medium size between 200μm and 900μm were employed instead of 500μm.

In Figure 5-1 is sketched the channel, it shows the length of the channel L, the distance from the open boundary to the original shoreline x_0, the maximum depth of the channel d_0, the slope s, the wave height when imposed at the open boundary, and the x-z coordinates. The distance x_0 and consequently the number of cells in the x-direction (nx) depended on the bed slope. For all the simulations the maximum water depth was d_0=35m and the time step was set to 0.3s resulting in maximum Courant numbers of about 0.46 at the deepest side of the channel. The bed roughness was characterized by a Manning coefficient of 0.025 $m^{-1/3}s$, over the entire domain.

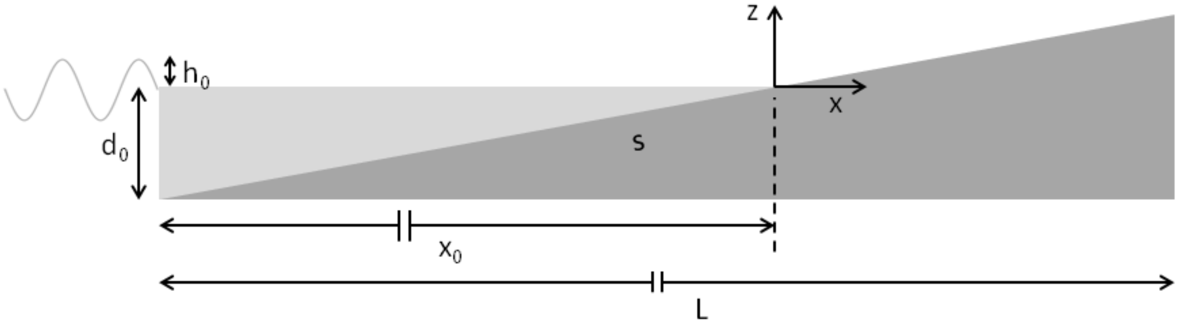

Figure 5-1. Schematization of the rectangular channel.

N-waves employed in the simulations were isosceles N-waves based on Tadepalli and Synolakis (1996) formulation:

$$\eta(t)_{x=-x_0} = \mp\frac{3}{2}\sqrt{3}\cdot H\,\mathrm{sech}^2[\gamma(t-t_0)]\tanh[\gamma(t-t_0)]. \qquad \textbf{5-1}$$

The minus sign in Eq. 5-1 refers to the leading elevation N-wave (LEN) and the plus sign refers to the leading depression N-wave (LDN). Four N-waves were considered, which constants are listed in Table 5-1. The parameters of N-waves were chosen to match the period of the corresponding tsunami waves.

Table 5-1. Name, orientation, γ, and t_0 of the N-waves employed.

Name and orientation	γ (min^{-1})	t_0 (min)	Equivalent tsunami wave
A. Leading Elevation	0.14	45	LE Male
B. Leading Depression	0.14	45	LD Male
C. Leading Elevation	0.09	50	LE Ganares
D. Leading Elevation	0.12	37	LE Hanimaadhoo

Tsunami shapes were obtained after the recorded 2004 Indonesia tsunami at Ganares, Hanimaadhoo and Male, Maldives (UHSLC, 2013), and were amplified to a uniform maximum wave height of H=4m and H=5m for these simulations. The leading wave of Male record was similar to N-wave A. This tsunami shape was originally leading elevation and it was inverted to consider also the leading depression case comparing with N-wave B. The leading wave of Ganares and Hanimaadhoo records was similar to N-waves C and D respectively. Both N-waves and tsunami waves with initial heights of H=4m and 5m were imposed on the channel with water depth of d_0=35m and bed slope of s=0.01, 0.015 and 0.02 composed of sediments with medium size D=500µm.

5.2. Comparison of N-waves and tsunami waves

Figure 5-2, Figure 5-3, Figure 5-4, and Figure 5-5 correspond to LE Male, LD Male, Ganares and Hanimaadhoo cases, and are divided in four subfigures in the same way. In subfigure (a) is shown the waveform of the tsunami wave compared to the equivalent N-wave. In subfigure (b) are shown the time derivatives of both waveforms. In subfigure (c) are shown the runup of both waveforms. And in subfigure (d) are shown the final morphological changes caused by the tsunami wave and the N-wave. In all cases the quantity corresponding the tsunami wave is plotted as a solid line and the equivalent quantity corresponding the N-wave as a dashed line.

The chosen N-waves and tsunami waves provoked very similar maximum water levels and inundation distances between equivalent cases (Figure 5-2c, Figure 5-3c, Figure 5-4c, and Figure 5-5c). Yet, the final bed level changes they caused were very different between them (Figure 5-2d, Figure 5-3d, Figure 5-4d, and Figure 5-5d). The largest difference was for case A, LE Male (Figure 5-2), and the smallest for case C, Ganares (Figure 5-4). The patterns for N-waves were simpler than for tsunami waves: composed only of one erosion and one deposition region while for tsunami waves they were composed of several erosion and deposition regions in most cases.

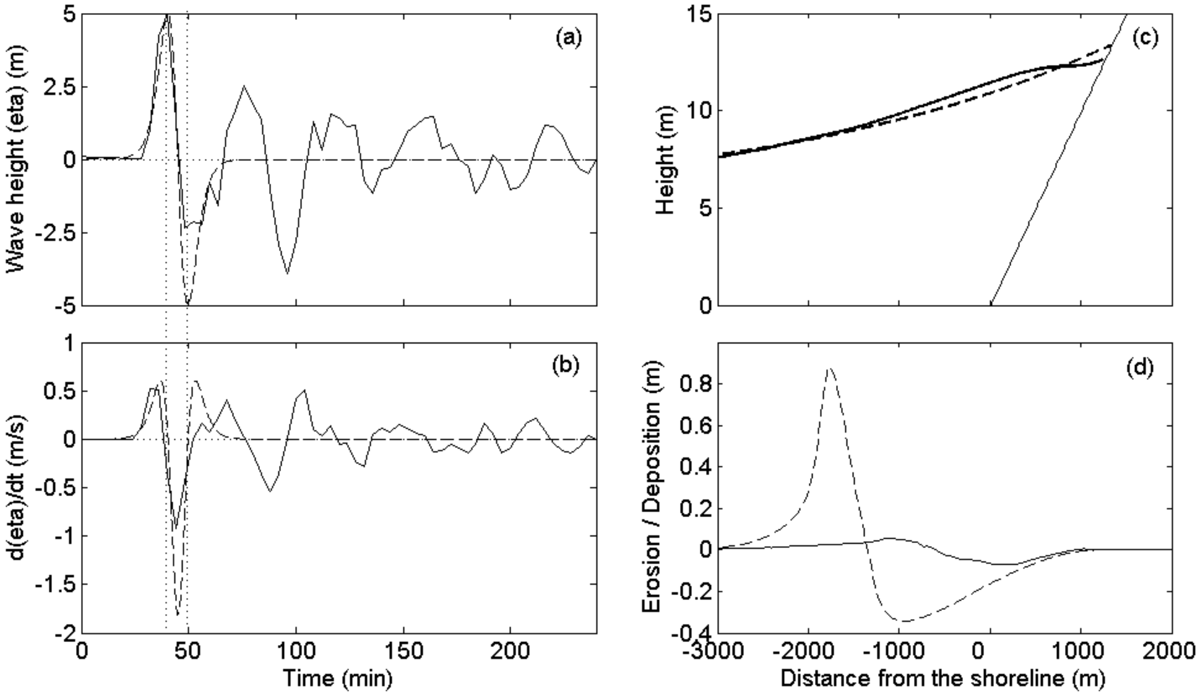

Figure 5-2. Case A: LE Male. (a) Tsunami shape and N-wave. (b) Time derivative of the waves. (c) Maximum water level. (d) Final morphological changes. Lines corresponding to tsunami shapes are solid and to N-waves are dashed. Both cases correspond to s=0.01 and h0=5m.

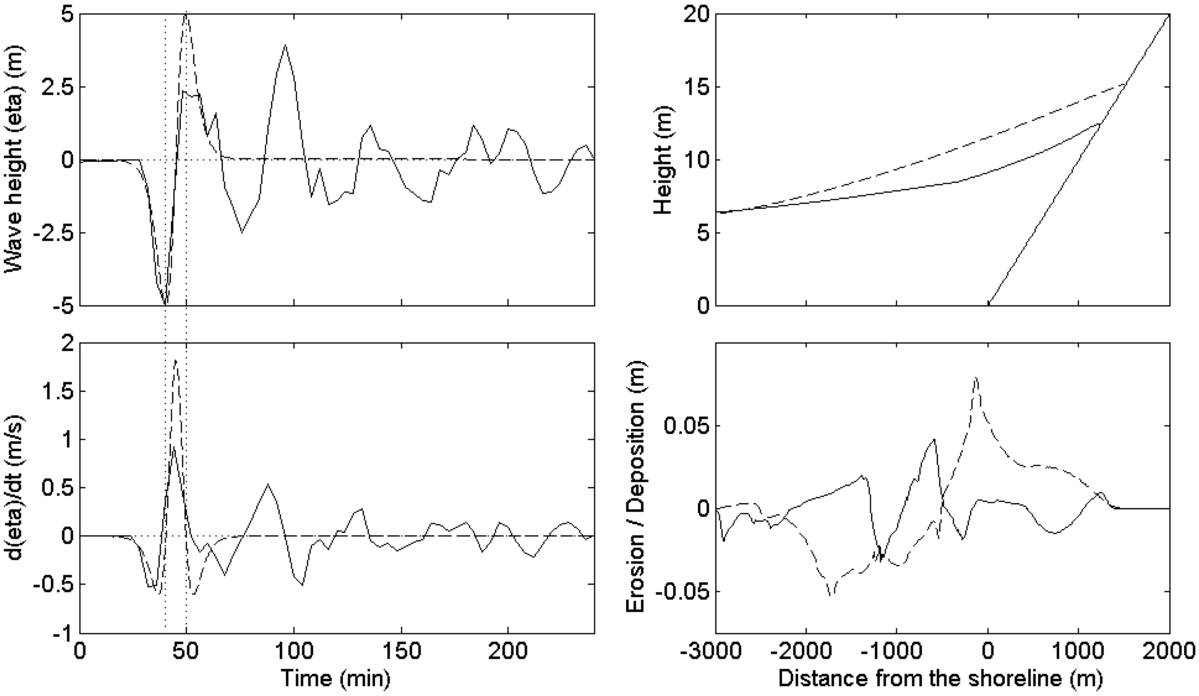

Figure 5-3. Case B: LD Male. (a) Tsunami shape and N-wave. (b) Time derivative of the waves. (c) Maximum water level. (d) Final morphological changes. Lines corresponding to tsunami shapes are solid and to N-waves are dashed. Both cases correspond to s=0.01 and h0=5m.

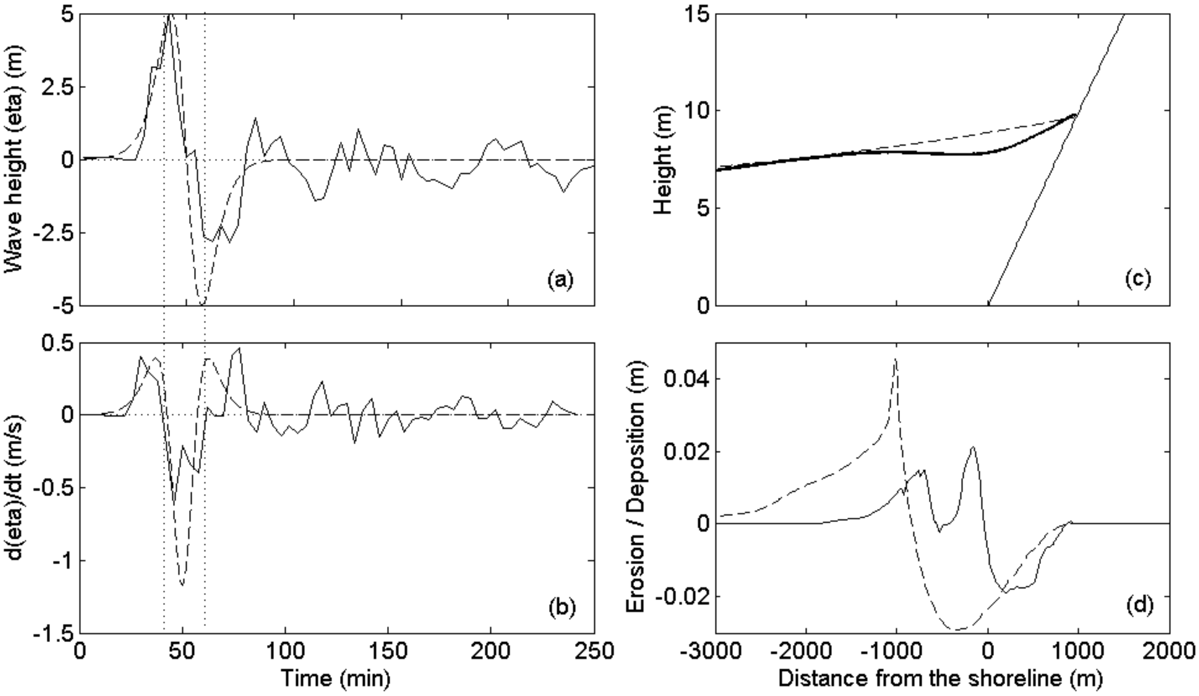

Figure 5-4. Case C: Ganares. (a) Tsunami shape and N-wave. (b) Time derivative of the waves. (c) Maximum water level. (d) Final morphological changes. Lines corresponding to tsunami shapes are solid and to N-waves are dashed. Both cases correspond to s=0.01 and h0=5m.

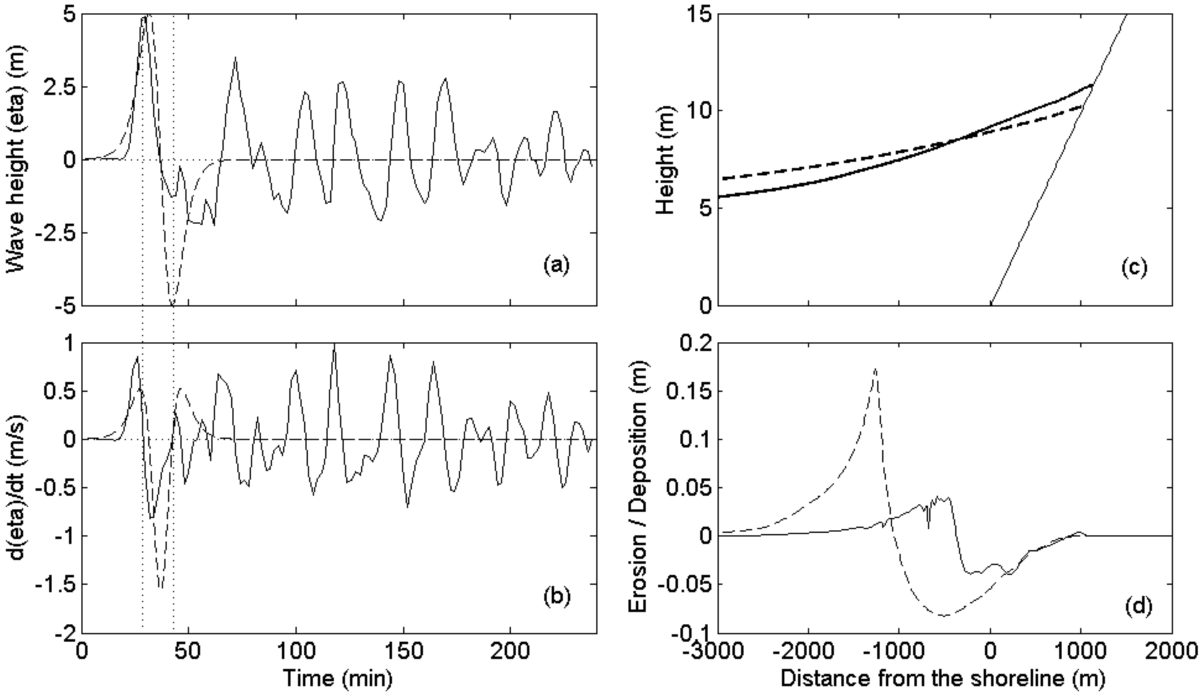

Figure 5-5. Case D: Hanimaadhoo. (a) Tsunami shape and N-wave. (b) Time derivative of the waves. (c) Maximum water level. (d) Final morphological changes. Lines corresponding to tsunami shapes are solid and to N-waves are dashed. Both cases correspond to s=0.01 and h0=5m.

Figure 5-6 and Figure 5-7 show the temporal variations along the channel of the superficial horizontal flow velocity and suspended sediment concentration (SSC) respectively, for N-waves and tsunami shapes for cases A and B: Male LE and LD. On Figure 5-6 and Figure 5-7 the arrows show the direction of the flow and the black contours correspond to zero flow velocity, i.e. flow reversal.

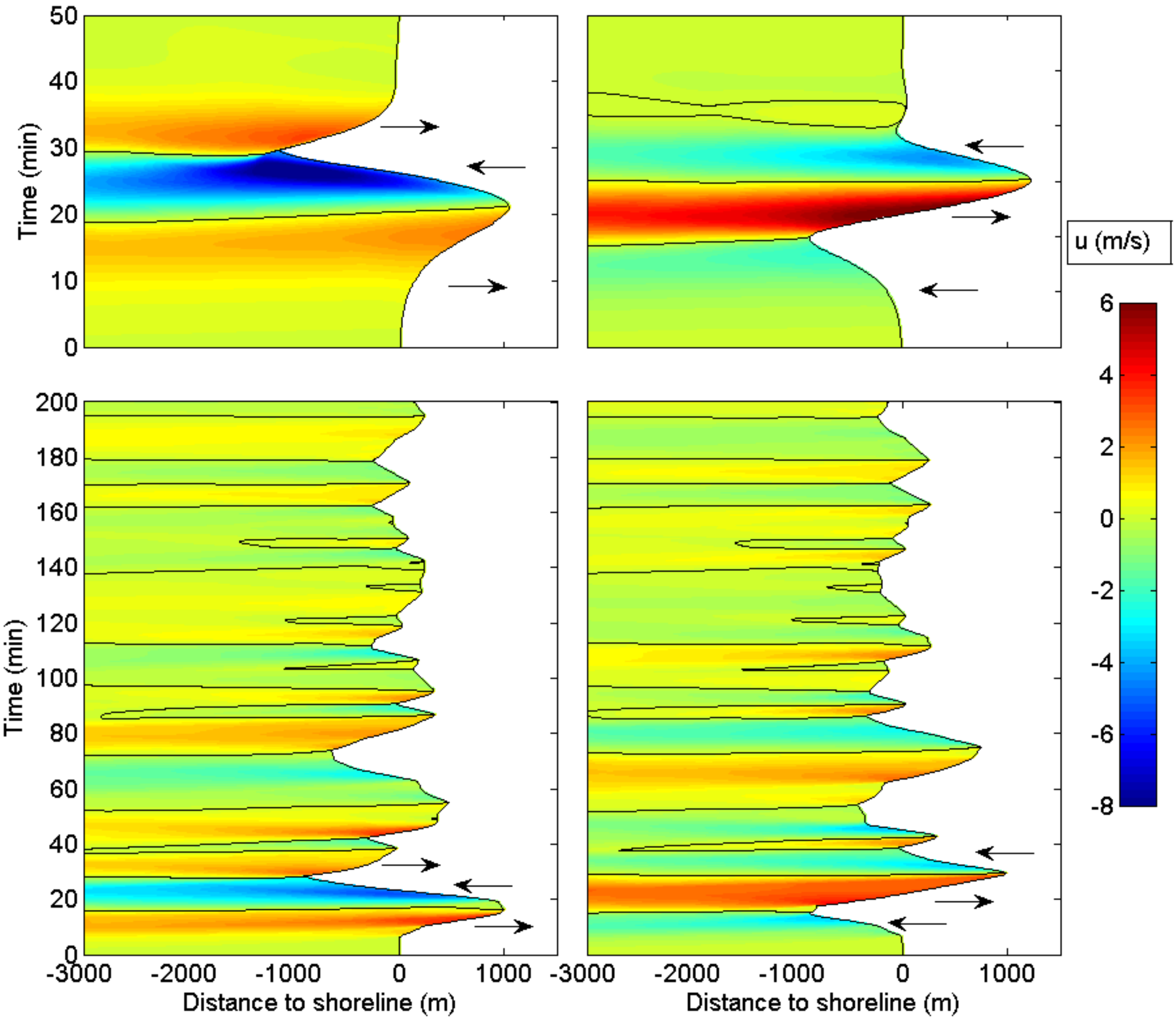

Figure 5-6. Superficial flow velocity (m/s) for (a) LEN, (b) LDN, (c) leading elevation Male wave, and (d) leading depression Male wave. Black contours indicate zero flow velocity. Arrows indicate flow direction in each of the first three stages: onshore (positive) and offshore (negative).

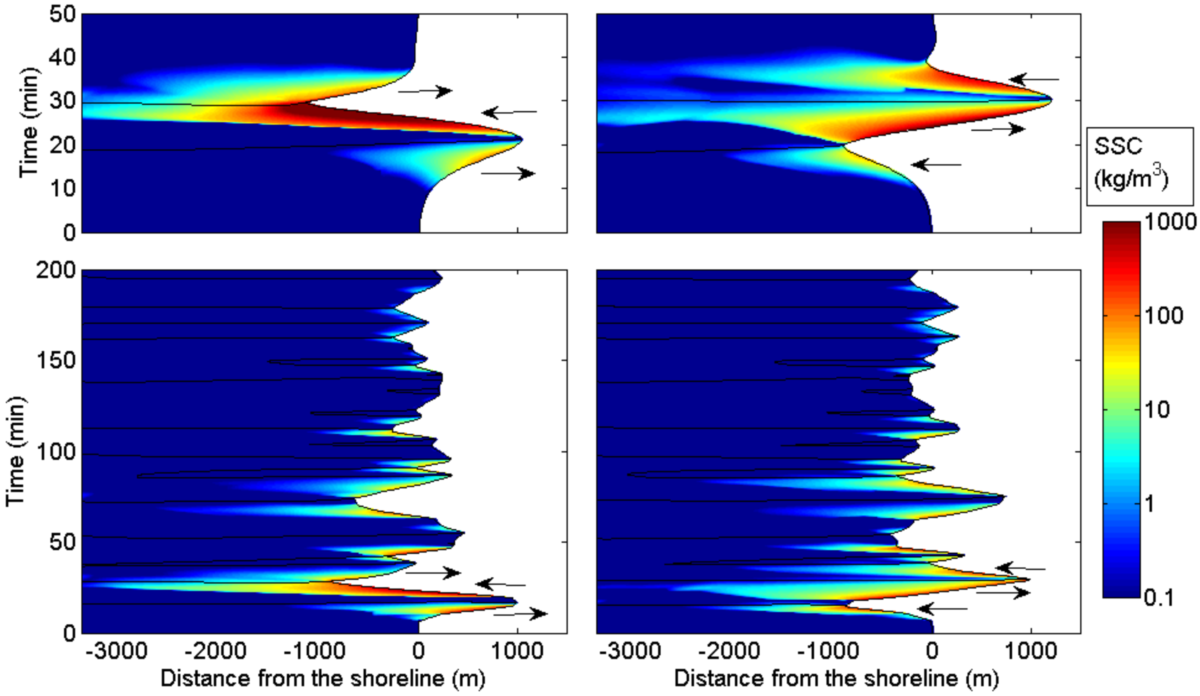

Figure 5-7. Suspended sediment concentration (SSC) (kg/m3) for (a) LEN, (b) LDN, (c) leading elevation Male wave, and (d) leading depression Male wave. Black contours indicate zero flow velocity. Arrows indicate flow direction in each of the first three stages: onshore (positive) and offshore (negative).

The wave was divided in stages for the analysis: 1. between the start of movement until first flow reversal, 2. between the first and second flow reversal, and 3. between the second reversal and zero level again, as indicated in the figures above. The first stage of the wave was flooding for LE waves and ebbing for LD waves, it lasted only between 8 and 10min, and the maximum flow velocities were the smallest of the wave: up to 3.65m/s corresponding to LE tsunami wave (Figure 5-6). The flow velocities were larger for tsunami waves than for N-waves during this first stage as the absolute value of the time derivative of the forcing $\left(\left|{}^{\partial\eta}/_{\partial t}\right|\right)$ for the former was larger than of the latter (Figure 5-2b and Figure 5-3b). The second stage was the longest for all the waves (up to 15min), leading to maximum values of flow velocities (up to 8m/s), agreeing with frictionless results from Carrier et al. (2003). Due to their orientation, the maximum flow velocity corresponded to backwash flow for LE waves and uprush flow for LD waves (Figure 5-6). These velocity magnitudes were larger for the LE waves than for the LD waves (maximum 8m/s vs. 6m/s), because the gravity, as restoring force, acts on the same direction as the forcing for LE and in opposite direction as the forcing for LD. The flow velocities were also larger for N-waves than for tsunami waves, as the former forcing waves had larger $\left|{}^{\partial\eta}/_{\partial t}\right|$ during this stage (Figure 5-2b and Figure 5-3b). For

N-waves, during the third stage occurred the maximum uprush (LEN) and backwash (LDN) flow velocity, while the flow returned to its equilibrium level. However, for the tsunami waves, they occurred during subsequent peaks and troughs, and were smaller than for N-waves.

Figure 5-8 show snapshots of the suspended sediment concentration at the moment of maximum flow velocity for (a) LEN, (b) LDN, (c) LE tsunami shape and (d) LD tsunami shape, all for Male cases. The arrows indicate flow direction at the time of the snapshot: onshore (positive) and offshore (negative).

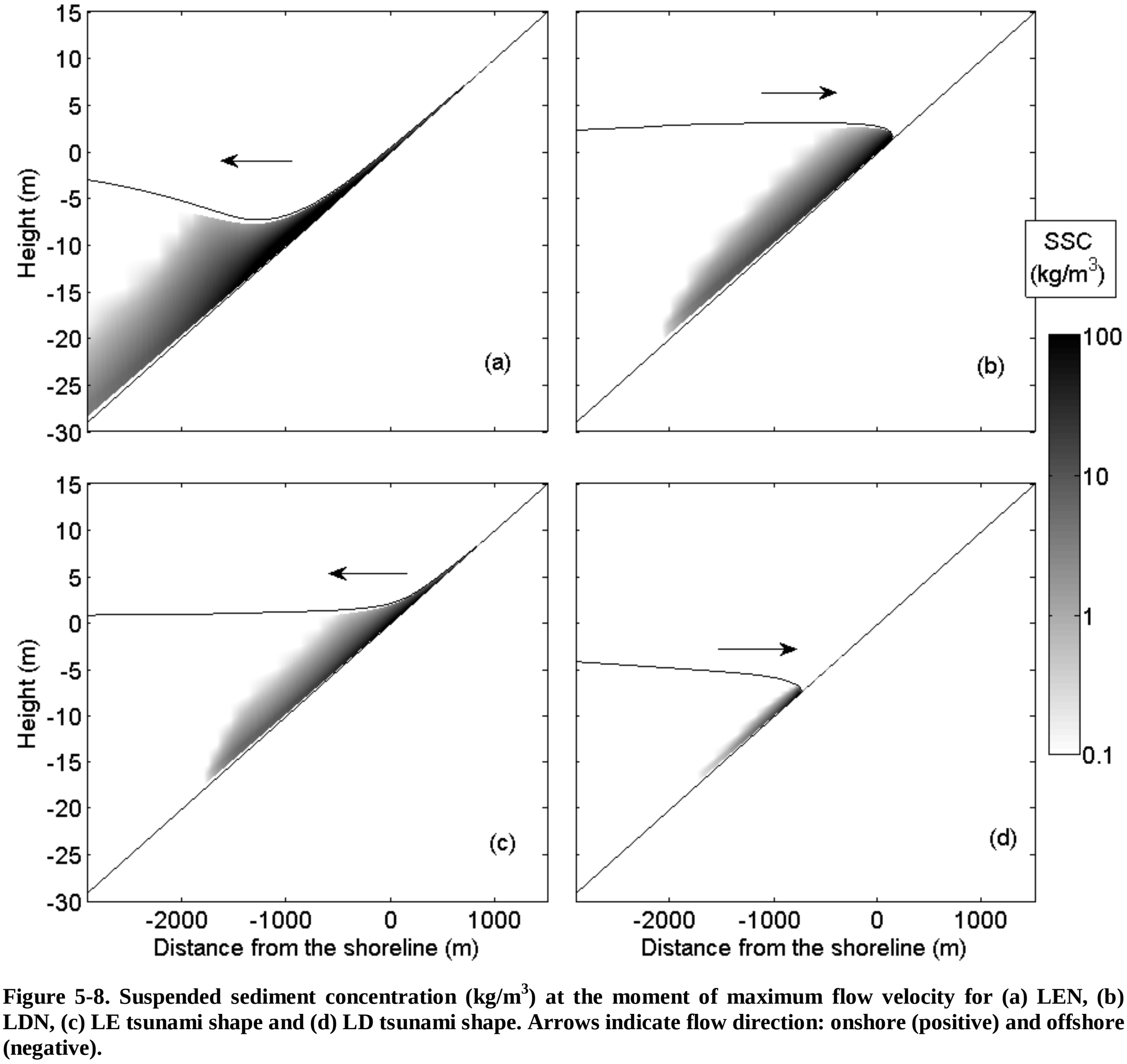

Figure 5-8. Suspended sediment concentration (kg/m^3) at the moment of maximum flow velocity for (a) LEN, (b) LDN, (c) LE tsunami shape and (d) LD tsunami shape. Arrows indicate flow direction: onshore (positive) and offshore (negative).

During the first stage of the wave little erosion happened (Figure 5-7), due to the relatively small flow velocities (Figure 5-6), and the short duration of this stage. The maximum SSC was reached during the second stage (Figure 5-7), through the maximum magnitude of flow velocity. As the velocity magnitudes were larger for the LE waves than for the LD waves, LE cases eroded (Figure 5-7 and Figure 5-8) and transported more sediment than LD cases and this transport was offshore for LE waves and onshore for LD waves (see arrows on Figure 5-7 and Figure 5-8). Similar results have been reported before (EINSELE et al., 1996), (LE ROUX and VARGAS, 2005) indicating that backwash flows are potentially more erosive than uprush flows, although this was blamed on the channelization caused by coastal topography. Also, N-waves eroded and transported more sediment than tsunami waves (Figure 5-8), as they presented larger velocities during this stage.

In Figure 5-9 are plotted the instantaneous morphological changes (solid line) for LE Male tsunami wave (top) and LD Male tsunami wave (bottom) at the moments of first flow reversal (left), maximum flow velocity (middle) and second flow reversal (right). The final morphological changes are shown with a dashed line in all cases.

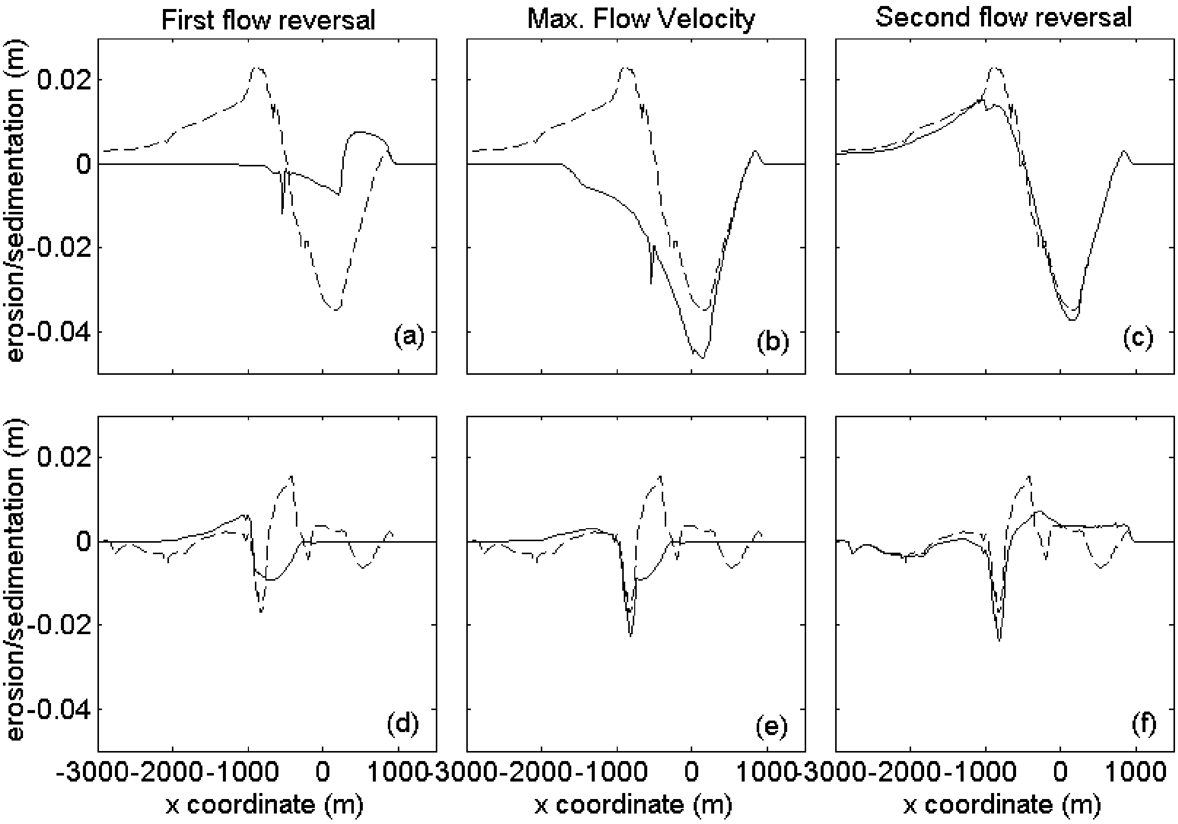

Figure 5-9. Instantaneous morphological changes (solid line) for LE tsunami wave (top) and LD tsunami wave (bottom) at the moments of first flow reversal (left), maximum flow velocity (middle) and second flow reversal (right). The final morphological changes are shown with a dashed line in all cases.

As erosion happened during the first stage, during the first flow reversal deposition took place (Figure 5-9 left) being eroded later during the second stage (Figure 5-9 middle). This deposition was located inland for LE waves and offshore for LD waves, thus the final inland deposits for LE were small. The largest erosion arose during the second stage (Figure 5-9 middle and Figure 5-8), corresponding with largest flow velocities (Figure 5-6) and largest SSC (Figure 5-7). At the end of this stage, the reversal of the flow allowed larger deposition to take place (Figure 5-7 and Figure 5-9 right). This deposition happened mostly around the wave front at that time, offshore for LE waves and around the original coastline and inland for LD waves. Therefore, the orientation of the final bed level changes was opposite for LE waves and LD waves on general terms (Figure 5-2d, Figure 5-3d, Figure 5-4d, and Figure 5-5d), and always larger for the former than for the later as LE waves suspended more sediment than LD waves. This could be the reason for Dawson and Stewart (2007) studies of ancient tsunami deposits corresponding to a marine setting rather than onshore. During the third stage minor rework took place for N-waves. Nevertheless, in most tsunami waves the subsequent peaks and troughs performed larger rework contributing to make the distribution of the morphological changes different than for N-waves.

For the case A, Male LE, the morphological changes had the same shape for the tsunami wave and the N-wave, as the tsunami wave showed only one strong backwash (Figure 5-6c), like the LEN (Figure 5-6a). Even when the tsunami shape had several secondary peaks and troughs, their amplitudes were small compared to the leading peak. This is noticeable on Figure 5-7 left, the largest suspended sediment concentration was located during the first backwash for the LE tsunami wave, as well as for LEN. Consequently, in this case the final bed level changes of both tsunami shape and corresponding N-wave had one erosion and one deposition region only.

Conversely, the distribution of the final morphological changes was not the same for N-waves and tsunami waves on Ganares and Hanimaadhoo cases (Figure 5-4d and Figure 5-5d). The small flow reversal around minute 50 on Ganares tsunami wave (Figure 5-4a) was responsible of the deposition bump located around x=-100m (Figure 5-4d). The second deposition bump located around x=-700m resulted when the backwash ceased and the wave started to run up, around minute 70 (Figure 5-4a). On Hanimaadhoo case, the secondary peaks were responsible for the small deposition bumps located around x=0m and x=+1000m (Figure 5-5a), which was not present with the N-wave.

For the LD Male tsunami wave, the presence of several peaks and troughs caused that the main erosion did not happen only during uprush but also during backwash, unlike LDN (Figure 5-7d and b, respectively). The flow velocity of LD tsunami wave showed five backwash moments with considerable flow velocity (Figure 5-6b) in opposition to LDN where there was only two backwash moments (Figure 5-6d). Moreover, those backwash velocities for LDN were smaller in magnitude than the uprush velocity, while the opposite happened for the tsunami shape. Consequently, there were four deposition regions for the leading depression tsunami wave, compared with one for LDN (Figure 5-3d).

Although there were moments of very high sediment concentration, most of the suspended sediments were located at the wave front and close to the bottom rather than distributed over the whole water column and the whole channel (Figure 5-8). The cause is the relatively small duration of tsunamis in general and N-waves in particular, which does not allow the suspended sediment to distribute over the whole water column and the whole domain. Nevertheless, in case LEN A the SSC extended further offshore and upper on the water channel than in other cases (Figure 5-8a). This would explain the much larger morphological changes caused by this wave with respect to the others. Also, in case LDN A (Figure 5-8b) the SSC extended further offshore and upper than for the equivalent LD Male tsunami wave (Figure 5-8d), explaining larger erosion and deposition for the former than for the latter. This effect can only be observed employing models considering vertical variations, as the one employed here. Depth-averaged models would overestimate the suspended sediment concentration as they consider the sediment concentration close to the bottom as uniform over the whole water column.

5.3. Variations on the Manning Coefficient

The value of the Manning’s coefficient depends on the characteristics of the seabed, as the size of the sediment for example, and is rarely uniform. Nevertheless, in tsunami simulations usually a general and uniform value is used. Here a value of n=0.025 $m^{-1/3}s$ was employed for the Manning's coefficient in all the simulations, as this is the typical value for a coast without vegetation according with Levin and Nosov (2009, p.214). Nevertheless, Lynett et al. (2012) says that the characteristic value for a smooth and even ocean bottom is $0.02m^{-1/3}s$ and Satake (1995) says that a typical value of n for coastal waters is 0.03 $m^{-1/3}s$. Therefore, the propagation of the tsunami wave of case A (LE Male) was repeated employing values of $n=0.02m^{-1/3}s$ and $n=0.03m^{-1/3}s$, and keeping all the other variables the same.

Figure 5-10 shows (a) the maximum water elevations, (b) the maximum offshore velocities and (c) the final bed level changes caused by the tsunami shape on the channel with the mentioned values of the Manning's coefficient. The offshore deposition was about ten-times larger with $n=0.02m^{-1/3}s$ than with $n=0.025m^{-1/3}s$; and about twice with $n=0.025m^{-1/3}s$ than with $n=0.03m^{-1/3}s$ (Figure 5-10c). This is a very large variability, considering that the variations of the runup with the Manning's coefficient were only of about 2% (Figure 5-10a). The offshore velocity also varied noticeably with the Manning's coefficient (Figure 5-10b), being the reason of the differences on morphological changes.

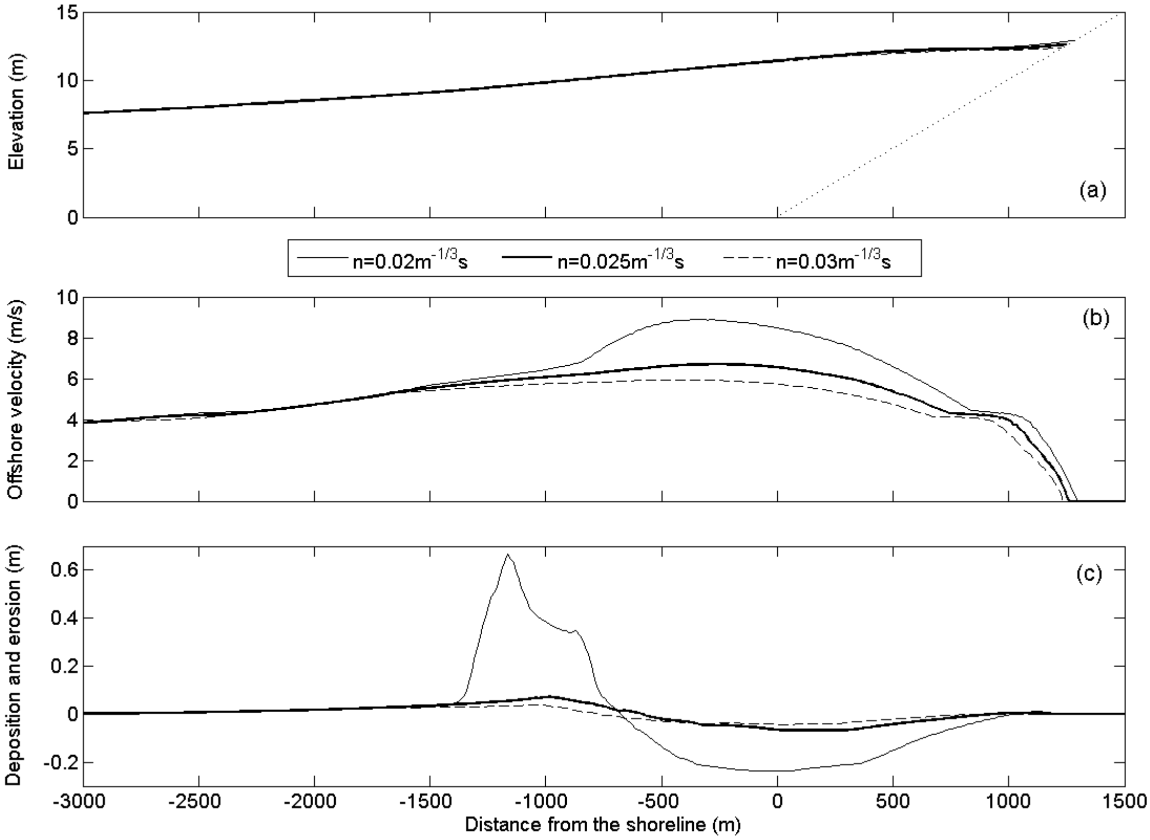

Figure 5-10. (a) Maximum water level, (b) Maximum offshore velocity and (c) final morphological changes caused by the real tsunami shape employing several Manning's coefficients for LE tsunami wave.

5.4. Discussion

Even when leading depression N-waves caused larger runup than leading elevation N-waves, they caused smaller morphological changes. Furthermore, it was found that the erosion and deposition patterns caused by tsunami and N-waves depended on their orientation. The sediment deposition was located mostly offshore for LE cases and inland for LD cases. The opposite happened with sediment erosion, it was located mostly inland for LE cases and offshore for LD cases. Then, regarding inland morphological changes, leading elevation waves caused mainly erosion and leading depression waves provoked mainly deposition.

For the cases examined here, N-waves did not reproduce the morphological changes caused by tsunami waveforms whose leading wave was comparable; even when the N-waves had very similar runup than the tsunami waveforms. The main reason was the differences on the steepness of the waveform. Tsunami waveforms had smaller slopes $\left(\left|{}^{\partial\eta}/_{\partial t}\right|\right)$ than the N-waves during the second stage of the waves (between dotted lines in Figure 5-2b, Figure 5-3b, Figure 5-4b, and Figure 5-5b). These milder slopes meant that for the tsunami shapes the flow velocities during the second stage were up to almost half than for N-waves (Figure 5-6). The smaller flow velocities of the tsunami waves suspended about three times less sediment than N-waves (Figure 5-7) and produced sediment deposits up to ten times thinner than N-waves (Figure 5-2d, Figure 5-3d, Figure 5-4d, and Figure 5-5d). The large differences plotted between morphological changes caused by tsunamis and N-waves were also observed when other values of bed slope were considered, as well as other values of wave height, then they were not a result of a particular set of parameters.

This result should still ideally be confirmed by further experiments. However, the employment of N-waves as parameterization of tsunami flow velocity and morphological changes should be done with care, and considering the wave steepness additionally to the wave height and period. The tsunami caused morphological changes should be analysed case by case at specific locations in order to gain further knowledge about parameters affecting morphodynamics and hydrodynamics of a particular tsunami.

The variations on the flow velocity were also responsible for the large differences on erosion and deposition when the Manning's coefficient was changed. The Manning's coefficient defines the boundary condition at the bottom for the horizontal flow velocity, and then influences the whole velocity profile. The reference concentration is calculated from the bed shear stress (Eq. 2-41), which depends on the flow velocity at the bottom and the amount of sediment eroded and deposited is calculated from the reference concentration.

Previous studies have shown that for non-breaking solitary waves the effect of bottom friction in runup is minor (LYNETT et al., 2002), (LIU et al., 1995). Nevertheless, Apotsos et al. (2009) found that if the offshore bed roughness increased, the amount of sediment eroded and deposited decreased, because of differences in the flow velocity. Still, the differences found here on the morphological changes due to variations on bed roughness were larger than in the mentioned work and suggest that the choice of this variable should be done carefully in morphodynamic tsunami simulations.

6. Three-dimensional modelling of tsunami-caused morphological changes in Tamil Nadu, east coast of India

6.1. Introduction

On the 26 of December of 2004 at 7:58am local time (00:58hrs UTM) a shallow earthquake (10km depth) of magnitude Mw 9.1 (NGDC/WDC, 2011) shook the north of the Sumatran island. This earthquake, the third largest ever measured (USGS, 2012), generated a huge tsunami that swept the coasts of the Indian Ocean and was recorded on tide gauges on remote places in other basins like Alaska (KAWATA et al., 2012, p.ObservationData) and Brazil (NOAA/PMEL, 2009). The death toll is not certain even yet, as some bodies were never recovered from the sea. The World Health Organization says it was “more than 225,000 deaths” (WHO, 2012), the NOAA database counts almost 227,000 deaths (NGDC/WDC, 2011) but the Japan Research Group for the 2004 tsunami reckons almost 300,000 death and missing people (KAWATA et al., 2012). People from all the continents died and around 30-40% of the casualties were on the source region.

Several circumstances got together to transform this natural phenomenon in a large natural disaster: the relative small size of the Indian Ocean, the complete lack of a warning system for the countries along this basin and the almost complete ignorance of the tsunami phenomenon from people living and having holidays there. About six years later, another earthquake with similar magnitude (Mw 9.0) struck the north coast of Japan causing only less than 10% of the total death-toll of the first one, all in the source region. The differences between the consequences of both tsunamis were listed before: the Pacific Ocean basin is much wider and this allowed the tsunami to lose power as it spread over the ocean; the Pacific Tsunami Warning Center (PTWC) informed all the countries within a couple of minutes after the earthquake happened; and finally the Japanese preparedness for tsunamis is the best in the world.

The Indian Ocean tsunami was chose as case study here for modelling the morphological changes caused for distant tsunamis. The Japanese tsunami was not considered because its damages were mainly local. Tsunami caused morphological changes located very close to the source are very difficult to separate from the co-seismic deformation and its direct consequences as liquefaction.

Here it was performed three-dimensional modelling of the morphological changes caused in five locations along the coast of Tamil Nadu (India) by a tsunami with the same source and magnitude as the Indian Ocean tsunami of the 26th of December 2004. The 2004 tsunami not only inundated land but also changed the coastal morphology in some of the places where it arrived (SRINIVASALU et al., 2007), (JAYA KUMAR et al., 2008), (MASCARENHAS and JAYAKUMAR, 2008), (KENCH et al., 2008), (PARI et al., 2008).

About a month after the 2004 Indian Ocean tsunami, in January 2005, a team of researchers from the National Institute of Oceanography of India (NIO) performed a tsunami survey along the coast of Tamil Nadu. Besides the tsunami inundation limits and runup, they also measured medium sediment sizes and beach profiles (BHATTACHARYA et al., 2005), (ILANGOVAN et al., 2005). They performed three additional surveys in April 2005, October 2005 and January 2006 to measure the recovery of the beaches, although they could not conclude if one year after the tsunami the recovery was complete (JAYA KUMAR et al., 2008). Considering the monsoon-driven dynamics of the region, it is quite possible that the beach profile measured in January 2006 was somewhat similar to what should have been the profile in January 2005 if the tsunami would not have happened. Among the profiles measured by the NIO (JAYA KUMAR et al., 2008) the ones that were chosen to analyse the three-dimensional model results were Tarangambadi, Karaikal, Velangani, Nagore and Samanthan Pettai, due to the closeness between them. Amid them, Nagore and Samanthan Pettai were analysed more carefully due to the finer bathymetry available in their vicinity. Besides the available data by the mentioned surveys, the target region of the study was chosen because it is an open coastline.

6.2. Model setup

A system of five nested domains was employed to fulfil the requirements of resolution, model fastness, stability (CFL) and refinement factor of subsequent grids (Figure 6-1). In the first four domains only depth-averaged (two-dimensional-horizontal, 2DH) hydrodynamic calculations were performed. The fifth and smallest domain will be referred to as TAVE: Tarangambadi to Velangani (Figure 6-1c). There, were also calculated sediment transport and morphological changes in a fully three-dimensional grid, considering five σ-layers in the vertical direction. The number of σ-layers remained constant, consequently their thickness was not uniform over the domain. The thickness of σ-layers decreased from the surface to the bottom in order to achieve better resolution near the bed. The first four domains were nested online between them, meaning that the computations on all of them were performed simultaneously. The hydrodynamic results from the fourth domain along the open boundaries of the TAVE domain were used as boundary condition for the later, in this way it was possible to do the simulation of the morphodynamics only on this level and not in the previous ones.

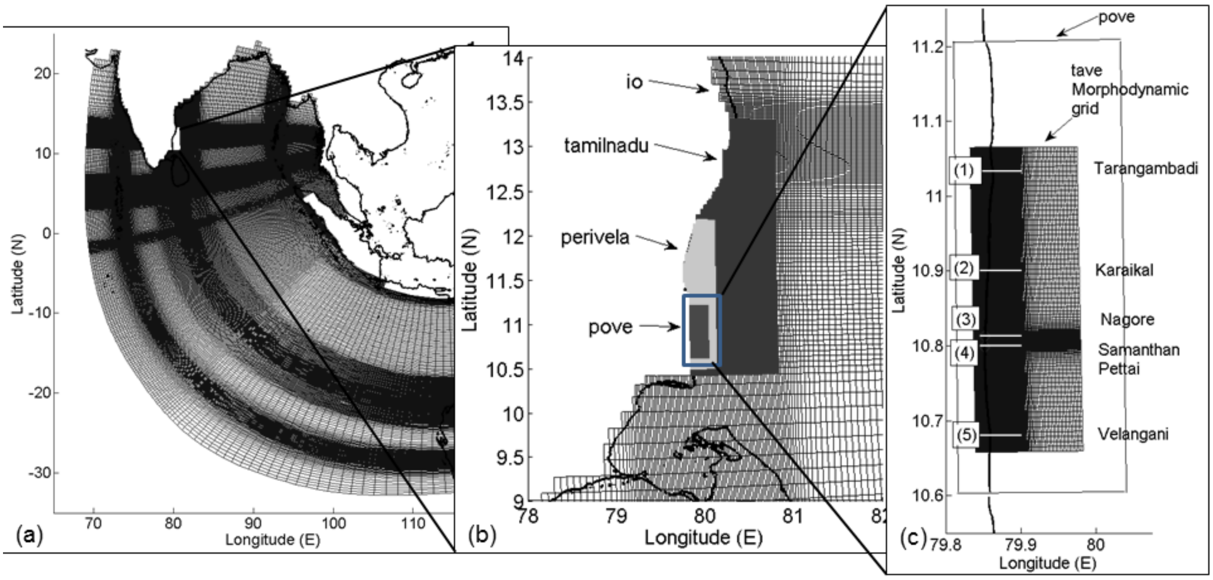

Figure 6-1. Grid system. The resolution is finer close to the interest arriving places and the source region. In (c) the location of the selected cross-sections at which the results are analyzed is shown: (1) Tarangambadi, (2) Karaikal, (3) Nagore, (4) Samanthan Pettai and (5) Velangani.

The first domain comprises the east side of the Indian Ocean, from Indonesia to Maldives. As boundary condition for this domain, zero Riemann-invariants were prescribed to allow the waves to leave the domain without reflections (VERBOOM and SLOB, 1984). The TAVE grid has cell sizes between 3.51m and 295m in the cross-shore direction and between 33.67m and 737.8m in the along-shore direction. The finer cells were located along the beach profiles on Nagore and Samanthan Pettai. These locations were the closest between them among all the locations surveyed by the NIO (about 2km between each other) and there was a large scale nautical chart available in front of them. As the morphodynamic was only modelled on the TAVE domain, there was no sediment flux through its borders. Then, the borders of TAVE domain were chosen accordingly to minimize the error associated with this assumption and it was prescribed boundary conditions of zero transport gradients through them.

The time step employed on the first four domains was of 0.45s, and on the TAVE domain was 0.15s. The maximum values of the CFL stability number was 0.63 for the TAVE domain and varied between 0.18 and 0.4 for the first four domains. In all the grids involved in this system spherical coordinates were used. In the main grid spherical coordinates were essential because of its size, and the nesting procedures in Delft3D require that all the nested grids have the same coordinates.

As initial condition was employed the co-seismic deformation obtained using the same parameters as Chacón-Barrantes (2005) but considering a rupture length of 1000km, resulting on Mw 9.17 (Figure 6-2).

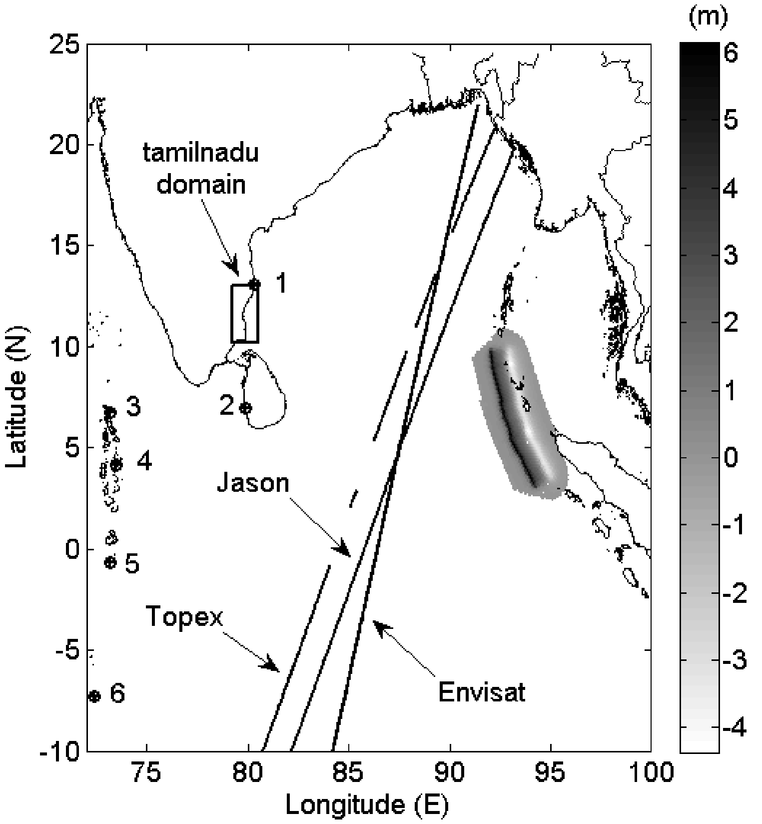

Figure 6-2. Co-seismic deformation used as initial condition for the tsunami model, water levels in meters. The points mark the tidal gauges employed for water level verification (1 Chennai, 2 Colombo, 3 Hanimaadhoo, 4 Male, 5 Ganares and 6 Diegres) and the thick lines show the paths along which the satellite altimetry was recorded. The square next to the Indian coast shows the localization of "tamilnadu" grid.

The bathymetry is very important in tsunami simulations because tsunami propagation speed depends on the water depth (Equation 2-10). Then, the tsunami experiences reflections and refractions in land, islands and bathymetric features during its propagation, and those interactions are the key features in the definition of the tsunami shape (CHACÓN-BARRANTES, 2007a) (CHACÓN-BARRANTES, 2007b). Consequently, bathymetry of the region through the tsunami propagates is important in tsunami driven sediment transport and morphological changes, because the tsunami shape has proved to be determinant on those processes (Chapter 5), (APOTSOS et al., 2009). Finally, when the tsunami approaches the coast, the bathymetry of the arrival region influences its waveform and consequently the morphological changes caused by the tsunami on that region itself (APOTSOS et al., 2011b).

There is global bathymetry publicly available up to 0.5arc-min resolution by The General Bathymetry Chart of the Oceans (GEBCO, 2011), yet in some regions near-shore GEBCO bathymetry is not accurate (FUJII and SATAKE, 2007). Therefore, nautical charts were digitized from the United Kingdom Hydrographic Office (UKHO, 2011) for depths less than 2000m in most part of the domains. Also small scale charts from the UKHO were digitized along the Tamil Nadu coast where available, for a total of 26 nautical charts. Some of the charts included data from surveys as old as XIX century, and some included data from post-tsunami surveys, like the one covering Colombo Harbour which relies completely on surveys performed after the tsunami. Particularly offshore Nagore and Samanthan Pettai the largest scale chart available was the 0575A (UKHO, 2011) with a scale of 1:40,000, still not fine enough for the model, and the source of this chart were surveys done between 1991 and 2009. The data obtained from the digitized nautical charts was interpolated and combined with GEBCO data to create the model bathymetry. Consequently, the model bathymetry is a combination of pre- and post-tsunami survey data. The measured beach profiles on January 2006 in Nagore, Samanthan Pettai, Velangani, Karaikal and Tarangambadi (JAYA KUMAR et al., 2008) were combined with interpolated Shuttle Radar Topography Mission 90m data (SRTM, 2011) to create the model topography. Nevertheless, SRTM topography does not match the measured profiles on any of the locations for any of the surveys performed between January 2005 and January 2006; then the SRTM data around those profiles were modified to avoid large gradients on the bed level.

To assess the model performance, simulated water levels were compared with the corresponding recorded water levels of the 2004 Indonesia tsunami on six coastal stations and along three satellite tracks. The tsunami record on Chennai station was obtained from Nagarajan et al. (2006) and the records on the other coastal stations were obtained from the University of Hawaii Sea Level Center (UHSLC, 2005). The satellite altimetry records were obtained from the NOAA Center for Tsunami Research (NOAA/PMEL, 2011).

Regarding morphological changes, as there are not pre-tsunami profiles available on the surveyed locations, the January 2006 (JAYA KUMAR et al., 2008) profile was employed as the initial beach profile for the simulations, assuming a full recovery by then. This profile was combined with the bathymetry and topography data mentioned before. The difference between January 2005 and January 2006 profiles was employed as a guide of the erosion and sedimentation caused by the tsunami, and the January 2005 profile was employed as a guide of the post-tsunami profile. Both are referred as the observations henceforth. One single class of sediments available over the whole domain was considered with a medium sediment size of 0.25mm, the size reported in Ilangovan et al. (2005) for Nagore.

It was employed a Manning coefficient of 0.025$m^{-1/3}s$ offshore and 0.04 $m^{-1/3}s$ onshore for bed roughness. The offshore value was chosen as it is the characteristic value for a smooth and even ocean bottom and the onshore value was chosen assuming a bed composed of cobbles. Even when the modelled beaches were not composed by cobbles, the higher Manning coefficient allow to take into consideration any vegetation or man-made structures that might be located on the study region. This approach was necessary because the surveys did not include information on the extent of coastal vegetation, rocks or man-made grounds that would allow choosing the Manning's coefficients more appropriately.

Equivalent two-dimensional modelling was carried out to assess the performance of the three-dimensional model versus two-dimensional models, both horizontal (2DH) and vertical (2DV). For the 2DH the model was switched to the depth-averaged version over the same TAVE domain. For 2DV modelling one row of the three-dimensional grid was employed along the Nagore and Samanthan Pettai profiles, with the same five σ-layers over the vertical and the corresponding forcing and bathymetry.

6.3. Modelled Water Levels and Morphological Changes

The water levels computed by the model are compared with the 2004 tsunami heights recorded on six coastal stations on Figure 6-4 and along three satellite tracks on Figure 6-3. The agreement with the altimetry records was good, as they were obtained in deep water where bathymetric features played a minor role. Here the differences on water height and tsunami shape were much smaller despite the noise present on the records, particularly at ENVISAT data.

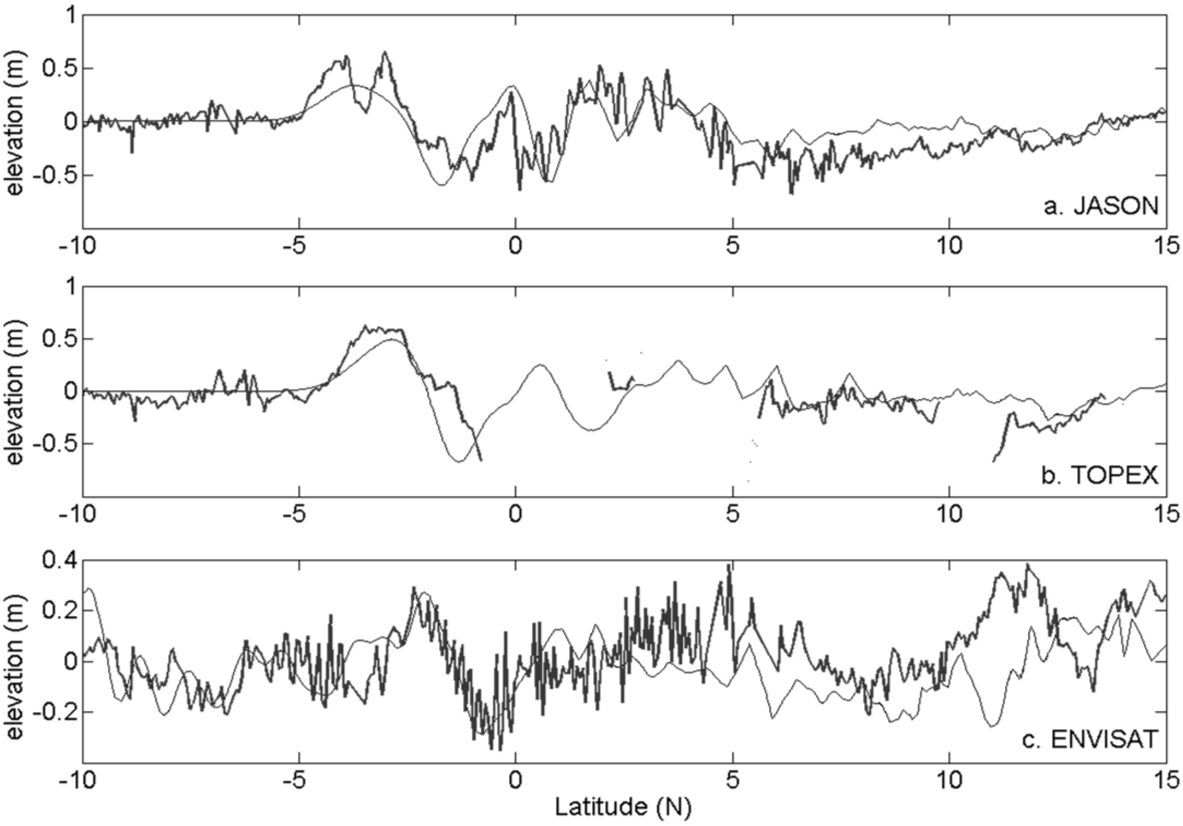

Figure 6-3. Comparison of modelled water level time series (thin lines) with tsunami altimetry recorded by three satellites (thick lines). The track of the satellites is plotted in Figure 6-2.

Regarding coastal records, the model reproduced well the tsunami waveform at Chennai port, although it overestimated the water heights during the first two hours of the tsunami (Figure 6-4a). There the tidal gauge was located inside the harbour, which was not well resolved by the model. The same happened at Colombo, where additionally the harbour was rebuilt after the tsunami and the new bathymetry was employed in the simulations, because the pre-tsunami bathymetry was not available. The incorrect bathymetry might be the reason for the underestimation of the tsunami heights there (Figure 6-4b). The other four coastal stations were located on reef islands (Figure 6-4c to f), where bathymetry is very irregular and yet the model reproduced acceptably well the tsunami shapes and heights in three of them.

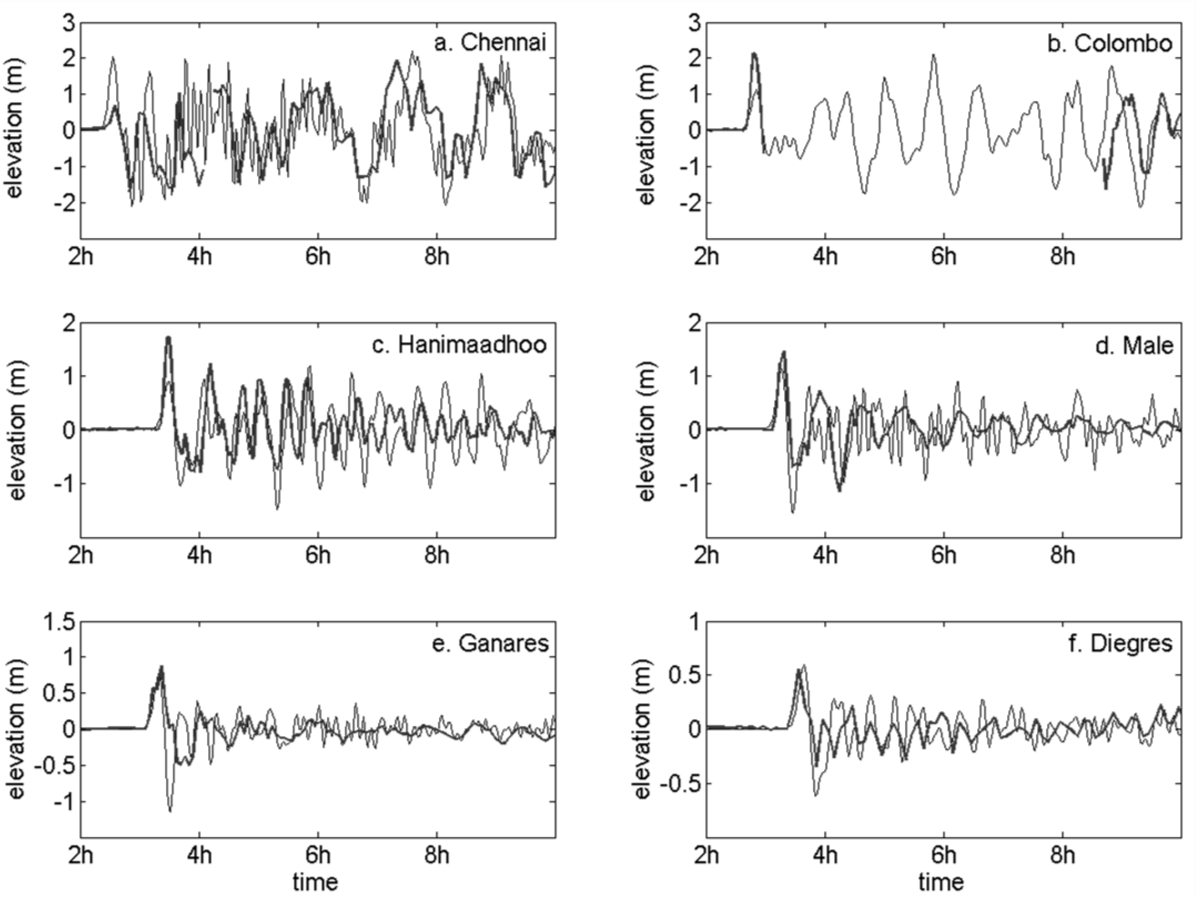

Figure 6-4. Comparison of modelled water level time series (thin lines) with recorded tsunami heights (thick lines) on coastal stations. The localization of these tidal stations is showed in Figure 6-2.

Furthermore, along the studied bed profiles on the east coast of India (Figure 6-1c), three tsunami waves or peaks were obtained in the simulation, agreeing with witnesses' reports, also the incidence angle agreed with fall vegetation (BHATTACHARYA et al., 2005). The measured and modelled tsunami runup and inundation distance are listed in Table 6-1 for the five locations, together with the maximum modelled flow velocity both on- and offshore. The difference on calculated maximum water height and measured runup was only 26cm on Nagore but 97cm in Samanthan Pettai, 1.4m in Tarangambadi, 1m in Karaikal and 52cm in Velangani. On Samanthan Pettai and Tarangambadi the NIO survey team was not able to measure the beach profiles through all the inundation distance (ILANGOVAN et al., 2005); therefore the runup and inundation distance listed in Table 6-1 for these two locations correspond only to the point until which they were able to measure.

Table 6-1. Observed runup and inundation distance (ILANGOVAN et al., 2005), and modelled maximum water height, inundation distance and maximum flow velocity. (*) Locations where it was not possible to measure the inundation distance further than that, due to inaccessibility reasons.

Location	Measured Runup, m	Modelled Max. Water Height, m	Inundation distance (m)		Max. Modelled Flow Velocity (m/s)	
			Observed	Modelled	Onshore	Offshore
Tarangambadi	4.351*	2.94	160*	200.0	2.58	1.58
Karaikal	2.638	3.69	199.5	453.3	2.80	2.05
Nagore	3.145	3.40	862	601.6	3.15	3.49
S. Pettai	4.515*	3.55	150*	161.9	4.75	1.88
Velangani	3.925	3.41	325	200.8	2.54	2.02

In Figure 6-5 are shown the maximum onshore (thin line) and offshore (thick line) flow velocities over the water column during the whole simulation. Only along Nagore profile the maximum offshore flow velocity was slightly larger than the maximum onshore flow velocity. In general both maximum on- and offshore flow velocities had comparable magnitudes, except along Samanthan Pettai, where the onshore velocity was more than twice the offshore velocity. Over the whole domain, the maximum on- and offshore velocities were located around the original shoreline.

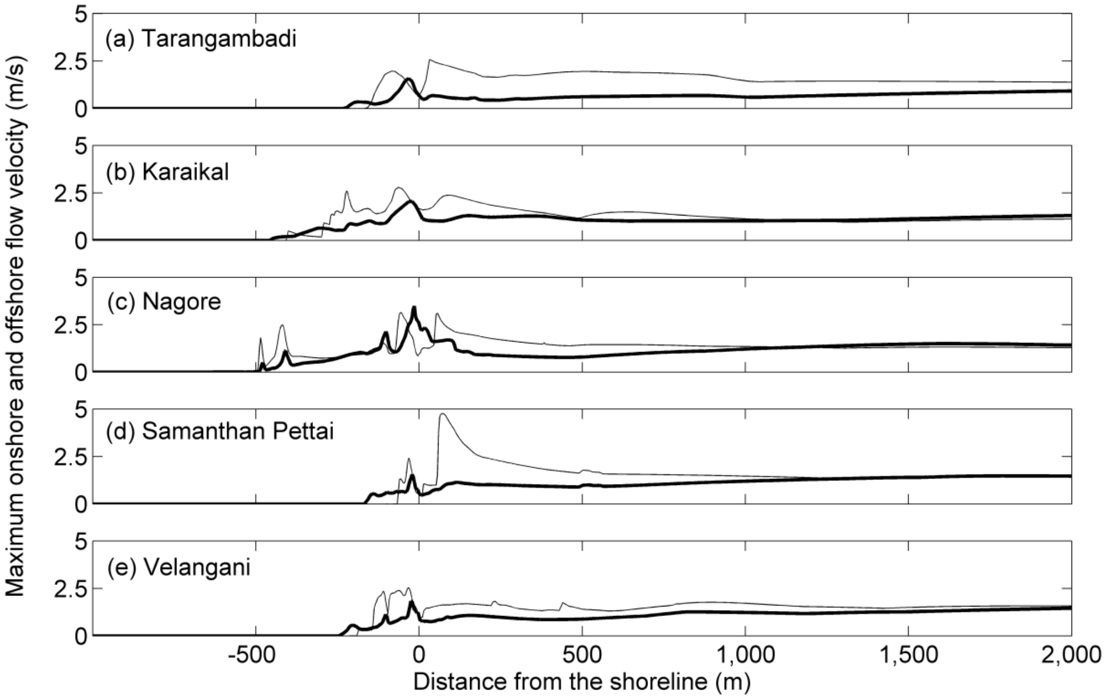

Figure 6-5. Maximum onshore (thin line) and offshore (thick line) flow velocities along the studied profiles. The location of the profiles is shown in Figure 6-1c.

The final modelled morphological changes, erosion and deposition, along the five studied beach profiles are shown with a thin line in Figure 6-6. They were compared with the difference between 2006 and 2005 bed profiles, employed as a guide of the tsunami caused morphological changes. Along all the beach profiles the model reproduced well the patterns of erosion and deposition caused by the tsunami. However, the magnitude of the resulting morphological changes was smaller than the observations on all cases. Along the three southernmost profiles the modelled changes were closer to observations than along the two northernmost profiles, but still much smaller than the equivalent tsunami-caused effects.

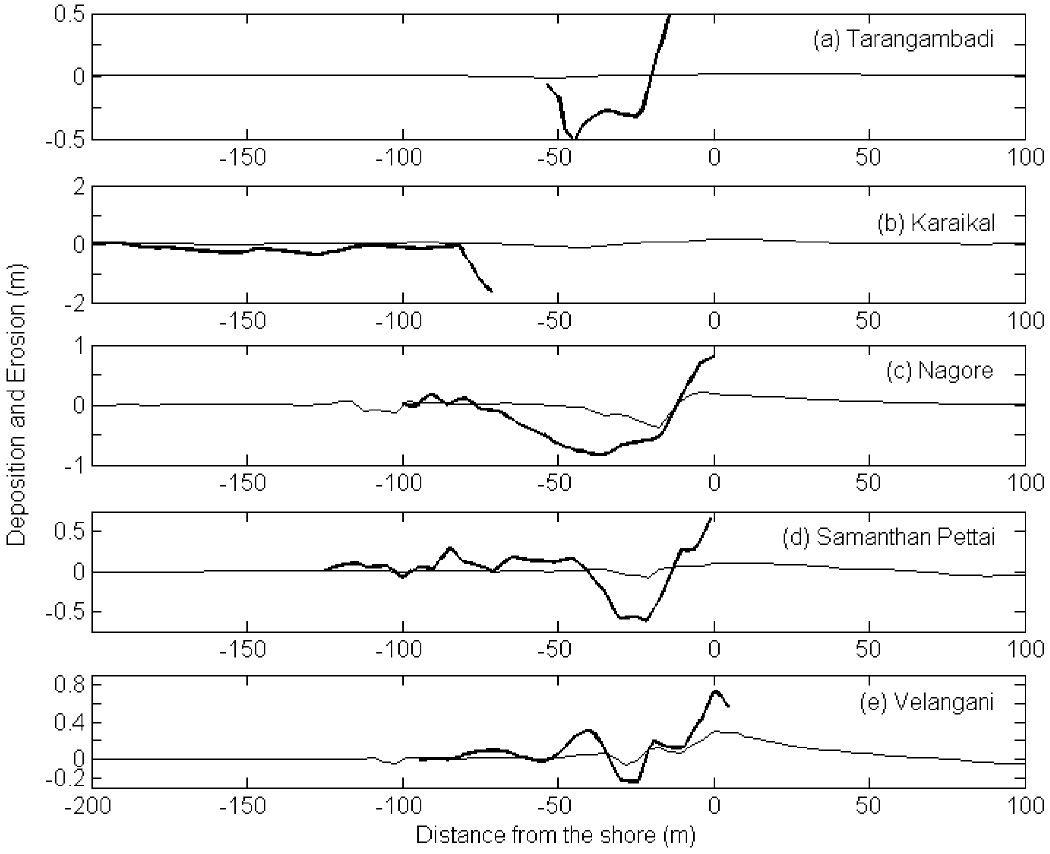

Figure 6-6. Final modelled erosion and deposition (thin line) compared with the difference on the bed profiles of January 2006 and January 2005 (thick line). The location of the profiles is shown in Figure 6-1c.

The initial and final modelled bed levels on Nagore and Samanthan Pettai are shown in Figure 6-7 with a dotted and solid thin line respectively, together with the maximum modelled water level, thin dashed-dotted line. The bed profile measured in January 2005 (here the post-tsunami bed level) is also shown for comparison with a thick solid line, as well as the measured runup with a thick dashed line. Nagore and Samanthan Pettai profiles were chosen as they were inside the region with the finest bathymetry available, nautical chart 0575A.

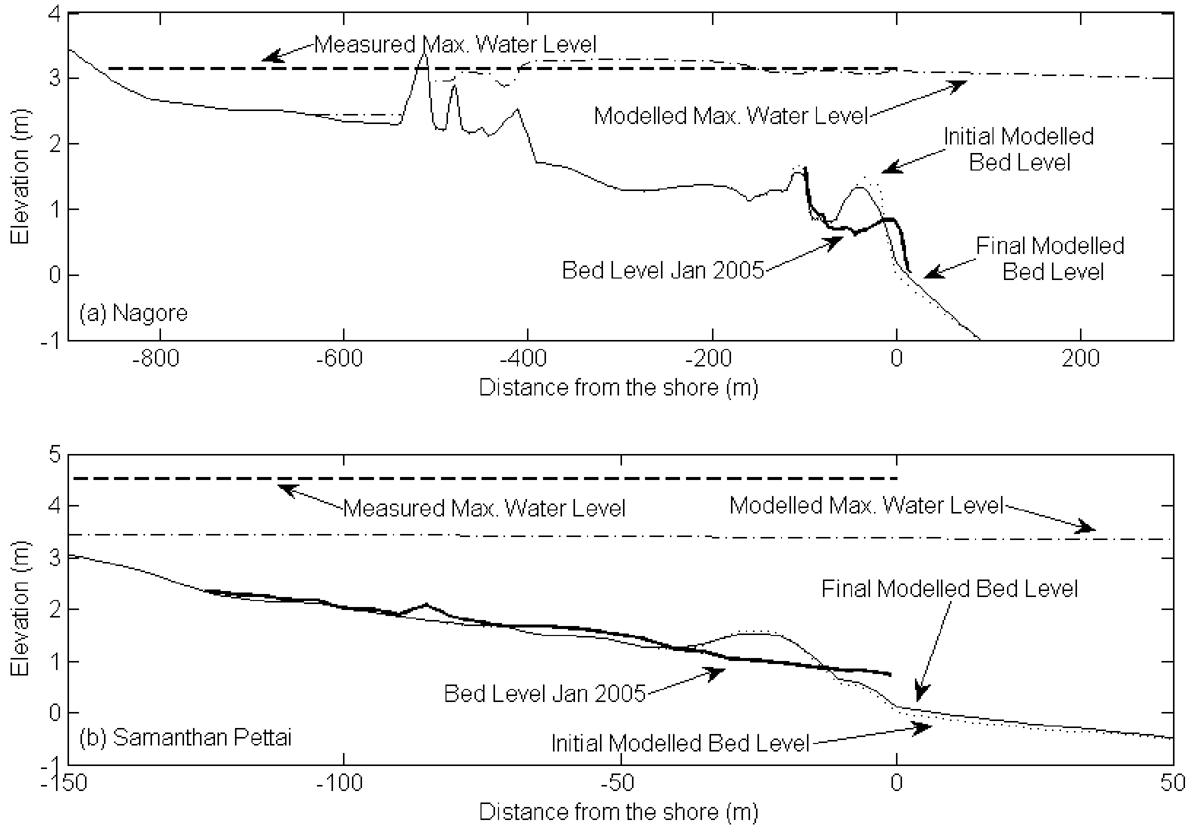

Figure 6-7. Initial bed profile (thin dotted line) and beach profile resulting from the simulation conducted here (thin line) at (a) NAGORE and (b) SAMANTHAN PETTAI. The maximum modelled water level is also shown (dashed-dotted line) together with the maximum values observed of runup and inundation (thick dashed line). The beach profile measured one month after the tsunami is also shown (thick line). The location of the profiles is shown in Figure 6-1c.

Along Nagore profile, the three-dimensional model simulated well the maximum water height (Figure 6-7a) and the distribution of the changes on the bed level caused by the tsunami (Figure 6-6c). The model simulated the erosion of the first sand dune and the deposition between the first and the second dune (Figure 6-7a). In the model results the tsunami also eroded the second dune, which possibly the 2004 tsunami did not. Yet, the three-dimensional model underestimated the large deposition caused by the tsunami on the original coastline. Along Samanthan Pettai profile, the modelling resulted on erosion of the sand dune and deposition behind the dune (Figure 6-7b). Nevertheless, the depth of this erosion and the height of this deposition were highly underestimated (Figure 6-6b).

In Figure 6-8 are shown snapshots of cross-shore velocity and sediment concentration over the vertical, together with the accumulated deposition and erosion along Nagore profile. The flow velocity was always higher on the surface than at the bottom, as tsunamis are surface waves and the bottom friction hinders the flow velocity near the bottom. At the moment of maximum inundation (Figure 6-8a-II) the horizontal velocity was zero only at the wave front, but it had non-zero offshore values everywhere else, larger over the dunes because of mass conservation. Therefore, the flow reversal had begun before the maximum inundation (Figure 6-8a-I), and did not happen at the same time for all the flow: the wave front was the last part of the flow to get to rest and only then the wave as a whole started to recede. When the wave was receding the suspended sediment concentration was larger than during the first flooding, especially near the bed (Figure 6-8cI and cII).

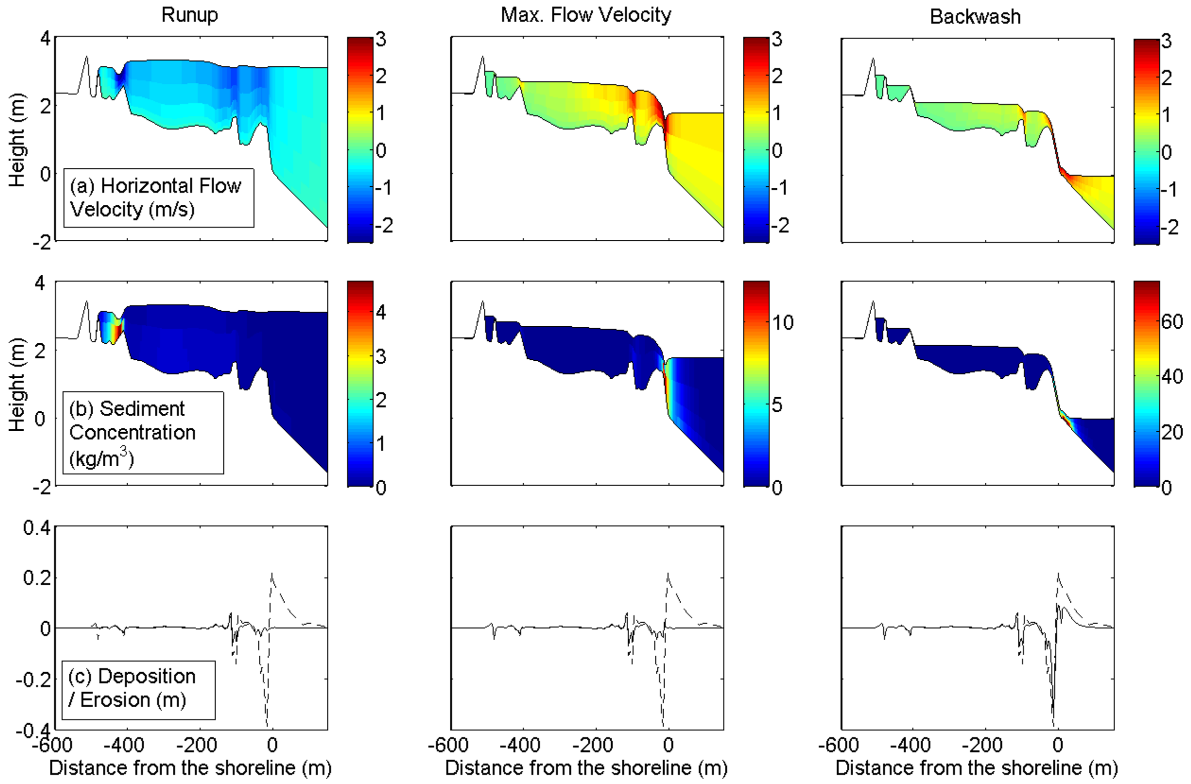

Figure 6-8. NAGORE. Snapshots of vertical variations on (a) onshore velocity and (b) sediment concentrations, and (c) snapshots of morphological changes during I. first flooding, II. maximum inundation, and III. first backwash. On (c) the instantaneous morphological changes are shown with a solid line and the final morphological changes are shown with a dashed line. The location of Nagore profile is shown in Figure 6-1c.

The high-velocity uprush flow of the tsunami in the simulation eroded the dunes and deposited a small amount of sediments behind them. The even faster backwash flow (Figure 6-8c right) eroded the dunes even more and deposited the sediments over the original shoreline, widening the beach (Figure 6-8c left and Figure 6-7). The erosion and deposition were accentuated by the flooding and ebbing of the following two tsunami waves, and the overall effect was a tendency to flatten the beach. Beach flattening was documented at the north of the study region, between Pondicherry and Portonova (VASUDEVAN et al., 2007).

6.4. Comparison between models

The modelling was repeated considering two-dimensional modelling: a depth-averaged calculation was performed to consider two-dimensional horizontal modelling (2DH) and rows of the original model were used separately to consider two-dimensional vertical modelling (2DV).

The results from the three models (3D, 2DH, 2DV) presented similar patterns of erosion and deposition along Nagore and Samanthan Pettai. Those in turn agreed with the patterns of the observations. However, in Figure 6-9 is shown that both the 2DH and the 2DV models simulated larger erosion than the 3D model, the highest corresponding to 2DV. The 2DH model calculated larger and the 2DV smaller deposition heights than the 3D model around the original shoreline. Yet, the 2DV model simulated deposit extension up to 100 – 150m offshore, which was not present with the other models; and it was not possible to verify because the beach profiles were measured only until the zero water level. On the 2DV model the flow was forced to rundown along a channel, consequently the flow took more time to decelerate, depositing the sediment over a larger extent offshore.

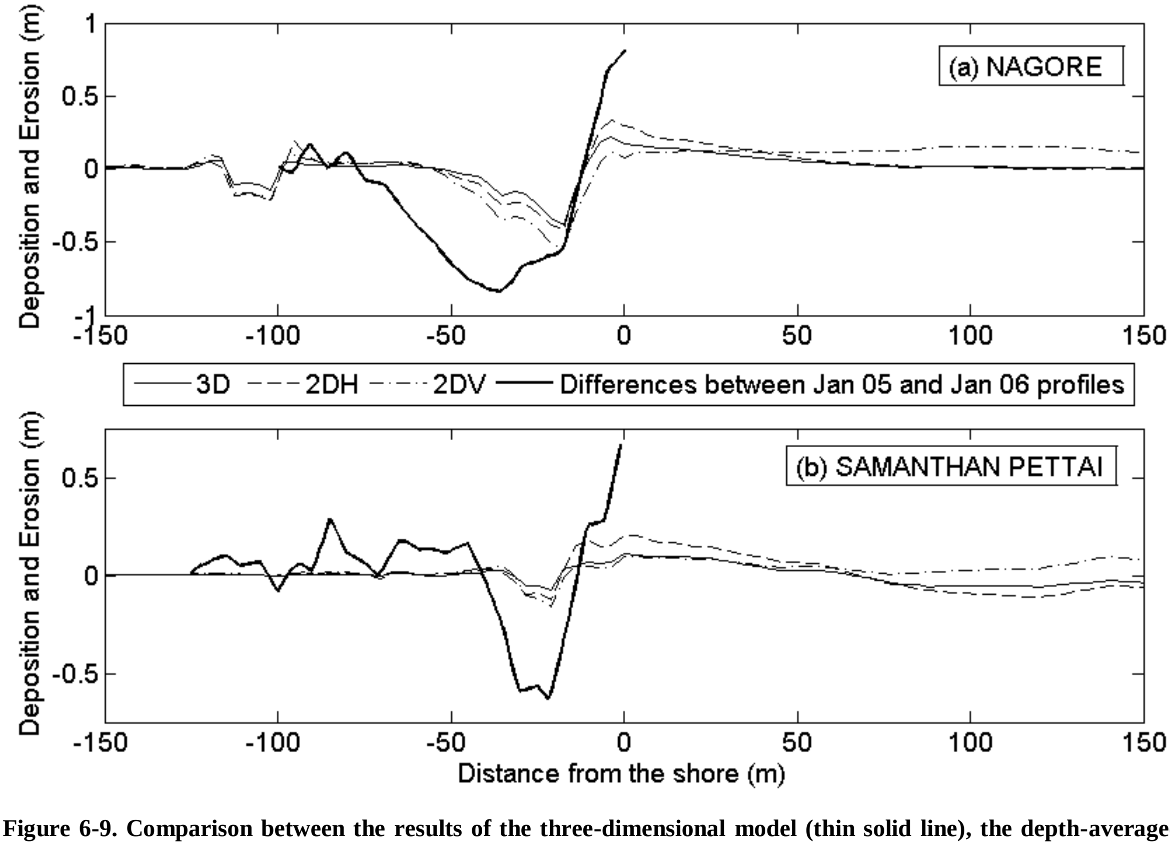

Figure 6-9. Comparison between the results of the three-dimensional model (thin solid line), the depth-averaged or two-dimensional horizontal model (dashed line), the two-dimensional vertical model (dotted-dashed line) and the

difference between the Jan 2005 and Jan 2006 measured profiles for (a) NAGORE and (b) SAMANTHAN PETTAI. The location of the profiles is shown in Figure 6-1c.

6.5. Discussion

In the third set of experiments, measured and modelled water levels showed differences in nearshore areas where tidal gauges are placed, while they did coincide more accurately in the open ocean, where the altimetry data was taken. The agreement of the computed water levels obtained here with the 2004 tsunami records, both coastal and satellite, was comparable to those of other tsunami numerical simulations such those in Fujii and Satake (2007), Arcas and Titov (2006), Geist et al. (2007), Pietrzak et al. (2007), among others. Yet, the model underestimated both inundation distance and morphological changes on the East Indian coast. The source of the discrepancies there was more likely associated with the quality of coastal bathymetry and topography data on the study region rather than with model performance. Inaccuracies on the offshore and inland bed roughness coefficient might have had a role on the mentioned discrepancies but not likely enough, as they are known to cause only minor differences on runup estimates (Section 5.3).

Over the study region it was not possible to find bathymetry on the required resolution, and interpolation had to be done, as mentioned on Section 5. The finest bathymetry available was in the neighbourhood of Nagore and Samanthan Pettai profiles, explaining the good results obtained along Nagore, but not the poorer results obtained along Samanthan Pettai. It could be possible that the bathymetry from the nautical chart and/or the SRTM topography was more accurate around Nagore than around Samanthan Pettai, differentiating the results. This nautical chart comprises data from 1991 to 2009 and then it might be also possible that the data offshore Samanthan Pettai were collected after the tsunami or many years before.

Correspondingly, there were no measurements of the beach profiles prior to the tsunami, thus the measurements of January 2006 were used as the model initial bed level, assuming the beaches had gone under full recovery by then. However this might not be true, Jaya Kumar et al. (2008) postulated that for January 2006 the beaches had reached a significant recovery although it was still in process. As every location experiences recovery at a different rhythm, it could be possible that the better results in Nagore were due to a more advanced recovery there than along Samanthan Pettai by that date. The SRTM topography did not match any of the measured profiles at any time of the year, which required the author to make adjustments to combine both sources. Moreover, during the post-tsunami survey three profiles (south, middle and north) were measured very close between them at most of the locations, but the subsequent surveys only included one profile at every location. Those locations were separated between them by more than 2km, making hard the construction of an accurate three-dimensional bathymetry and topography for the model. Furthermore, the way the beach profiles were allegedly reduced to the Chart Datum is unclear, as the same profiles in Ilangovan et al. (2005) and Jaya Kumar et al. (2008) present different reference level. The difference cannot be explained by the predicted tide at each location at the time of the surveys.

Moreover, the profiles were measured until the water level at the time of the survey which means there was no quantification of the changes caused by the tsunami offshore. According with Jaya Kumar et al. (2008) the 2004 Indian Ocean tsunami occurred at the end of the NE monsoon, when the beach width has been reduced and the sand has been deposited offshore forming sandbars. They believe the tsunami eroded these sandbars and brought the sediment to the surf zone forming the wider beaches observed right after the tsunami. The pre-tsunami bathymetry employed on the three-dimensional model did not show offshore sandbars as the ones mentioned by Jaya Kumar et al. (2008), very likely because of the resolution of the nautical charts used to build it. Therefore, in the three-dimensional modelling, the sediments responsible of the beach widening came from the sand dunes inland (Figure 6-7) being clearly less than the observations (Figure 6-6).

As tsunamis are gravity waves, unrealistic model bathymetry might have led to unrealistic flow velocities, in this case probably smaller than real flow velocities. Smaller flow velocities would lead in turn to smaller wave penetration and runup, but particularly to smaller erosion and deposition. This behaviour was observed on the experiments here, when the smaller flow velocities of tsunami waves led to smaller morphological changes than the N-waves (Figure 5-6 and Figure 5-7).

In addition to the limitations on bathymetry and topography data, there was no data available on roughness coefficient for the three-dimensional modelling region of this experiment. Then it is also possible that the underestimation of flow velocity and morphological changes on the experiments of Chapter 6 might be due to a non-realistic choice of Manning coefficient. In the experiments of Chapter 5 it was found that the variations on the flow velocity were responsible for the large differences on the erosion and deposition when the Manning's coefficient was changed. The Manning coefficient determines the amount of energy dissipated by friction, and therefore influences the flow velocity.

The three-dimensional model calculated cross-shore flow velocities up to 4m/s in Section 6 (Table 6-1 and Figure 6-5). Nonetheless, as discussed above, it is very likely that the real tsunami had even higher flow velocities, considering the underestimation of inundation distances and morphological changes (Figure 6-6 and Figure 6-7). Indeed in Chapter 5 flow velocities up to 8m/s were obtained (Figure 5-6). Tsunami flow velocities are very difficult to measure directly, but can be estimated from tsunami videos. For the 2004 Indian Ocean tsunami maximum magnitudes of flow velocities were estimated on 5m/s (FRITZ et al., 2006). Also, during the 1993 Hokkaido tsunami, the maximum flow velocity was estimated between 10 and 18m/s at Aonae, Okushiri Island, Japan (TSUTSUMI et al., 2000). And during the 2011 Tohoku event at Sendai plain in Japan, the onshore velocity of the wave-front was estimated on about 4m/s between 1 and 2km onshore of the original coastline (GOTO et al., 2011) and up to 11m/s at Kesenuma port (FRITZ et al., 2012)

In the modelling of the East Coast of India, backwash flow velocities were smaller than uprush flow velocities because the Manning coefficient onshore was almost twice than offshore and the mean bed slope was small. A larger onshore Manning coefficient meant that the flow penetrated less distance inland and then, after reversing its direction, had shorter distance to accelerate during backwash, provoking smaller backwash flow velocities. The opposite happened in the channel experiments of Chapter 5 (Figure 5-6) because the bed was even and the Manning coefficient was uniform. In the real life, when a tsunami rushes inland finds many obstacles on its way that imply a high Manning coefficient. By the time the tsunami recedes those obstacles are no longer there or represent a smaller resistance to the flow and that is another reason for tsunami backwash flows being usually faster than uprush flows.

In the India experiments, the maximum backwash flow velocity was slightly larger than the maximum uprush velocity only along Nagore profile, because the irregular bed profile there encouraged backwash flows. Also, among all profiles Nagore presented the largest backwash velocity, agreeing with the largest morphological changes along this profile. Accordingly, Tarangambadi presented the smallest backwash velocity, agreeing with the smallest morphological changes there. Backwash flows suspended more sediments than uprush flows on the experiment of Chapter 5, even if they had similar flow velocity magnitude, because backwash flows are accelerating and uprush flows are decelerating.

The smooth slope and almost even bed level along Samanthan Pettai profile caused that the flow rushed onshore very fast and returned much slower, additionally of the higher inland Manning coefficient explained before. However, caution is advised with generalizations about bed slopes, flow velocities and morphological changes. In the experiments of this Chapter the bed was not even, particularly onshore, and it is still not possible to quantify the influence of topography irregularities on the flow velocity and morphological changes (APOTSOS et al., 2009).

To the author’s knowledge, in all the modelling studies of tsunami morphodynamics, including those cited on Section 3.3 the results were not as accurate as they are in the modelling of tsunami propagation and inundation. The equations for the latter are robust and theoretical, while the sediment transport equations are empirical and based on river and estuary flows, where characteristic magnitudes are much lower than those of processes induced by tsunamis. The morphodynamic equations employed here were derived for depth-averaged velocities of less than 2m/s and sediment concentrations of less than 150kg/m^3 (VAN RIJN, 2007). In this work were obtained maximum flow velocities much larger than that and sediment concentrations up to 750kg/m^3 in Chapter 5, which were consistent with those obtained by tsunami modelling in other studies (APOTSOS et al., 2011a). The morphological changes obtained here agreed well with those obtained by Apotsos et al. (2009) and also with measurements of real tsunamis, e.g. in Sendai plain after the 2011 Japan tsunami, where the tsunami height was over 10m, and maximum scour depths of 50cm together with tsunami deposits were as thick as 30cm were measured (RICHMOND et al., 2012).

Some processes important on tsunami sediment transport are included in the model employed here, like hindered settling and suspended sediment induced density stratification (APOTSOS et al., 2011a). However, the model does not include others that are or might be important. For example, the model does not consider the interchange of fluids between the water-air or the water-sand boundaries. On the first case, the introduction of air in water happens during wave breaking, and most tsunamis do not break. On the second case, the infiltration/exfiltration flow across the fluid-sand interface and the residual pore-water pressure affect the effective stress inside the sand bed. This stress in turn affects both the effective weight of the sand particles and the boundary layer thickness. Nakamura et al. (2009) demonstrated that those effects are not negligible in predicting tsunami sediment transport.

Almost all the mentioned limitations are common to the numerical models cited in Section 3.3 when employed on tsunami sediment transport and morphological changes so far. However, the modelling studies performed up to now gave reasonably good results, allowing a general understanding of the phenomena (APOTSOS et al., 2011c), (APOTSOS et al., 2011a), (GELFENBAUM et al., 2007).

Furthermore, in this study region the incidence angle of the tsunami was estimated on about 240° (NE to SW) by Bhattacharya (2005) based on the orientation of felled vegetation. This was also approximately the incidence direction of the tsunami in the model, observed on tsunami animation. As the shoreline is orientated mainly from north to south, a 240° incidence angle means that the alongshore component of the flow was stronger than the cross-shore component. This was the reason for the 2DV model presenting larger morphological changes than the 3D model, because considers all the flow impacting perpendicularly to the shoreline, instead of obliquely as it was in reality. Equally, the 2DH model considers the alongshore components of velocity and transport, but employs the depth-averaged values of these variables. As depth-averaged velocities are larger than bottom velocities, is expectable that 2DH presented also larger morphological changes than the 3D model. However, due to the differences on prescribing the bottom friction and turbulence closure model between the 2DH model and those considering variations over the vertical direction, the comparison of 2DH with 3D and 2DV might not be appropriate. Three-dimensional modelling is preferable as it incorporates effects of wave incidence and velocity profiles, being more physically accurate than depth-averaged or 2DV models.

Still, there is a slight possibility that the employment of a 3D model is not justifiable for tsunami morphodynamics, in the similar way as Boussinesq equations are not chosen to model tsunami flow. As discussed in Section 2.3, Boussinesq equations are more appropriate to describe tsunamis than Shallow Water Equations because they consider wave dispersion. However, the former are much more expensive computationally than the latter, and wave dispersion can be approximated by numerical dispersion, making SWE widely preferred for tsunami simulations. In the case of morphodynamical modelling there are still many uncertainties and assumptions, some of which were listed above, that might turn pointless the employment of a three-dimensional model. After all, the results of both models agree qualitatively between them and with the few data available, and then the results of a depth-averaged model might be interpreted as an extreme value, instead of an accurate prediction. Anyway, more studies would be necessary to inquire this.

Summarizing, with the equations currently available, it would be desirable to have pre-tsunami existing conditions over a region and not only over several disperse profiles when modelling tsunami caused morphological changes. These conditions should include at least: bathymetry, topography, bed roughness, sediment size, composition, and distribution. Unfortunately, these data are also very difficult to collect because it is not possible to know when a tsunami will happen and coasts are under continuous change. The constant monitoring of the mentioned parameters over a region would be the only way to have pre-tsunami updated data. This kind of monitoring is usually performed in harbours or semi-closed coastal environments where tsunami behaviour and consequences are very different than in open coastlines like the one modelled here (TAKAHASHI et al., 2000), (NISHIHATA et al., 2006), (KIHARA and MATSUYAMA, 2010). Still, the agreement obtained in this work between the three-dimensional model results and the data available was comparable to that obtained in morphodynamic simulations of tsunamis by Apotsos et al. (2011a), (2011c), Li et al. (2012), Kihara and Matsuyama (2010) among others.

7. Conclusions and Recommendations

Here the results of three different set of experiments were presented: one modelled only tsunami hydrodynamics and two modelled also morphodynamics in the searching of a modelling strategy for tsunami morphological changes. On the first set of experiments several tsunami scenarios for the North Sea were considered by means of N-waves, including the search of the origin of the orphan 1858 tsunami. Tsunami simulations performed at the North Sea resulted on water levels smaller than those from storm surges, when a wave of unitary height was imposed. However, modelled tsunami flow velocities suggest that a large tsunami might cause equal o larger damage than storm surges on the region, due to comparable magnitude of flow velocities and smaller time of action. Part of this damage would consist on erosion and sediment deposition, which was not simulated at the North Sea as there was no data to compare or validate the modelling.

The type of tsunami source was found to play an important role determining the most affected regions. Submarine slides-generated tsunamis and earthquake-generated tsunamis differ not only in their characteristic amplitudes but also in frequency and shape. Those differences were remarkable as the Storegga-like tsunami and an earthquake generated tsunami imposed in the same way affected different regions in the German Bight and the North Sea.

N-waves have been proved to be a good representation of the leading wave of tsunamis when modelling tsunami heights and can be employed on studies like the one performed here on the North Sea. However, they do not seem to work as well on modelling tsunami morphodynamics, according with the results of the second set of experiments.

On the second set of experiments, N-waves were employed as an attempt to parameterize the tsunami caused morphological changes along two-dimensional vertical channel. The morphodynamics of leading elevation and leading depression N-waves were analysed and compared with the morphodynamics of equivalent real tsunami shapes, which were normalized to equal maximum wave height.

Nevertheless, the employment of N-waves to simulate tsunami morphodynamics was not straightforward on the experiments performed here. It does not seem possible to use them within the modelling strategy as it was required more specific information about the tsunami shape to model tsunami morphological changes than to model tsunami water levels.

On the third set of experiments, a three-dimensional model was set up to simulate the morphological changes caused on the East Coast of India by a tsunami with similar characteristics as the 2004 Indian Ocean tsunami. The three-dimensional model utilized performed satisfactorily despite the simplifications employed and the little data available. The overall results compared qualitatively well with the observed effects of the 2004 Indian Ocean tsunami in this region. The model also approximated quantitatively the morphological changes caused along Nagore profile. Nevertheless, it underestimated the morphological changes along Samanthan Pettai and Velangani profiles in the south, and did not reproduce well the morphological changes along Tarangambadi and Karaikal profiles in the north. Along the study region consisting of an open coastline, the overall effect of the tsunami was flattening the beach, both on the three-dimensional modelling results and on post-tsunami observations.

As part of the strategy of modelling coastal development due to tsunamis, it is desirable to have accurate and fine-resolution data to perform more reliable tsunami modelling. The quality of the data on bathymetry, topography and tsunami source is important in any tsunami modelling. Moreover when sediment transport is also modelled, it is important to have also accurate data on pre-tsunami existing conditions such as topography, bathymetry, sediment size, composition and distribution. Records of tsunamis which caused morphological changes often consist only of inland sediment deposits and no reference is given to offshore deposits or erosion in general. In the results presented here, waves caused both erosion and deposition offshore; therefore the tsunami surveys should ideally be extended to include determining factors such as the offshore morphological changes.

Until now there are no sediment transport formulations derived and/or validated specifically for tsunami flow conditions. However, the formulation employed here gave satisfactory results, not only qualitatively but also quantitatively considering the many approximations employed. Despite the mentioned limitations, the numerical modelling of tsunami morphodynamics can be employed to understand better the consequences of tsunamis on a mobile bed. Further research could confirm or reject the adequacy of this sediment transport formulation on tsunami cases and add processes not accounted for so far to improve the strategy.

Even when Delft3D has been validated for tsunami propagation and inundation, there are still no benchmarks for the modelling of tsunami currents and therefore it is not possible to know how well is it or any numerical model performing on the simulation of tsunami flow velocities. However, as mentioned in Section 2.12, this kind of benchmarks might be available soon and then it is advisable to validate the numerical model for the modelling of tsunami currents.

On the last experiment, the comparison between results of 3D, 2DV and 2DH models proved that there were significant differences when simplifications were made in order to use 2D models rather than 3D. As the angle of incidence of the tsunami wave and the flow velocity distribution over the water column are important on the numerical modelling, 3D models seem to be the best choice. However, there are so many uncertainties on the modelling of tsunami morphodynamics that the employment of 3D models might be futile. The determination of the best model might not be possible until specific equations for tsunami sediment transport are derived or the adequacy of the existent demonstrated.

8. Bibliography

ALLEN, J. R. L. 1992. *Principles of Physical Sedimentology*. 272pp.; New Jersey (The Blackburn Press).

APOTSOS, A., M. BUCKLEY, J. GELFENBAUM, B. JAFFE, and D. VATVANI. 2011a. Nearshore tsunami inundation model validation: towards sediment transport applications. *Pure and Applied Geophysics*. **168**(11): 2097-2119, doi10.1007/s00024-011-0291-5.

APOTSOS, A., G. GELFENBAUM, and B. JAFFE. 2011b. Process-based modeling of tsunami inundation and sediment transport. *Journal of Geophysical Research - Earth Surface*. **116**(F1): p.F01006, doi10.1029/2010JF001797.

APOTSOS, A., G. GELFENBAUM, B. JAFFE, S. WATT, B. PECK, M. BUCKLEY, and A. STEVENS. 2011c. Tsunami Inundation and Sediment Transport in a Sediment-Limited Embayment on American Samoa. *Earth Science Reviews*. **107**(1-2): 1-11, doi10.1016/j.earscirev.2010.11.001.

APOTSOS, A., B. JAFFE, and G. GELFENBAUM. 2011d. Wave characteristic and morphologic effect on the onshore hydrodynamic response of tsunamis. *Coastal Engineering*. **58**: 1034-1048, doi10.1016/j.coastaleng.2011.06.002.

APOTSOS, A., B. JAFFE, G. GELFENBAUM, and E. ELIAS. 2009. Modeling time-varying tsunami sediment deposition. *In*: *Proceedings of Coastal Dynamics 2009*. Tokyo, p.Paper No. 34. doi:10.1145/9789814282475_0037.

APOTSOS, A., B. JAFFE, G. GELFENBAUM, and E. ELIAS. 2009. Modeling time-varying tsunami sediment deposition. *In*: *Proceedings of Coastal Dynamics 2009*. Tokyo.

ARCAS, D. and V. TITOV. 2006. Sumatra tsunami: lessons from modeling. *Survey in Geophysics*. **27**: 679-705.

Asian Tsunami Videos. 2011. [online]. [Accessed 31 January 2012]. <http://www.asiantsunamivideos.com/>

BHATTACHARYA, G.C., D. ILANGOVAN, S. JAYAKUMAR, R. MANIMURALI, M. KOCHERLA, R. ALAGARSAMY, R. GOWTHAMAN, and K.A. NAIK. 2005. *Observations of post tsunami reconnaissance investigations along eastern coastal tract of*

India following the devastating tsunami of 26th December 2004. National Institute of Oceanography of India.

BORCK, I., S. DICK, E. KLEINE, and E. MÜLLER-NAVARRA. 2007. *Tsunami - a study regarding North Sea coast*. Hamburg and Rostock.

BOURGEOIS, J. 2009. Geological Effects and Records of Tsunamis. *In*: E. N. BERNARD and A. R. ROBINSON, (eds). *The Sea. Tsunamis*, Cambridge, MA: Harvard University Press.

BRETSCHNEIDER, C. L. and P.G. WYBRO. 1976. Tsunami Inundation Prediction. *In*: *Proceedings of the 15th Conference on Coastal Engineering*., pp.1006-1024.

BRICKER, J. D., S. MUNGER, C. PEQUIGNET, J. R. WELLS, G. PAWLAK, and K. F. CHEUNG. 2007. ADCP observations of edge waves off Oahu in the wake of November 2006 Kuril Islands tsunami. *Geophysical Research Letters*. **34**(L23617), doi10.1029/2007GL032015.

BRUSS, G., G. GÖNNERT, and R. MAYERLE. 2010. Extreme scenarios at the German North Sea Coast. A numerical model study. *In*: *Coastal Engineering*. Shangai, China.

CARRIER, G. F., T. T. WU, and H. YEH. 2003. Tsunami run-up and draw-down on a plane beach. *Journal of Fluid Mechanics*. **475**: 79-99.

CHACÓN-BARRANTES, S. 2005. *Estimación temprana de la altura esperada de tsunamis*.; Ensenada, Mexico (Master's Thesis).

CHACÓN-BARRANTES, S. 2007a. Factores que influyen la forma de un tsunami. *Revista Uniciencia*.

CHACÓN-BARRANTES, S. 2007b. Importancia de la batimetría de las planicies abisales en la propagación de tsunamis transoceánicos (in spanish). *Ciencia y Tecnología*. **25**(1-2): 25-33.

CLAGUE, J. J., P. T. BOBROWSKI, and I. HUTCHINSON. 2000. A review of Geological records of large tsunamis at Vancouver Island, British Columbia, and implications for hazard. *Quaternary Science Reviews*. **19**: 849-863.

CUSHMAN-ROISIN, B. and J. M. BECKERS. 2011. *Introduction to Geophysical Fluid Dynamics*. Academic Press.

DAO, M. H. and P. TKALICH. 2007. Tsunami propagation modelling - a sensitivity study. *Natural Hazards and Earth System Sciences*. **7**: 741-754, doi10.5194/nhess-7-741-2007.

DAWSON, A. G. 1996. The geological significance of tsunamis. *Zeitschrift für Geomorphologie*. **102**: 199-210.

DAWSON, A.G. 1999. Linking tsunami deposits, submarine slides and offshore earthquakes. *Quaternary International*. **60**: 119-126.

DAWSON, A. G., D. LONG, and D. E. SMITH. 1988. The Storegga slides: evidence from eastern Scotland for a possible tsunami. *Marine Geology*. **82**(2): 272-276, doi10.1016/0025-3227(88)90146-6.

DAWSON, A.G. and I. STEWART. 2007. Tsunami deposits in the geological record. *Sedimentary Geology*. **200**: 166-183, doi10.1016/j.sedgeo.2007.01.002.

DELEERSNIJDER, E. and P. LUYTEN. 1994. On the practical advantages of the quasi-equilibrium version of the Mellor and Yamada level 2.5 turbulence closure applied to marine modelling. *App. Math. Modelling*. **18**(5): 281-287.

DELFT HYDRAULICS. 2010. *Delft3D-FLOW, User Manual*. Delft (Deltares).

DENGLER, L. and B. USLU. 2011. Effects of Harbor Modification on Crescent City, California's Tsunami Vulnerability. *Pure and Applied Geophysics*. **168**(6-7): 1175-1185, doi10.1004/s00024-010-0224-8.

EINSELE, G., S.K. CHOUGH, and T. SHIKI. 1996. Depositional events and their records - an introduction. *Sedimentary Geology*. **104**: 1-9, doi10.1016/0037-0738(95)00117-4.

FRITZ, H., J. BORRERO, C. E. SYNOLAKIS, and J. YOO. 2006. 2004 Indian Ocean tsunami flow velocity measurements from survivor videos. *Geophysical Research Letters*. **33**(24): p.L24605, doi10.1029/2006GL026784.

FRITZ, H., D. PHILLIPS, A. OKAYASU, T. SHIMOZONO, H. LIU, F. MOHAMMED, V. SKANAVIS, C. E. SYNOLAKIS, and T. TAKAHASHI. 2012. The 2011 Japan tsunami current velocity measurements from survivor videos at Kesenuma Bay using LiDAR. *Geophysical Research Letters*. **39**(7), doi10.1019/2011GL050686.

FUJII, Y. and K. SATAKE. 2007. Tsunami source of the 2004 Sumatra-Andaman Earthquake Inferred from Tide Gauge and Satellite Data. *Bulletin of the Seismological Society of America*. **97**(1A): S192-S207.

GAYER, G., I. LESCHKA, I. NÖHREN, O. LARSEN, and H. GÜNTER. 2010. Tsunami inundation modelling based on detailed roughness maps of densely populated areas. *Natural Hazards and Earth System Science*. **10**(8): 1679-1687, doi10.5194/nhess-10-1679-2010.

GEBCO. 2011. *General Bathymetry Chart of the Oceans*. [online]. <http://www.gebco.net/>

GEIST, E. L., V. V. TITOV, D. R. ARCAS, F. F. POLLITZ, and S. L. BILEK. 2007. I. Implications of the December 26, 2004 Sumatra-Andaman earthquake on tsunami forecast and assesment models for great subduction zone earthquakes. *Bull. Seismol. Soc. America*. **97**(1A): S240-S270, doi10.1785/0120050619.

GELFENBAUM, G., D. VATVANI, B. JAFFE, and F. DEKKER. 2007. Tsunami inundation and sediment transport in vicinity of coastal mangrove forest. *In*: *Coastal Sediments 2007*. New Orleans: American Society of Civil Engineers (ASCE), pp.1117-1128.

GOFF, J. R., H. L. ROUSE, S. L. JONES, B. W. HAYWARD, U. COCHRAN, W. MCLEA, W. W. DICKINSON, and M. S. MORLEY. 2000. Evidence for an earthquake and tsunami about 3100-3400 yr ago, and other catastrophic saltwater inundations recorded in coastal lagoon, New Zealand. *Marine Geology*. **170**: 213-249.

GOTO, K., C. CHAGUÉ-GOFF, S. FUJINO, J. GOFF, B. JAFFE, Y. NISHIMURA, B. RICHMOND, D. SUGAWARA, W. SZCZUCINSKI, D. R. TAPPIN, R. C. WITTER, and E. YULIANTO. 2011. New insights of tsunami hazard from the 2011 Tohoku-oki event. *Marine Geology*. **290**(1-4): 46-50, doi10.1016/j.margeo.2011.10.004.

GOTO, C., Y. OGAWA, and F. IMAMURA. 1997. *Numerical Method of Tsunami Simulation with the Leap-Frog Scheme*. Intergovernmental Oceanographi Commision, Manuals & Guides 35.

GUSMAN, A., Y. TANIOKA, B. MACINNES, and H. TSUSHIMA. 2014. A methodology for near-field tsunami inundation forecasting: Application to the 2011 Tohoku tsunami. *Journal of Geophysical Research: Solid Earth*. **119**: 1-21, doi10.1002/2014JB010958.

HARBITZ, C. B. 1992. Model simulations of tsunamis generated by the Storegga Slides. *Marine Geology*. **105**: 1-21.

HARTSUIKER, G. 1997. *Deutsche Bucht and Dirthmarscher Bucht, Set-up and Calibration of Tidal Flow Models*. Delft.

HORSBURGH, K. J., C. WILSON, B. J. BAPTIE, A. COOPER, D. CRESSWELL, R.M. W. MUSSON, L. OTTEMÖLLER, S. RICHARDSON, and S. L. SARGEANT. 2008. Impact of a Lisbon-type tsunami on the U.K. coastline and the implications for tsunami propagation over broad continental shelves. *Journal of Geophysical Research*. **113**: p.C04007, doi10.1029/2007JC004425.

HUNTINGTON, K., J. BOURGEOIS, G. GELFENBAUM, P. LYNETT, B. JAFFE, H. YEH, and R. WEISS. 2007. Sandy signs of tsunami onshore depth and speed. *EOS Trans. Am. Geophys. Union*. **88**(52): 577-578.

ILANGOVAN, D., S. JAYAKUMAR, R. GOWTHAMAN, G. TIRODKAR, P. GANESAN, G.N. NAIK, R. MANIMURALI, G.S. MICHAEL, M.V. RAMANA, and K.A. NAIK. 2005. *Inundation, run-up heights, cross-section profiles and littoral environment along the Tamil Nadu coast after 26th December 2004 Tsunami*. Goa (National Insitute of Oceanography of India).

IMAMURA, F. 2009. Tsunami Modeling: Calculating Inundation and Hazard Maps. *In*: E. BERNARD and A. ROBINSON, (eds). *Tsunamis. The Sea V. 15*, Harvard University Press, pp.321-332.

IMAMURA, F., A. YALCINER, and G. OZYURT. 2006. *Tsunami modelling manual (TUNAMI model).*

IOC. 2013. *Tsunami Glossary*. Paris (UNESCO).

JAFFE, B. E. and G. GELFENBAUM. 2007. A simple model for calculating tsunami flow speed from tsunami deposits. *Sedimentary Geology*. **200**: 347-361, doi10.1016/j.sedgeo.2077.01.013.

JAYA KUMAR, S., K. A. NAIK, M. V. RAMANAMURTHY, D. ILANGOVAN, R. GOWTHAMAN, and B. K. JENA. 2008. Post-tsunami changes in the littoral environment along the southeast coast of India. *Journal of Environmental Management*. **89**: 35-44, doi10.1016/j.jenvman.2007.01.050.

KAWATA, Y., H. HAYASI, F. IMAMURA, S. KOSHIMURA, K. SATAKE, Y. TSUJI, K. FUJIMA, I. HAYASI, H. MATSUTOMI, T. TAKAHASHI, Y. TANIOKA, Y. NISHIMURA, M. MATSUYAMA, N. MAKI, K. HORIE, N. KOIKE, K. HARADA, and S. SUZUKI. 2012. *The December 26, 2004 Earthquake Tsunami Disaster of Indian Ocean*. [online]. <http://www.drs.dpri.kyoto-u.ac.jp/sumatra/index-e.html#tsunami>

KENCH, P. S., S. L. NICHOL, S. G. SMITHERS, R. F. MCLEAN, and R. W. BRANDER. 2008. Tsunami as agent of geomorphic change in mid-ocean reef islands. *Geomorphology*. **95**: 361-383, doi10.1016/j.geomorph.2007.06.012.

KIHARA, N., N. FUJII, and M. MATSUYAMA. 2012. Three-dimensional sediment transport processes on tsunami-induced topography changes in a harbor. *Earth Planets Space*. **64**: 787-797, doi10.5047/eps.2011.05.036.

KIHARA, N. and M. MATSUYAMA. 2010. Numerical Simulations of Sediment Transport Induced by the 2004 Indian Ocean Tsunami near Kirinda Port in Sri Lanka. *In*: *Proc. of the International Conference in Coastal Engineering*. Shangai, p.currents.12.

KOWALIK, Z. and A. PROSHUTINSKY. 2010. Tsunami-tide interactions: a Cook Inlet case study. *Continental shelf research*. **30**: 633-642, doi10.1016/j.csr.2009.10.004.

KOWALIK, Z., T. PROSHUTINSKY, and A. PROSHUTINSKY. 2006. Tide-tsunami interactions. *Science of Tsunami Hazards*. **24**(4): 242-256.

LACY, J., D. RUBIN, and D. BUSCOMBE. 2012. Currents, drag and sediment transport induced by a tsunami. *Journal of Geophysical Research*. **117**(C9): p.C09028, doi10.1029/2012JC007954.

LE ROUX, J.P. and G. VARGAS. 2005. Hydraulic behaviour of tsunami backflows: insights from their modern and ancient deposits. *Environmental Geology*. **49**(1): 65-75, doi10.1007/s00254-005-0059-2.

LEENDERTSE, J. J. 1987. *A three-dimensional alternating direction implicit model with iterative fourth-order dissipative non-linear advection terms*. Amsterdam (The Netherlands Rijkswaterstaat WD-333-NETH).

LEHFELDT, R., P. MILBRADT, A. PLÜSS, and H. SCHÜTTRUMPF. 2007. Propagation of a Tsunami-Wave in the North Sea. *Die Küste*. **72**: 105-123.

LEVIN, B. and M. NOSOV. 2009. *Physics of Tsunamis*. 327pp.; Moscow (Springer).

LI, L., Q. QIU, and H. ZHENHUA. 2012. Numerical modeling of the morphological change in Lhok Nga, west Banda Aceh, during the 2004 Indian Ocean tsunami: understanding tsunami deposits using a forward modeling method. *Natural Hazards*. **64**: 1549-1574, doi10.1007/s11069-012-0325-z.

LIU, P. L.-F., Y.-S. CHO, M. J. BRIGGS, U. KANOGLU, and C. E. SYNOLAKIS. 1995. Runup of solitary waves on a circular island. *Journal of Fluid Mechanics*. **302**: 259-285, doi10.1017/S0022112095004095.

LYNETT, P. J., J. C. BORRERO, R. WEISS, S. SON, D. GREER, and W. RENTERIA. 2012. Observations and modeling of tsunami-induced currents in ports and harbors. *Earth and Planetary Science Letters*. **327-328**: 68-74, doi10.1016/j.epsl.2012.02.002.

LYNETT, P. J., T. R. WU, and P. L.-F. LIU. 2002. Modeling Wave Runup with Depth-Integrated Equations. *Coastal Engineering*. **46**(2): 89-107, doi10.1016/S0378-3839(02)00043-1.

MADSEN, P. and H. SCHÄFFER. 2010. Analytical solutions for tsunami runup on a plane beach: single waves, N-waves and transient waves. *Journal of Fluid Mechanics*. **645**: p.27, doi10.1017/S0022112009992485.

MARTIN, M.E., R. WEISS, J. BOURGEOIS, T. PINEGINA, H. HOUSTON, and V. TITOV. 2008. Combining constraints from tsunami modeling and sedimentology to untangle the 1969 Ozernoi and 1971 Kamchatskii tsunamis. *Geophysical Research Letters*. **35**: p.L01610, doi10.1029/2007GL032349.

MASCARENHAS, A. and S. JAYAKUMAR. 2008. An environmental perspective of the post-tsunami scenario along the coast of Tamil Nadu, India: Role of sand dunes and forests. *Journal of Environmental Management*. **89**: 24-34, doi10.1016/j.jenvman.2007.01.053.

MAYERLE, R., J. WILKENS, C. ESCOBER, and W. WINDUPRANATA. 2005. Hydrodynamic Forcing Along the Open Sea Boundaries of Small-Scale Coastal Models. *Die Küste. Archive for research and technology on the North Sea and Baltic Coast*. **69**: 203-228.

MERCADO, A. and W. MCCANN. 1998. Numerical simulation of the 1918 Puerto Rico tsunami. *Natural Hazards*. **18**(1): 57-76.

MOREIRA, V. S. 1989. Seismicity of the Portuguese continental margin. *In*: S. GREGERSEN and P. W. BASHAM, (eds). *Earthquakes at North Atlantic Passive Margins Neotectonic and Postglacial Rebound*, Massachusetts: Kluwer, p.736.

MURTY, T. S. and Z. KOWALIK. 1993. Use of Boussinesq versus Shallow Water Equations in tsunami calculations. *Marine Geodesy*. **16**(2): 149-151.

NAGARAJAN, B., I. SURESH, D. SUNDAR, R. SHARMA, A. K. LAL, S. NEETU, S. S. C. SHENOI, and D. SHANKAR. 2006. The great tsunami of 26 December 2004: A description based on tide gauge data from Indian subcontinent and surrounding areas. *Earth Planets Space*. **58**: 211-215.

NAKAMURA, T., N. MIZUTANI, and S. YIM. 2009. A three-dimensional coupled Fluid-Sediment Interaction Model with Bed-Load/Suspended-Load Transport for Scour Analysis Around a Fixed Structure. *Journal of Offshore Mechanics and Artic Engineering*. **131**: p.031104, doi10.1115/1.3124132.

NEWIG, J. 2012. *Personal Communication*.

NEWIG, J. and D. KELLETAT. 2011. The North Sea tsunami of June 5, 1858. *Journal of Coastal Research*. **27**(5): 931-941, doi10.2112/JCOASTRES-D-10-00098.1.

NGDC. 2012. *Tsunami Travel Time Maps*. [online]. [Accessed 2012]. <http://www.ngdc.noaa.gov/hazard/tsu_travel_time.shtml>

NGDC/WDC, National Geophysical Data Center / World Data Center. 2011. *Global Historical Tsunami Database*. [online]. <http://www.ngdc.noaa.gov/hazard/tsu_db.shtml>

NISHIHATA, T., Y. TAJIMA, Y. MORIYA, and T. SEKIMOTO. 2006. Topography change due to the Dec 2004 Indian Ocean tsunami - field and numerical study at Kirinda Port, Sri Lanka -. *In*: *Proc. of the 30th International Conference in Coastal Engineering*. ASCE, pp.1456-1468.

NOAA/PMEL. 2009. *December 26, 2004 Indonesian Sumatra Earthquake*. [online]. [Accessed 29 Oct 2014]. <http://nctr.pmel.noaa.gov/sumatra20041226.html>

NOAA/PMEL. 2011. *NOAA Center of Tsunami Research. Tsunami Event - December 26, 2004 Indonesia (Sumatra)*. [online]. <http://nctr.pmel.noaa.gov/indo_1204.html>

ONTOWIRJO, B., R. PARIS, and A. MANO. 2013. Modeling of coastal erosion and sediment deposition during the 2004 Indian Ocean tsunami in Lhok Nga, Sumatra, Indonesia. *Natural Hazards*. **65**(3): 1967-1979, doi10.1007/s11069-012-0455-3.

PARI, Y., M.V. RAMANA MURTHY, S. JAYA KUMAR, B.R. SUBRAMANIAN, and S. RAMACHANDRAN. 2008. Morphological changes at Vellar estuary, India - Impact of the December 2004 tsunami. *Journal of Enviromental Management*. **89**: 45-57, doi10.1016/j.jenvman.2007.01.055.

PHILLIPS, N. A. 1957. A co-ordinate system having some special advantages for numerical forecasting. *Journal of Meteorology*. **14**: 184-185.

PIETRZAK, J., A. SOCQUET, D. HAM, W. SIMONS, C. VIGNY, R. J. LABEUR, E. SCHRAMA, G. STELLING, and D. VATVANI. 2007. Defining the source region of the Indian Ocean tsunami from GPS, altimeters, tide gauges and tsunami models. *Earth and Planetary Science Letters*. **261**: 49-64.

PMEL. 2006. *Method of Splitting Tsunami (MOST) Software Manual*. NOAA.

PRITCHARD, D. and L. DICKINSON. 2008. Modelling the sedimentary signature of long waves on coasts: implications for tsunami reconstruction. *Sedimentary Geology*. **206**: 42-57, doi10.1016/j.sedgeo.2008.03.004.

REID, H. F. 1914. The Lisbon earthquake of November 1 1755. *Bull. Seismological Society of America*. **4**: 53-80.

RICHMOND, B., W. SCZSUCINSKI, C. CHAGUÉ-GOFF, K. GOTO, D. SUGAWARA, R. C. WITTER, D. R. TAPIN, B. E. JAFFE, S. FUJINO, Y. NISHIMURA, and J. GOFF. 2012. Erosion, deposition and landscape change on the Sendai coastal plain, Japan, resulting from the March 11, 2011 Tohoku-oki tsunami. *Sedimentary Geology*. **282**: 27-39, doi10.1016/j.sedgeo.2012.08.005.

SATAKE, K. 1995. Linear and nonlinear computations of the 1992 Nicaragua earthquake tsunami. *Pure and Applied Geophysics PAGEOPH*. **144**(3-4): 455-470, doi10.1007/BF00874378.

SMITH, D. E., S. SHI, R. A. CULLINGFORD, A. G. DAWSON, S. DAWSON, C. R. FIRTH, I. D. L. FOSTER, P. T. FRETWALL, B. A. HAGGART, L. K. HOLLOWAY, and D. LONG. 2004. The Holocene Storegga Slide tsunami in the United Kingdom. *Quaternary Science Reviews*. **23**: 2291-2321, doi10.1016/j.quascirev.2004.04.001.

SRINIVASALU, S., N. THANGADURAI, A. D. SWITZER, V. RAM MOHAN, and T. AYYAMPERUMAL. 2007. Erosion and sedimentation in Kalpakkam (N Tamil Nadu, India) form the 26th December 2004 tsunami. *Marine Geology*. **240**: 65-75, doi10.1016/j.margeo.2007.02.003.

SRTM. 2011. *Shuttle Radar Topography Mission*. [online]. <http://www2.jpl.nasa.gov/srtm/index.html>

STELLING, G. S. and S. P.A. DUINMEIJER. 2003. A staggered conservative scheme for every Froude number in rapidly varying shallow water flows. *Intl. J. Numerical Methods in Fluids*. **43**(12): 1329-1354.

STELLING, G. S. and J. J. LEENDERTSE. 1991. Approximation of convective processes by cyclic AOI methods. *In*: *Proceedings of the 2nd ASCE Conference on Estuarine and Coastal Modeling*. Tampa: ASCE, pp.771-782.

SUGAWARA, D., K. MINOURA, and F. IMAMURA. 2008. Tsunamis and Tsunami Sedimentology. *In*: T. SHIKI, Y. TSUJI, T. YAMAZAKI, and K. MINOURA, (eds). *Tsunamiites: Features and Implications*, Elsevier, p.426.

SYNOLAKIS, C., E. BERNARD, V. TITOV, U. KANOGLU, and F. GONZÁLEZ. 2007. *Standards, Criteria and Procedures for NOAA Evaluation of Tsunami Numerical Models*. Seattle.

SYNOLAKIS, C. E., E. N. BERNARD, V. V. TITOV, U. KANOGLU, and F. I. GONZALEZ. 2008. Validation and Verification of Tsunami Numerical Models. *Pure and Applied Geophysics*. **165**: 2197-2228.

TADEPALLI, S. and C. E. SYNOLAKIS. 1994. The runup of N-waves on sloping beaches. *Proc. R. Soc. Lond. A.* **445**: 99-112.

TADEPALLI, S. and C.E. SYNOLAKIS. 1996. Model for the leading waves of tsunamis. *Physical Review Letters*. **77**(10): 2141-2144.

TAKAHASHI, T., N. SHUTO, F. IMAMURA, and D. ASAI. 2000. Modeling sediment transport due to tsunamis with exchange rate between bed load layer and suspended load layer. *In*: *Proc. of the 27th International Conference in Coastal Engineering*., pp.1508-1519.

TITOV, V., F. GONZÁLEZ, H. MOJFELD, and A. VENTURATO. 2003. *TIME Seattle Tsunami Mapping Project: Procedures, Data Sources and Products*. Seattle.

TSUTSUMI, A., T. SHIMAMOTO, E. KAWAMOTO, and J. LOGAN. 2000. Nearshore Flow Velocity of Southwest Hokkaido Earthquake Tsunami. *Journal of Waterway, Port, Coastal, and Ocean Engineering*. **126**(3): p.136–143, doi10.1061/(ASCE)0733-950X(2000)126:3(136).

UHSLC. 2005. *Records of the 2004 Indian Ocean Tsunami*. [online]. [Accessed 2005]. <http://ilikai.soest.hawaii.edu/uhslc/iotd/>

UHSLC. 2013. *University of Hawaii Sea Level Center*. [online]. [Accessed 2005]. <http://ilikai.soest.hawaii.edu/uhslc/>

UKHO. 2011. *United Kingdom Hydrographic Office*. [online]. <http://www.ukho.gov.uk/Pages/Home.aspx>

UNESCO/IOC. 2014a. *ICG/CARIBE EWS*. [online]. [Accessed 29 Oct 2014]. <http://iocaribe.ioc-unesco.org/icgcaribeews>

UNESCO/IOC. 2014b. *NEAMTWS*. [online]. [Accessed 29 Oct 2014]. <http://neamtic.ioc-unesco.org/neamtws>

USC. 2015. *Mapping and Modeling Benchmarking Workshop*. [online]. [Accessed 2015]. <http://coastal.usc.edu/currents_workshop/index.html>

USGS. 2012. *Magnitude 9.1 - OFF THE WEST COAST OF NORTHERN SUMATRA*. [online]. [Accessed 28 February 2012]. <http://earthquake.usgs.gov/earthquakes/eqinthenews/2004/us2004slav/#summary>

VAN RIJN, L.C. 1984a. Sediment transport, part I: Bed load transport. *Journal of Hydraulic Engineering ASCE*. **110**: 1431-1456.

VAN RIJN, L.C. 1984b. Sediment transport, part II: Suspended load transport. *Journal of Hydraulic Engineering ASCE*. **110**: 1613-1641.

VAN RIJN, Leo C. 1993. Principles of sediment transport in rivers, estuaries and coastal seas. *Aqua Publications I11*, p.690.

VAN RIJN, L. 1993. *Principles of Sediment Transport in Rivers, Estuaries and Coastal Seas*.; Delft (Aqua Publications).

VAN RIJN, L. C. 2007. Unified view of sediment transport by currents and waves. II: Suspended transport. *Journal of Hydraulic Engineering*. **133**(6): 668-689, doi10.1061/(ASCE)0733-9429(2007)133:6(668).

VAN RIJN, L. 2007. Unified view of sediment transport by currents and waves. II: Suspended transport. *Journal of Hydraulic Engineering*. **113**: 668-689, doi10.1061/(ASCE)0733-9429(2007)133:6(668).

VAN RIJN, L., D. J. R. WALSTRA, and M. VAN ORMONDT. 2004. *Description of TRANSPOR 2004 (TR2004) and implementation in DELFT3D-online*. Delft.

VASUDEVAN, S., M. ARUMUGAM, K. SRINIVASAMOORTHY, P. ANADHAN, and S. CHIDAMBARAM. 2007. Morphological changes in the beaches caused by tsunami in between Pondicherry and Portonova, East Coast of India. *Journal of Geosciences Osaka University*. **50**: 83-91.

VERBOOM, G., J. RONDE, and R. DIJK. 1992. A fine grid tidal flow and storm surge model of the North Sea. *Continental Shelf Research*. **12**(2): 213-233.

VERBOOM, G. K. and A. SLOB. 1984. Weakly-reactive boundary conditions for two-dimensional water flow problems. *Advances in water resources*. **7**(4): 192-197.

WHO. 2012. *Health action in crises. South Asia earthquake and tsunamis*. [online]. [Accessed 31 January 2012]. <http://www.who.int/hac/crises/international/asia_tsunami/en/>

YAMAZAKI, Y., Z. KOWALIK, and K. F. CHEUNG. 2009. Depth-integrated, non-hydrostatic model for wave breaking and runup. *International Journal for Numerical Methods in Fluids*. **61**(5): 473-497.

ZITELLINI, N., F. CHIERICI, R. SARTORI, and L. TORELLI. 1999. The tectonic source of the 1755 earthquake and tsunami. *Ann. Geofis.* **42**: 49-55.

Declaration

Herewith I declare that the work is my genuine work and nothing but the references and tools mentioned in my thesis and the advice of my supervisor were used to prepare the thesis.

Besides this I declare that the thesis had not been submitted elsewhere in an examination procedure, and that only the experiment of the North Sea was published as a scientific paper, as mentioned in Chapter 4.

I declare that this thesis has been prepared subject to the Rules of Good Scientific Practice of the German Research Foundation

Place/date: San José, Costa Rica, 10.03.2015

Signature

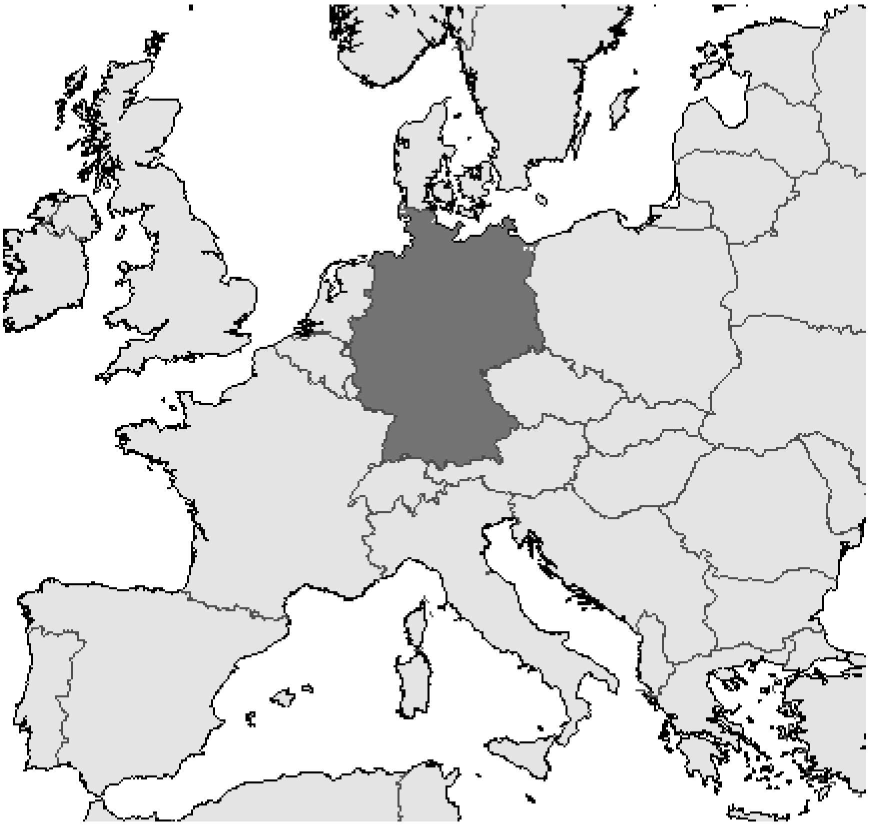

COASTAL RESEARCH LABORATORY
RESEARCH AND TECHNOLOGY CENTRE
CHRISTIAN-ALBRECHTS-UNIVERSITY
Hafentörn 1
D-25761 BÜSUM – GERMANY

telephone	**+49 (0) 4834 604200**
telefax	**+49 (0) 4834 604299**
e-mail	**info@corelab.uni-kiel.de**
internet	**www.ftz.uni-kiel.de**